National Library of Canada
Bibliothèque nationale du Canada

Canadian Theses Service
Service des thèses canadiennes

Ottawa, Canada
K1A 0N4

NOTICE

The quality of this microform is heavily dependent upon the quality of the original thesis submitted for microfilming. Every effort has been made to ensure the highest quality of reproduction possible.

If pages are missing, contact the university which granted the degree.

Some pages may have indistinct print especially if the original pages were typed with a poor typewriter ribbon or if the university sent us an inferior photocopy.

Previously copyrighted materials (journal articles, published tests, etc.) are not filmed.

Reproduction in full or in part of this microform is governed by the Canadian Copyright Act, R.S.C. 1970, c. C-30.

AVIS

La qualité de cette microforme dépend grandement de la qualité de la thèse soumise au microfilmage. Nous avons tout fait pour assurer une qualité supérieure de reproduction.

S'il manque des pages, veuillez communiquer avec l'université qui a conféré le grade.

La qualité d'impression de certaines pages peut laisser à désirer, surtout si les pages originales ont été dactylographiées à l'aide d'un ruban usé ou si l'université nous a fait parvenir une photocopie de qualité inférieure.

Les documents qui font déjà l'objet d'un droit d'auteur (articles de revue, tests publiés, etc.) ne sont pas microfilmés.

La reproduction, même partielle, de cette microforme est soumise à la Loi canadienne sur le droit d'auteur, SRC 1970, c. C-30.

NL-339 (r. 88/04)

Canada

THE UNIVERSITY OF ALBERTA

THE QUANTIFICATION AND DESCRIPTION OF PULMONARY EDEMA WITH NMR IMAGING

BY

© DAVID M. PHILLIPS

A THESIS

SUBMITTED TO THE FACULTY OF GRADUATE STUDIES AND RESEARCH

IN PARTIAL FULFILMENT OF THE REQUIREMENTS FOR THE DEGREE

OF MASTER OF SCIENCE

IN

EXPERIMENTAL MEDICINE

DEPARTMENT OF MEDICINE

EDMONTON, ALBERTA

FALL 1987

Permission has been granted to the National Library of Canada to microfilm this thesis and to lend or sell copies of the film.

The author (copyright owner) has reserved other publication rights, and neither the thesis nor extensive extracts from it may be printed or otherwise reproduced without his/her written permission.

L'autorisation a été accordée à la Bibliothèque nationale du Canada de microfilmer cette thèse et de prêter ou de vendre des exemplaires du film.

L'auteur (titulaire du droit d'auteur) se réserve les autres droits de publication; ni la thèse ni de longs extraits de celle-ci ne doivent être imprimés ou autrement reproduits sans son autorisation écrite.

ISBN 0-315-41016-7

THE UNIVERSITY OF ALBERTA

RELEASE FORM

NAME OF AUTHOR: David M. Phillips

TITLE OF THESIS: The Quantification and Description of Pulmonary Edema with NMR Imaging

DEGREE: Master of Science

YEAR THIS DEGREE GRANTED: 1987

Permission is hereby granted to THE UNIVERSITY OF ALBERTA LIBRARY to reproduce single copies of this thesis and to lend or sell such copies for private, scholarly or scientific research purposes only.

The author reserves other publication rights, and neither the thesis nor extensive extracts from it may be printed or otherwise reproduced without the author's written permission.

David M. Phillips

David M. Phillips

9105 112th Street

Apartment 02B

Edmonton, Alberta

T6G 2C5

THE UNIVERSITY OF ALBERTA

FACULTY OF GRADUATE STUDIES AND RESEARCH

The undersigned certify that they have read, and recommend to the Faculty of Graduate Studies and Research for acceptance, a thesis entitled THE QUANTIFICATION AND DESCRIPTION OF PULMONARY EDEMA WITH NMR IMAGING, submitted by DAVID M. PHILLIPS, in partial fulfilment of the requirements for the degree of MASTER OF SCIENCE.

.....
Co-Supervisor

.....
Co-Supervisor

.....

.....

Date: June 10, 1987

To Annabelle,

who was there from the beginning

ABSTRACT

The development of NMR imaging created great excitement within the medical community, for it offered a non-invasive imaging modality possessing a marked sensitivity to alterations of the mobile proton environment in tissues. The suggestion to employ NMR imaging both to visualize spatially and to quantify lung water came soon after its initial clinical trials. Such a technique would indeed prove advantageous: the measurements are non-invasive and non-destructive, do not require indicator tracers, are independent of ventilation-perfusion distributions, and may be performed repeatively.

The encouraging results from several preliminary in-vitro studies warranted an attempt to seriously evaluate the potential of NMR imaging to pulmonary medicine, and in particular to the investigation of lung water.

The initial stage of this evaluation comprised the development of optimal RF pulse sequences and respiratory-gated data acquisition procedures for obtaining quality in-vivo images of both the normal and the edematous lung. Moreover, it was desired that these images would be of sufficient quality to enable the measurement of in-vivo tissue magnetization relaxation times T_1 and T_2, both of which provide an index of tissue proton mobility.

The second stage of this project concerned the development of a quantitative technique that would permit the assessment of temporal alterations in the volume, nature, and distribution of oleic acid-induced pulmonary edema in experimental animals. This technique was established in an elaborate series of tissue-phantom experiments and then applied to two series of in-vivo pulmonary edema investigations. One of these latter experimental series terminated with the initial observation of edema within the acquired images, while the other series followed the course of the induced edema over 4-5 hours. Quantitative imaging data were then correlated with post-mortem lung water analyses.

The investigative findings clearly demonstrated that NMR imaging represents a worthy addition to both clinical and investigative pulmonary medicine. This imaging modality consistently exhibited an acute sensitivity to alterations in lung water volume, nature, and distribution. Indeed, its attributes were such that, for the study and diagnosis of pulmonary edema, NMR imaging may represent a more sensitive and reliable analytical tool than is currently available.

ACKNOWLEDGEMENTS

I wish to express my sincere thanks and graditude to my co-supervisors, Drs. S.F.P. Man and P.S. Allen, for granting me the opportunity to participate within the field of biomedical NMR imaging. Their continual support and enthusiasm, in all aspects of the research which constituted my MSc. project, are greatly appreciated.

I also wish to thank Dr. R.L. Jones for his lucid disclosures of the complexities and intricacies of cardio-pulmonary physiology. Moreover, I am very grateful that Dr. Jones was always most willing to discuss any physiological concern pertaining to my investigations.

I am indeed grateful for the generous financial assistance offered by both the Alberta Heart Foundation and the Alberta Heritage Research Foundation for Medical Research to the project described in this thesis.

Finally, I wish to express my sincerest thanks and appreciation to my contemporary members of the in-vivo NMR facility at the University of Alberta: Andrew Lunt, Erich Treiber, Chris Hanstock, Steve Knudsen, Cindy Stewart, Manuel Castro, Dan Doran, and Laird Trimble. These individuals helped to create one of the most unique and rewarding working environments it has been my pleasure to know. I am fortunate to be considered among their friends.

TABLE OF CONTENTS:

	Page
ABSTRACT	v
1. INTRODUCTION	1
2.1 THE LUNGS AND PULMONARY VASCULAR SYSTEM	
2.1.1 Overview	5
2.1.2 The Alveolar Epithelium	8
2.1.3 The Alveolar-Capillary Memebrane	10
2.1.4 The Pulmonary Circulation and its Associated Hemodynamics	14
2.1.5 Normal Pulmonary Blood Flow Distribution	18
2.1.6 Blood Flow Distribution in Pulmonary Edema	22
2.1.7 Increased Permeability Pulmonary Edema	24

2.1.8 The Adult Respiratory Distress Syndrome(ARDS) 25

2.1.9 The Bilateral Lung Lavage Model of ARDS 27

2.1.10 The Fat Embolism Syndrome 29

2.1.11 Oleic Acid-Induced Pulmonary Edema 31

2.1.12 Measurement of EVLW Content 35

2.2 THE THEORY OF NUCLEAR MAGNETIC RESONANCE (NMR) IMAGING

2.2.1 Basic NMR Theory 40

2.2.2 The Rotating Frame of Reference 46

2.2.3 The Effect of Rotating Magnetic Fields 49

2.2.4 Detection of the NMR Signal 53

2.2.5 The Bloch Equations 57

2.2.6 Magnetization Relaxation Processes 60

2.2.7 The Two-Site Rapid Exchange Model of Relaxation 70

2.2.8 Spin Echoes 77

2.2.9 2DFT Image Reconstruction 83

2.2.10 Slice Definition and Selective RF Excitation 91

2.3 THE APPLICATION OF NMR IMAGING TO CLINICAL MEDICINE

2.3.1 A Brief Historical Perspective 98

2.3 THE APPLICATION OF NMR IMAGING TO THE QUANTIFICATION AND DESCRIPTION OF LUNG WATER

2.3.2 A literature Review 102

BIBLIOGRAPHY FOR CHAPTER 2 115

3. PRELIMINARY IN-VIVO NMR IMAGING EXPERIMENTS

3.1 Introduction 122

3.2 Experimental

3.2.1 Imaging System and RF Sequences 124

3.2.2 Imaging of a Cat Model of Pulmonary Edema 127

3.2.3 Phantom Study 130

3.3 Results

3.3.1 Imaging of a Cat Model of Pulmonary Edema 132

3.3.2 Phantom Study 139

3.4 Discussion 144

References 154

4. PHANTOM EXPERIMENTS AND THE ESTABLISHMENT OF A QUANTITATIVE NMR TECHGNIQUE FOR THE MEASUREMENT OF LUNG WATER

4.1 Introduction 156

4.2 Experimental

4.2.1 General Outline 157

4.2.2 Spin Conditioning and the Verification of NMRI Parameters 160

4.2.3 Correction for Selective RF Excitation 165

4.2.4 The H_2O Quantity-Modified Proton Density Relationship 166

4.3. Results 169

4.4 Discussion 179

References 183

5. THE IN-VIVO QUANTIFICATION AND DESCRIPTION OF OLEIC ACID-INDUCED PULMONARY EDEMA WITH NMR IMAGING

5.1 Introduction 184

5.2 Experimental

5.2.1 Imaging System and RF Pulse Sequences 185

5.2.2 In-Vivo Experiments 189

5.2.3 Post-Mortem Analysis of EVLW 193

5.3 Results

5.3.1 In-vivo Experiments 196

5.3.2 Post-Mortem Measurements of EVLW 207

5.4 Discussion 212

References 225

6. CONCLUSIONS 228

APPENDIX 233

LIST OF TABLES

Table		Page
3.3.1	T_2 derived from the preliminary NMR imaging experiments	142
3.3.2	A comparison of phantom T_2 determinations from NMR images and from in-vitro spectrometric analysis	143
4.3.1	Transverse relaxation measurements for all phantom gel solutions	171
4.3.2	Longitudinal relaxation measurements for phantom gel solutions	173
4.3.3	The estimate of the signal intensity asymptote for all phantom gel solutions	175
4.3.4	The relationship between phantom gel water density and region of interest(ROI) volume-integrated signal intensity	177
5.3.1	Changes in arterial blood gas tensions with oleic acid treatment	203
5.3.2	ROI volumes of imaged edematous lung regions for series A experiments	204
5.3.3	Longitudinal magnetization relaxation indices for series A experimental animals	205
5.3.4	Transverse magnetization relaxation indices for series A experimental animals	206
5.3.5	Wet-to-Dry ratio and EVLW measurements, of all edematous lung tissue samples, for both series A and B experimental animals	209

5.3.6 Actual EVLW measurements, in relation to those predicted by NMR imaging, for all edematous lung regions of series A experimental animals 210

LIST OF FIGURES

Figure		Page
2.1.1	The rapid increase in total cross-sectional area of the airways within the respiratory zone	6
2.1.2	The alveolar and extra-alveolar pulmonary blood vessels	16
2.1.3	The distribution of pulmonary blood flow under normal conditions	19
2.2.1	The orientations that may be taken in an applied field B_0 by the magnetic moment of a nucleus with I = 1/2	41
2.2.2	The distribution of parallel and anti-parallel nuclear magnetic moments for a collection of nuclear spins, I=1/2, in a magnetic field B_0	43
2.2.3	The energies of the two orientations of a nucleus with I = 1/2 expressed as a function of the applied field B_0	44
2.2.4	The macroscopic magnetization vector, $\underline{M}$, and the effect of RF pulse excitation upon this vector	45
2.2.5	The effective magnetic field and the precession of the magnetization about it within the rotating frame of reference	51
2.2.6	The application of a $\underline{B_1}$ field of duration t_ω and its effect on the magnetization	52
2.2.7a	The effect of the applied $\underline{B_1}$ field in tilting the net nuclear magnetization from the Z′ -axis	53

2.2.7b	The X′Y′ components of magnetization, produced by the applied $\underline{B_1}$ field, rotating about the Z′ -axis with angular frequency ω_0	53
2.2.8a	An FID waveform	56
2.2.8b	The frequency spectrum, following Fourier transformation, derived from an FID waveform	56
2.2.9	The spectral density function, $J(\omega)$, as a function of angular frequency, for T_1 relaxation processes	63
2.2.10	The relationship between the proton longitudinal relaxation time and correlation time τ_c	65
2.2.11	The dephasing of the individual nuclear magnetic moments, together with the resultant decay of M_{x-y}, immediately following a 90° RF pulse	67
2.2.12	The relationship between T_2^* and the linewidth of the associated proton resonance peak	69
2.2.13	The relationship between the spectral density function, $J(\omega)$, and angular frequency for T_2 relaxation processes	70
2.2.14	A diagrammatic representation of water protons existing in the "bound" and "free" phases	72
2.2.15	A diagrammatic representation of the arrangement of water protons close to the surface of a protein molecule	76
2.2.16	The Hahn spin-echo pulse sequence	79
2.2.17	The Carr-Purcell spin-echo pulse sequence	81

2.2.18	The Carr-Purcell spin-echo pulse sequence with phase alternation of the individual 180° RF pulses	81
2.2.19	The Carr-Purcell-Meiboom-Gill spin-echo pulse sequence	83
2.2.20	The measurement of nuclear density along the direction of a linear magnetic-field gradient	85
2.2.21	A possible sequence of gradient pulses used in 2DFT imaging	86
2.2.22	A presentation of two elemental magnetizations	88
2.2.23	The frequency-domain components, at both f_i and f_{ii}, after a complex Fourier transformation of two different FID waveforms, with respect to t-t_y	90
2.2.24	A two-dimensional data array following a second Fourier transformation, with respect to t_y	91
2.2.25	The elemental magnetization components following the application of a wide bandwidth-rectangular 90° RF pulse	94
2.2.26	The tailored excitation function of a sinc RF pulse, together with its associated frequency-domain envelope	96
2.2.27	An NMR slice-defining pulsed gradient sequence	96
3.2.1	Three different respiratory-gated pulse excitation sequences developed for the preliminary in-vivo NMR imaging experiments	126

3.3.1	Four MSE images of the upper thorax of a cat, without pulmonary edema, acquired with the SCSS pulse excitation sequence	134
3.3.2	Two spin-echo images from a sequence of four MSE images of the upper thorax of a cat, without pulmonary edema, acquired with the SCSN pulse excitation sequence	136
3.3.3	Two spin-echo images from a sequence of four MSE images of the upper thorax of a cat, without pulmonary edema, acquired with the NSN pulse excitation sequence	137
3.3.4	One spin-echo image from a sequence of four MSE images of the thorax of a cat, with pulmonary edema, acquired with the SCSS pulse excitation sequence	138
3.3.5	Later spin-echo image of a stationary phantom from sequences of four MSE images produced by the three pulse excitation sequences	140
3.4.1	Later spin-echo images from sequences of four MSE images, produced by the SCSN pulse excitation sequence, depicting a flow phantom	149
4.2.1	The two imaging pulse excitation sequences employed for the phantom experiments	162
4.3.1	Comparison of proton R_2 values, as determined with both spectrometric and imaging techniques, for the phantom gel solutions	172
4.3.2	Comparison of proton R_1 values, as determined with both spectrometric and imaging techniques, for the phantom gel solutions	174
4.3.3	The relationship between normalized proton density, as calculated from images acquired with the SR pulse excitation sequence, and phantom gel concentration	176

4.3.4	The relationship between percentage increase in phantom water content and the associated percentage decrease in ROI volume-integrated signal intensity	178
5.2.1	The RF pulse excitation sequences employed for the later in-vivo NMR imaging experiments	187
5.3.1	The first spin-echo image from a sequence of four MSE images depicting the upper lung lobes of a cat, without pulmonary edema	199
5.3.2	The first spin-echo image from a sequence of four MSE images, depicting the initial edematous condition in the upper lung lobes of a cat	200
5.3.3	The first image of a 5-image SR sequence depicting the later edematous condition in the upper lung lobes of a cat	201
5.3.4	The relationship between actual EVLW content and that predicted by NMR imaging, for all edematous lung tissue samples of the later in-vivo NMR imnaging experiments	211
Appendix	A schematic diagram depicting the electronic respiratory-gating circuit employed for all in-vivo NMR imaging experiments described	234

SYMBOLS AND ABBREVIATIONS

ARDS	The Adult Respiratory Distress Syndrome
b_{local}	The time-varying local magnetic field at a particular nuclear site
$\underline{B}(t)$	a time-varying magnetic field
B_0	the externally-applied static magnetic field
ΔB_0	the magnitude of the static magnetic field inhomogeneity
$\underline{B}_1$	the oscillating, or rotating, magnetic field associated with the applied radiofrequency pulse excitation
$\underline{B}_{eff}$	the effective magnetic field
B_g	the magnetic field associated with the application of a linear magnetic-field gradient
CPMG	the Carr-Purcell-Meiboom-Gill pulse excitation sequence
D	the gas diffusion constant, measured in ml $minute^{-1}$ $mmHg.^{-1}$
E	energy
ΔE	the change in energy
E_I	the energy of interaction
emf	an electromotive force
EVLW	the extra-vascular lung water
F_I	the imaginary portion of the NMR signal, created during the process of complex Fourier transformation
F_R	the real portion of the NMR signal, created during the process of complex Fourier transformation
FID	a free-induction decay
F_IO_2	the inspiratory fraction of oxygen

G_r	a linear magnetic-field gradient positioned along the direction r
h	the Planck constant, 6.63×10^{-34} joule-second
Hb	hemoglobin
$\underline{i}$	a unit vector
I	the nuclear-spin quantum number
IR	the inversion-recovery pulse excitation sequence
$\underline{j}$	a unit vector
$J(\omega)$	the spectral density function of the angular frequency ω
$\underline{k}$	a unit vector
K	the Boltzmann constant, 1.38×10^{-27} joule molecule^{-1} °K
K_f	the filtration coefficient of a solute, measured in ml minute^{-1} mmHg.$^{-1}$
m(r)	an elemental magnetization component along the direction r
$\underline{M}$	the macroscopic magnetization vector
MHz	megahertz
MSE	the multiple spin-echo pulse excitation sequence
n_α	the nuclear population in the lower energy state
n_β	the nuclear population in the higher energy state
P_1, P_2	the partial pressures of a gas
P_a	the pulmonary arterial hydrostatic pressure
P_{alv}	the alveolar fluid hydrostatic pressure
P_{AW}	the airway pressure
P_b	the blood protein content within a lung tissue sample
P_c	the pulmonary capillary hydrostatic pressure

PHct	the pulmonary hematocrit correction factor, required when using using systemic blood samples as a reference for pulmonary blood hemoglobin measurements
P_{if}	the interstitial fluid hydrostatic pressure
P_{O_2}	the partial pressure of oxygen gas
P_{tm}	the pulmonary capillary transmural pressure
Q_b	the total blood mass within a lung tissue sample
Q_{dl}	the dry lung tissue mass
$\dot{Q}_f$	the net fluid filtration across the alveolar epithelium, measured in ml $hour^{-1}$
Q_{Hb}	the hemoglobin mass within a lung tissue sample
Q_{td}	the total dry lung tissue mass
Q_{wl}	the total wet lung tissue mass
QPSD	quadrature phase-sensitive detection
R_1	the rate of longitudinal magnetization relaxation
R_2	the rate of transverse magnetization relaxation
RF	radiofrequency
ROI	a region of interest
SG	the specific gravity
SR	the saturation-recovery pulse excitation sequence
S/N	the signal-to-noise ratio
t_ω	the time duration of the applied RF magnetic field
T	i)the surface tension of a fluid ii)Tesla
T_1	the longitudinal, or spin-lattice, magnetization relaxation time constant
T_2	the transverse, or spin-spin, magnetization relaxation time constant

T_2^*	the time constant for total dephasing of the transverse magnetization components
T_R	the pulse excitation sequence repetition time
2DFT	two-dimensional Fourier transformation image reconstruction
$\dot{V}_{gas}$	gas flow, measured in units of volume time^{-1}
W_b	the blood water volume within a lung tissue sample
W/D	the wet-to-dry ratio for a lung tissue sample
γ	the gyro-magnetic ratio for a nuclear species, measured in radians seconds^{-1} Tesla^{-1}
δ	a delta function
θ	the magnitude of an angle, measured in degrees
$\underline{\mu}$	the nuclear magnetic moment
$\Delta\nu_{1/2}$	the linewidth at 50% maximum amplitude of a proton resonance peak
π_{alv}	the alveolar fluid osmotic pressure, measured in mmHg.
π_c	the pulmonary capillary osmotic pressure
π_{if}	the interstitial tissue osmotic pressure
ρ	the proton density
σ_s	the reflective coefficent for a solute s, measured in ml mmHg.$^{-1}$ hour^{-1}
τ_c	the correlation time characterizing both rotational and translational molecular motion
ϕ	the phase angle, measured in radians
$\underline{\omega}$	the angular velocity
ω_0	the precessional frequency

1. INTRODUCTION:

The major impetus for investigating fluid exchange in the lung is predominently the clinical importance of pulmonary edema. Not only does the severe form of intra-alveolar pulmonary edema interfere with alveolar gas exchange, but its constituent fluid content, when combined with air, forms a durable foam that pronouncely affects both overall ventilation and its distribution throughout the various lung regions.

It is now recognized that clinical pulmonary edema is a late manifestation in a large number of different disease processes. This finding established the need to focus special attention on the early stages of pulmonary edema, when excess lung fluid is essentially restricted to the interstitial tissues and consequently the process is most often clinically silent.

Today, techniques commonly employed to diagnose pulmonary edema all exhibit limitations in either the degree of sensitivity to increases in lung water content, or in the ability to distinquish the early stages of pulmonary edema from other respiratory disease processes. These include roentgenography, x-ray computer tomography, measurements of both pulmonary function and gas exchange, and indicator-dilution techniques. Thus, it must be concluded that the clinical detection of early lung edema is not possible.

In 1973, the development of Nuclear Magnetic Resonance(NMR) imaging generated considerable excitement, since it represented a reliable and sensitive tool for the diagnosis of subtle alterations in tissue water content. Moreover, pioneering investigators in the development of NMR imaging, such as Paul Lauterbur(42) and J.A. Frank(23), suggested the future application of this new imaging modality for both the investigation and diagnosis of pulmonary edema. Indeed, with its marked sensitivity to changes in the mobile proton environment, NMR imaging represents an excellent diagnostic tool for the non-invasive detection and description of the initial stages of this pathophysiological condition. Despite such early enthusiasm, and the appearance of several preliminary investigations (8,11,28,62-64,72) demonstrating the applicability of NMR techniques to the study of lung water, a truly in-vivo quantification and description of pulmonary edema with NMR has yet to be presented. This is principally due to the complexity of NMR imaging and to the technical difficulties associated with the obtainment of reliable quantitative information from the in-vivo lung.

This thesis describes the application of NMR techniques to the in-vivo investigation of lung fluid exchange in experimental animals. The project itself is divided into two main sections:

1) The development of optimal radio-frequency(RF) pulse excitation sequences and respiratory-gated data acquisition procedures for generating quality in-vivo images of both the normal and the edematous lung

2) The establishment of a quantitative technique (for determining both the longitudinal and transverse magnetization relaxation indices, and proton density of the in-vivo lung) that would permit the assessment of temporal alterations in the volume, nature, and distribution of oleic acid-induced pulmonary edema

The above sections are described in chapters 3-5. Chapter 2.1 provides a review to the anatomy and physiology of the respiratory system, the histology of the alveolar-capillary membrane, the influential factors of lung fluid exchange, current methods for clinically measuring lung water content, and the pathological changes established by certain disease processes which eventually lead to pulmonary edema. Also described are the experimental animal models that have been devised to produce pulmonary edema, and which have been employed in the studies outlined in this thesis. Chapter 2.2 presents the principals of NMR imaging that are germane to this discussion, while chapter 2.3 briefly

reviews the application of NMR techniques both to medicine and, in particular, to the study of pulmonary edema. Chapter 6 summarizes the experimental findings of this thesis, discusses the possible goals or objectives for future endeavours within this area, and relates the applicability of the developed quantitative NMR technique to the clinical setting.

THE LUNGS AND PULMONARY VASCULAR SYSTEM

2.1.1 AN OVERVIEW:

The cardinal function of the human lungs is to exchange gases. In so doing, oxygen is allowed to diffuse from the atmosphere into the blood and carbon dioxide is allowed to diffuse from the blood. In terms of its principal functional anatomy, the lung may be thought of as comprising four components: the conducting airways, the alveolar ducts, the alveolar-capillary membrane, and the blood vessels.

The conducting airways consist of a series of branching tubes, or conduits, which become increasingly narrower, shorter, and more numerous as they penetrate deeper into the lung. These comprise the trachea, the right and left main bronchi, the lobar bronchi, the segmental bronchi, and finally the terminal bronchioles. The conducting airways, including the portion between the nares and trachea, take no part in gas exchange and as such constitute the anatomical dead space, whose volume under normal conditions is approximately 150 milliliters(ml) in humans.

The terminal bronchioles divide into the respiratory bronchioles which may possess occassional alveoli, small polygonal-shaped air sacs averaging 75-300 micrometers(μm) in diameter, which represent the site for gas exchange. However, it is only in the following segment, the alveolar

ducts, that one encounters the anatomical region of the lung where gas exchange occurs per se. This region, also described as the respiratory zone, is completely lined with alveoli, which may number as many as 300 million. The alveoli's polygonal shape, together with their large number, greatly increases the cross-sectional area of the respiratory zone(see Fig. 2.1.1). Thus although the distance from the terminal bronchioles to the most distal alveolus is approximately only 5.0 mm, the volume of this respiratory zone may exceed 2500 ml at functional residual capacity (FRC), and thus constitutes the majority of the lung's gas volume.

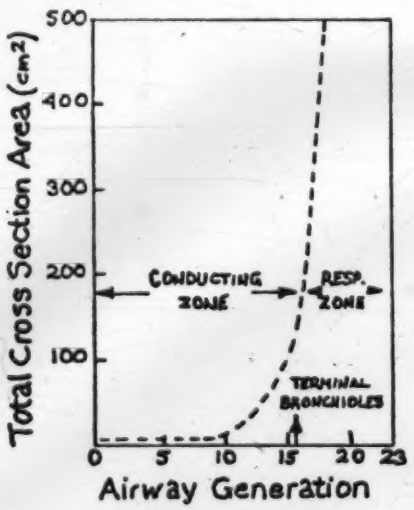

FIGURE 2.1.1: A graphical representation of the rapid increase in total cross-sectional area of the airways within the respiratory zone of the human lungs.

Air travels through the conducting airways, until the level of the terminal bronchioles, essentially through bulk flow. Beyond this point, the forward velocity of the air becomes quite small, as a result of the enormous increase in cross-sectional area occurring at the level of the alveolar ducts. Diffusion rapidly becomes the predominant mode of flow within the respiratory zone. Fick's law of diffusion states that movement of a gas across a membrane is proportional to the cross-sectional area of the membrane and inversely proportional to its thickness:

$$\dot{V}_{gas} \propto (A/T)(D)(P_1-P_2) \qquad (2.1.1)$$

where V_{gas} is gas flow, measured in volume per unit time, A is the cross-sectional area of the membrane, and T is the membrane thickness. D is the diffusion constant of the gas in question, measured in ml x minute^{-1} x mmHg^{-1}, and (P_1-P_2) is the difference in partial pressure of the gas across the membrane, measured in mmHg. The membrane across which oxygen must diffuse to reach the blood is exceedingly thin, less than 0.5 micrometer(μm), and has a total cross-sectional area of between 50 and 100 square meters. Consequently, the rate of diffusion for gases such as oxygen within the respiratory zone is so rapid that differences in gas concentrations are virtually abolished within one second (71).

The pulmonary blood vessels also form a series of branching tubes: beginning with the pulmonary arteries, continuing through the extensive capillary network, and then terminating with the pulmonary veins. The capillaries form a dense network within the walls of the alveoli, completely enveloping the latter structure. With their small diameter(10 μm, or just large enough for an erythrocyte to pass through) and extremely short length, this capillary network is a virtual sheet of blood contained within the alveolar wall, an extremely efficient arrangement for gas exchange. Indeed, although each erythrocyte spends about 1.0 second in the capillary network, it will traverse perhaps two or three alveoli, such that virtually complete equilibration of oxygen and carbon dioxide is obtained between alveolar gas and the capillary blood(71).

2.1.2 THE ALVEOLAR EPITHELIUM:

The alveoli are polygonal-shaped air sacs, averaging 75-300 μm in diameter, which consist of an epithelium lined by a dual layer of lipoproteins.

The epithelium is composed of two varieties of cells: Type I and Type II(granular epithelial). Type I cells do not divide but, owing to their large size, constitute 95% of the alveolar surface. Type II cells, which make up the remaining portion of the alveolar surface, do divide and in fact are

believed to give rise to both Type I and Type II cells(20). Type II cells are metabolically active and synthesize surfactant, of which a major component is the phospholipid dipalmitoyl lecithin(71). Surfactant is a remarkable compound, vitally important to the normal operational mechanics of the lung, and is present in the outermost lipoprotein layer covering the alveolar epithelium.

The underlying lipoprotein layer is a high-molecular weight, saline-dispersable complex, rich in phospholipids (56). From this, through some form of surface action, the outermost lipoprotein layer is fashioned. This latter insoluble layer, while being only some 50 angstroms(A) thick, possesses the vital compound surfactant. Surfactant greatly reduces the surface tension of the fluid lining the alveoli, making inflation of the alveoli remarkably easy. For example, in a normal healthy lung, a breath of approximately 500 ml requires a distending pressure of less than 3.0 cm H_2O(71). In certain pathological conditions, for example the Adult Respiratory Distress Syndrome(ARDS) and the later stages of the fat embolism syndrome, this outer alveolar lipoprotein lining is either defective or damaged, resulting in collapse of the alveoli. The ensuing reduction in the respiratory zone's cross-sectional area consequently presents severe deleterious consequences for subsequent gas exchange. Thus, the ramifications of comprehending the underlying mechanisms for these two disease states are obvious.

2.1.3 THE ALVEOLAR-CAPILLARY MEMBRANE:

The alveolar-capillary membrane consists of two lipoprotein layers(the outer of which contains surfactant), the alveolar epithelium and the capillary endothelium together with their basement membranes, and the interstitial space. Early pulmonary investigators(19) believed that liquid from the capillaries readily entered the alveoli, to be later reabsorbed into the interstitium and lymphatics at the broncho-alveolar junction. Today, there exists anatomical and physiological evidence that such is not the case. Moreover, the permeability of the capillary endothelium has been demonstrated to exceed that of the alveolar epithelium. In fact, it appears that not only is the normal alveolar epithelium effectively impermeable to macromolecules, but that it also possesses a very low permeability to small solutes such as electrolytes (67).

Transport across the alveolar-capillary membrane may be described by the following equations derived from the Starling relationship:

Fluid transport across the capillary endothelium:

$$\dot{Q}_f = K_f[(P_c - P_{if}) - \sigma_s(\pi_c - \pi_{if})] \qquad (2.1.2a)$$

Fluid transport across the alveolar epithelium:

$$\dot{Q}_f = K_f[(P_{if}-P_{alv}) - \sigma_s(\pi_{if} - \pi_{alv})] \qquad (2.1.2b)$$

where Q_f is the net fluid filtration, measured in ml per hour, and K_f is the filtration coefficient of the solute in question, measured in ml x $mmHg^{-1}$ x $hour^{-1}$. P_c-P_{if} represents the hydrostatic pressure difference between the capillary and the interstitum, while $P_{if}-P_{alv}$ represents that between the interstitium and the alveolar fluid, and σ_s is the reflective coefficient for the solute s, measured in ml x $mmHg^{-1}$ x $hour^{-1}$. $\pi_c - \pi_{if}$ represents the oncotic pressure difference between the capillary and interstitium, while $\pi_{if} - \pi_{alv}$ represents that between the interstitium and the alveolar fluid. Under normal conditions, $\dot{Q}_f$ is essentially zero.

Solute diffusion is dependent on molecular weight, lipid solubility and the structural characteristics of the alveolar-capillary membrane. Thus the reflective coefficient may vary from 1(a perfect semi-permeable membrane) to 0(an extremely leaky membrane). Large osmotic pressure gradients across the alveolar epithelium for low molecular weight solutes such as Na^+ and Cl^- are indeed possible. An active transport mechanism would represent an ideal method to adjust the osmotic pressure gradient and has, in fact, been documented(31). Despite the remarkable qualities of the alveolar epithelium it is unfortunately extremely delicate.

For example, in pneumonia the epithelium is easily lifted from the underlying tissue, suggesting that it cannot withstand any significant pressure differential directed toward the alveolus(51).

The complex geometry and architecture of the alveoli give rise to a natural tendency for fluid to enter from the surrounding interstitium. The surface tension at the alveolar air-liquid interface exerts a force tending to draw fluid into the alveolar lumen. An alveolus' polygonal shape forms a series of planes with sharp corners at the adjacent edges where the fluid radius can be as small as 0.5 μm and the associated force drawing fluid into the alveoli as great as 300 mmHg(48). However, there exists a multitude of protective mechanisms to oppose excessive entry of fluid into the alveoli. The surface tension and consequently the fluid-drawing force can be effectively reduced by surfactant. Nevertheless, some fluid does in fact enter into the alveolar lumen, although the exact pathway and mechanism is unknown(67). Regardless of how it enters the alveoli, this fluid may combine with the surfactant to form an effective force opposing further entry of fluid. The minute amount of alveolar fluid which collects at the corners of the polygon may form a dome, convex to the airway lumen. From the Laplace relationship for two interacting surfaces:

$$P = (4 \times T)/R \qquad (2.1.3)$$

where P is the resultant pressure, T is the surface tension existent within the alveolar fluid, and R is the dome radius, this may result in the establishment of a considerable force which would tend to drive fluid out of the alveoli(29). In addition, the lymphatic vessels, present in the interstitium of the alveolar-capillary membrane network, can effectively increase their fluid conductance by 10-fold(68), thus establishing an extensive operational margin of safety. Consequently, drastic increases in the hydrostatic/oncotic pressure differential may be continually experienced before the lymphatics' drainage capabilities are exceeded.

However, in certain pathological conditions(most notably, increased permeability pulmonary edema) fluid filtration out of the capillaries may increase to such an extent that fluid accumulates too rapidly within the interstitium to be removed completely. The accumulating fluid will then expand the interstitium's loose connective tissue, which has been shown to be easily distended at low pressures(9,25), forming a peribroncho-vascular cuff. Eventually the increased hydrostatic pressure in the interstitium may equal or exceed the effective pressure in the alveoli. Consequently, the accumulated liquid will begin to overflow into the air spaces, extensively reducing the effective cross-sectional area available for gas exchange. This alveolar flooding has been shown to commence when the extravascular lung water(EVLW) content, at FRC, increases by

20-30%(67). Such values of EVLW would represent extensive pulmonary edema.

2.1.4. THE PULMONARY CIRCULATION AND ITS HEMODYNAMICS:

As discussed in section 2.1.1, the pulmonary vascular system begins at the main pulmonary artery, which receives mixed venous blood from the heart's right ventricle. This artery then branches successively in a fashion very similar to that of the airways, and follows the course of the bronchi down to the primary lobules of the lung until the terminal bronchioles. Beyond this point, these vessels divide extensively to establish the pulmonary capillary bed which lies predominantly within the walls of the alveoli. Indeed, so extensive is the capillary bed's mesh-like construction that many investigative physiologists consider it more correct to describe it as a virtual sheet of flowing blood. Following the capillary bed, the now-oxygenated blood passes into small pulmonary veins which run between individual lung lobules. Eventually these veins terminate in the large pulmonary veins, which then continue directly into the left atrium.

Hydrostatic pressures within the pulmonary circulation are remarkably low. The mean pressure in the main pulmonary artery is typically 15 mmHg. However, there is considerable fluctuation in this hemodynamic parameter throughout the

cardiac cycle. Systolic pressures commonly approach 25 mmHg whereas those associated with diastole are ~8 mmHg. Thus, blood flow is highly pulsatile through the pulmonary circulation, a characteristic which manifests important consequences when attempting to acquire multiple spin-echo images of the in-vivo lung without cardiac-cycle synchronized data acquisition(see chapter 3). The walls of the pulmonary artery are quite thin and contain little smooth muscle, in contrast to arterial walls of the systemic circulation. Thus, the pulmonary artery is exceedingly pliant and resistance is therefore relatively low. Pressure within the pulmonary capillaries is not known exactly, although it must lie somewhere between that of the main pulmonary artery and the left atrium. However there is evidence which suggests that a large proportion of the pressure change occurring in the pulmonary vasculature is associated with the capillary bed. Thus the distribution of pressures is considerably more symmetrical than is that of the systemic circulation.

The pulmonary capillaries receive little support from the thin layer of epithelial cells lining the alveoli. These vessels are hence liable to collapse, depending on the difference in pressure within and around them, commonly described as the transmural pressure(P_{tm}). Occasionally, the effective pressure around the capillaries is decreased by the surface tension created by the alveoli's fluid lining, producing an enlargement of their dimensions. More

commonly, however, the alveolar pressure(P_{alv}) is increased above the pressure within the capillaries, resulting in their collapse. The situation is somewhat different for the case of the pulmonary arteries and veins. As the lung expands during inflation these larger vessels are pulled open by the elastic tension created by the expanding lung parenchyma. Alternatively, when lung volumes are low, the relatively thin walls of these vessels are insufficient to maintain a patent lumen and consequently their internal diameter decreases. The difference in behaviour between these two classes of pulmonary vessels has led to describing them as either alveolar or extra-alveolar(see Fig. 2.1.2).

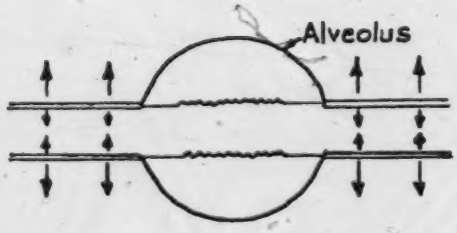

FIGURE 2.1.2: A diagrammatic representation of the structural relationship between an alveolus and both its alveolar and extra-alveolar pulmonary blood vessels.

The former category, consisting of the capillaries and both small arterioles and veins, is influenced primarily by P_{alv}. The latter category, which includes the pulmonary arteries and veins, is subject to the characteristics of the lung parenchyma and therefore possesses the more complex behaviour. The very large vessels of the pulmonary vasculature, situated near the hilum, are entirely outside the lung and its influences, and are therefore subject to the pressures within the thoracic cage.

Although the normal pulmonary vascular resistance is comparatively low, it can become even smaller in magnitude as hydrostatic pressures in the constituent vessels increase. There are two mechanisms responsible for this phenomenon: capillary recruitment and distension of the pulmonary capillaries. Under normal functional conditions, not all capillaries are open. However with increased hydrostatic pressures, the capillaries which were initially closed, now become patent and are "recruited" into the population actively transporting blood by the alveoli. Consequently the overall vascular resistance is greatly diminished. Although the exact mechanism of this behaviour is unknown, several hypotheses have been proposed. Some investigators believe that differences in vessel geometry, which produce preferential channels for blood flow, may be the causative agent. However, others maintain that a critical opening pressure must be exceeded before any of these "recruited" capillaries conduct blood. Pulmonary

capillary distension occurs predominantly at elevated vascular pressures, and thus is typically not the major component for lowering vascular resistance. Nevertheless, the endothelial wall of the pulmonary capillaries is thin and very pliable, two characteristics which undoubtably contribute to the observed distention.

In addition to the above, pulmonary circulation hemodynamics are similarily responsive to alterations in lung volume. Increased lung volumes distend and increase the calibre of extra-alveolar vessels, whereas decreased volumes constrict these vessels, thus contributing to an elevated vascular resistance. The response of alveolar vessels to changes in lung volume tends to contrast with that of the extra-alveolar vessels. With increased lung volume, P_{alv} increases, the alveolar walls are stretched and the associated alveolar vessels become stretched and narrowed. Such behaviour is far more influential in determining overall pulmonary vascular resistance, as this hemodynamic parameter tends to continually increase with enlargened lung volumes.

2.1.5. THE NORMAL PULMONARY BLOOD FLOW DISTRIBUTION:

There exists a considerable degree of inequality in the regional pulmonary blood flow. When in the upright position, blood flow continually decreases from the bottom lung

regions to those of the top, in an almost linear fashion(see Fig. 2.1.3).

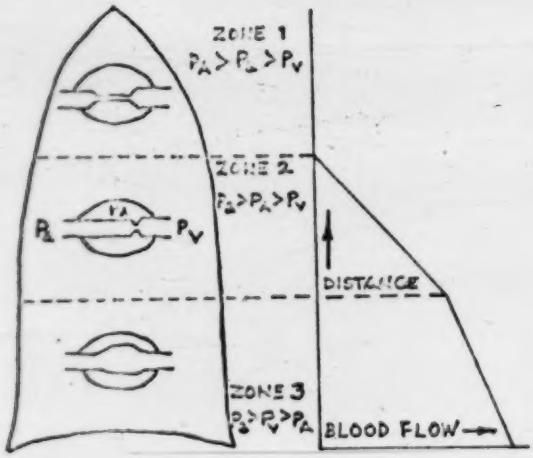

FIGURE 2.1.3: The distribution of pulmonary blood flow in the human lung under normal conditions. The relative magnitudes of the alveolar air pressures (P_A) and the pulmonary vascular pressures (P_a and P_v) for each of the various zones are also provided. The graph on the right depicts the increase in blood flow experienced as one progresses from Zone 1 to Zone 3 of the vertically-positioned human lung.

This phenomenon has been described in detail by West and his colleagues(70). Zone 1, which represnts the most apical lung regions, is an area where the pulmonary arterial pressure(P_a) is below that of P_{alv}. Therefore capillaries are collapsed and blood flow is zero. Such a zone does not readily present itself under normal conditions, as P_a is usually sufficient to raise blood to this region, especially during systole. However, clinical interventions such as

positive-pressure ventilation may well increase P_{alv} high enough to create the required circumstances. Since Zone 1, if it exists, represents an area that is unperfused, it constitutes the alveolar dead space. Farther down the lung, P_a begins to exceed P_{alv} due to the influence of gravity on the hydrostatic pressure within the involved vessels. However, as P_{alv} remains greater in magnitude relative to the pressure in the pulmonary veins(P_v), flow is determined by the relative difference between P_a and P_{alv}. This is the predominant characteristic of Zone 2. As one progresses down this zone, P_a continually increases, while P_{alv} remains essentially constant. Thus, the driving pressure for flow in this zone steadily increments and initiates both capillary recruitment and eventually capillary distention, both of which serve to increase blood flow. In the basal regions of the lung, increasing hydrostatic pressures elevate both P_a and P_v above P_{alv}, such that flow is determined by the relative difference between P_a and P_v. The driving pressure within the vessels is sufficiently large that capillary distention is the predominant mechanism for increasing flow. Indeed, intricate measurements have revealed that capillary dimensions are greater in Zone 3 than either of the above two zones(71). In addition, further recruitment of pulmonary capillaries may contribute to the further enhancement of flow distribution.

However, this pattern of blood flow distribution is greatly altered by position. When in the supine position, the blood flow to the anatomical lung apex dramatically increases while that of the anatomical base remains virtually unaltered. This produces a considerably more uniform distribution than that of the upright position. However, while in the supine position, blood flow along the posterior-anterior axis of the lung does exhibit a gravity-dependent distribution. The magnitude of this dependency is chiefly determined by the vertical height of the lung established along the posterior-anterior axis. Thus, blood flow would be considerably more influenced within the lung base, where this dimension is maximal.

Gravity is able to manifest the influences outlined above by either increasing or decreasing the hydrostatic pressures in the pulmonary vessels. If one considers the pulmonary vascular system, in the upright position, as a continuous column of blood, the alterations in hydrostatic pressure between apical and basal regions approaches 30 cm H_2O, or 23 mmHg. This represents a considerable pressure differential for such a low pressure/low resistance system as the pulmonary vasculature.

Although the resistance of the pulmonary vasculature is, under normal conditions, quite low, it is markedly responsive to changes of alveolar gas P_{O_2} and may readily alter the existent blood flow distribution pattern. The mechanism for this involves contraction of the smooth muscle

present within the walls of the small arterioles in the hypoxic region. This response persists in excised isolated lung tissue and thus does not require CNS involvement. Even excised pulmonary artery segments have been shown to actively constrict if the environment is made sufficiently hypoxic. Interestingly, if the lung tissue is perfused with blood of an elevated P_{O_2}, exposure to hypoxic environments continues to elicit this same response. Exposure to low alveolar P_{O_2} may cause cells in the perivascular tissue to release a vasoconstrictor molecule. Regardless of its exact mechanism, this vasoconstriction re-directs blood away from the hypoxic regions of the lung, thus minimizing the adverse effects on subsequent gas exchange.

2.1.6. BLOOD FLOW DISTRIBUTION IN PULMONARY EDEMA:

In the early stages of pulmonary edema, as fluid begins to accumulate in the interstitial space, P_{tm} decreases, thus producing restricted blood flow to the particular lung region involved. One may intuitively expect that such restriction would aid to re-direct blood flow away from edematous lung regions. However, Naimark et al.(55) have shown that gross edema is required before any significant shift in regional blood flow distribution actually occurs. This has been confirmed with both histological and physiological data by Muir et al.(53), who demonstrated that

blood flow is altered only when alveolar edema has formed. Thus, it would appear that accumulation of fluid in interstitial tissues presents little, if any, significant influence on pulmonary blood flow distribution.

The substitution of fluid pressure for gas pressure within alveoli could theoretically decrease P_{tm} of the alveolar vessels and therefore increase local vascular resistance. It is also possible to envision that the alveolar collapse, subsequent to their flooding, produces a local reduction in the lung volume, resulting in the constriction of the extra-alveolar vessels. However, it has been reported that such regionalized atelectasis does not produce significant alterations in pulmonary blood flow(54). Therefore, it appears reasonable to conclude that it is the alveolar fluid cuff component of airspace edema which is the predominant influence for increasing vascular resistance, and thereby limiting further local blood flow. Such a mechanism provides efficient control for re-directing blood perfusion away from lung regions that are no longer well ventilated. Adequate gas exchange is thus ensured until comparatively late in the evolution of pulmonary edema. Indeed, rapid deterioration of gas exchange may correctly be assumed to indicate fluid accumulation in both the alveoli and the immediately adjacent airways.

2.1.7 INCREASED PERMEABILITY PULMONARY EDEMA:

Increased permeability pulmonary edema is characterized clinically and experimentally by an increase in lung lymph and EVLW protein content, both of which contain plasma proteins at concentrations higher than expected for the known driving pressures. This form of pulmonary edema is the most commonly seen in the clinical setting(50), an observation most probably due to the wide variety of agents that may induce it: trauma, bacterial endotoxins, shock, microembolism, smoke and fume inhalation, radiation, and various drugs(heroin, salicylates, etc.). Many of these agents produce, either directly or indirectly, damage to the alveolar-capillary membrane manifested as gap formation, swelling, sloughing, and cell death(50).

In increased permeability pulmonary edema an elevated filtration rate($\dot{Q}_f$) occurs at any driving pressure. The associated protein concentrations(usually exceeding 70% of the plasma level) across the membrane are sufficiently altered to markedly reduce the effectiveness of the normal oncotic feedback control. Thus two prinicpal mechanisms protecting the alveoli from edema have failed, either partially or completely. Consequently, increased permeability pulmonary edema is characterized by sudden onset and rapid progression(67), resulting in a reduced vital capacity, deterioration of ventilation-perfusion ratios, and an increase in the alveolar-arterial oxygen

tension difference. Failure to recognize the early stages of this pathological condition may lead to a continuous downhill course(65). Moreover, measures taken later to ameliorate a patient's condition, such as mechanical ventilation with an elevated F_IO_2, may further damage the alveolar epithelium and thus inadvertently contribute to continued deterioration in pulmonary function(65).

2.1.8 THE ADULT RESPIRATORY DISTRESS SYNDROME(ARDS):

ARDS is one of many conditions that manifest severe injury to the alveolar-capillary membrane. It is characterized by marked pulmonary parenchymal inflammation and increased permeability of the alveolar-capillary membrane, both of which lead to severe hypoxemia and widespread infiltrates. Mortality from ARDS is high, ranging from 20 to 83%(20), and results from either progressive respiratory failure or associated multi-system disease.

This pathological condition may be described as progressing through several phases(20), each more serious than that which preceded:

1)profound dyspnea and tachypnea, normal roentgenogram

2)increased cyanosis, hypoxemia, minor roentgenogram changes

3)respiratory failure, profound hypoxemia, decreased compilation, diffuse bilateral infiltrates

4)severe hypoxemia unresponsive to O_2 therapy, metabolic and respiratory acidosis

Visualization of ARDS via conventional diagnostic imaging is only possible in the later stages of the disease, when the patient's condition is severely compromised. The development of an imaging modality that would permit visualization of the early stages is clearly warranted.

One of the purportive components in the etiology of ARDS is deficient or damaged surfactant, and its involvement is supported by several pieces of circumstantial evidence (20). Firstly, there exists a similarity between the half-life of surfactant and the latent period between lung injury and the clinical manifestations of ARDS. This would suggest that the Type II cells are damaged in some forms of ARDS relatively early in the course of the disease, after which their production of surfactant is markedly reduced. Secondly, the reduced lung compliance so prevalent in ARDS could certainly be associated with the loss of free or intracellular surfactant. Finally, surfactant that has been removed from ARDS patients by endobronchial lavage has been found to be abnormal, both structurally and functionally.

Given the above observations, it is not altogether surprising that an experimental model of ARDS was developed

in 1980(39) whose principal characteristics are surfactant deficiency with simultaneous damage to the alveolar epithelium and its associated structures. It was a variation of this technique, initially described as in-vivo bilateral lung lavage, that served as the model for pulmonary edema in the preliminary NMR imaging experiments described in this thesis(see section 3.2.2).

2.1.9 THE BILATERAL LUNG LAVAGE MODEL OF ARDS:

The experimental model described by Lachmann and co-workers(39) closely resembles ARDS in terms of arterial blood gas tensions, pulmonary mechanics, and morphological changes as observed with both light and electron-microsocpy. By varying the number of individual lavages performed on the experimental animal, it is possible to alter the severity of the pulmonary function disturbance. Moreover, strictly following the lavage protocol, as outlined below, has been reported to result in a reproducible status(40).

The bilateral lung lavage is performed with physiological saline(35 ml/kg body weight), heated to 37°C.. The dosage employed corresponds to 80-90% total lung capacity, or the lung volume at 35 cm H_2O transpulmonary pressure. The lavage, of 20 seconds duration, is repeated approximately 10 times, each separated by an interval of 5 minutes. The principal effects induced by the lavage are a

reduced inspiratory maximal volume, a reduced FRC, hypoxemia, and edema.

In order to evaluate the application of NMR imaging to the detection and quantification of pulmonary edema, a variant form of the in-vivo bilateral lung lavage model, described above, was employed. A lavage fluid of 0.1N HCl, approximately iso-osmotic with body fluids at 290 mOsm./kg H_2O(or 1.315 gm NaCl/500 ml of solution), replaced the physiological saline used by Lachmann et al. Thus, this modified lavage model more closely resembled inflammatory pneumonitis, especially as induced by the aspiration of gastric contents. This condition, frequently observed in the clinical setting, shares more characteristics with ARDS than would perhaps be intuitively expected(73). Isolated areas of atelectasis become present within minutes of the initial insult. Later examination reveals edema, hemorrhage, and areas of epithelial degeneration, all of whose severity is predominantly influenced by the volume and distribution of the "aspirate".

Despite approximating certain ARDS characteristics, the bilateral lung lavage model does possess some disdvantages. The continual mechanical ventilation with an elevated F_IO_2, essential for maintaining the survival of the experimental animal, may aggravate the initial epithelial lesions induced by the lavage(39). Therefore, it has been emphasized(40) that arterial blood gas tensions be continually monitored throughout the post-lavage period to provide an index of the

experimental animal's respiratory status. In addition, contrary to other reports, I have found that the lavage model is both highly dynamic and unstable. These latter characteristics prevent the acquisition of reliable in-vivo tissue magnetization relaxation times(T_1 and T_2), or an index of in-vivo tissue proton mobility, of any one stage in the patho-physiological process. Thus it was decided, that for the purposes of the experiments concerning lung water quantification and description, to employ the much more stable oleic acid model of increased permeability pulmonary edema. This model produces lesions and patho-physiological changes that are virtually identical with those of the fat embolism syndrome(18).

2.1.10 THE FAT EMBOLISM SYNDROME:

Fat embolism is a clinical entity frequently observed with the fracture of the long bones, orthopedic manipulation, hyperlipemia, and diabetes(27). This condition may prove to be a principal cause of increased patient morbidity and death in cases involving mechanical trauma and its ensuing shock. Although its pathogenesis is hedged in controversy, and an effective single treatment is unfortunately lacking, the diagnosis of fat embolism can be made with both confidence and assurance(58).

Patients exhibiting the classic form of fat embolism are commonly asymptomatic for the initial 24-48 hours. This time interval is frequently described as a "latent period". Although this term implies quiessence or inactivity, this is certainly not the case, for it is during this period that the early changes brought about by fat embolism occur(57).

Dyspnea, hemorrhagic petechiae, and a drastic fall in blood hemoglobin content are the initial, clearly discernable symptoms of this pathological condition. When fat emboli large enough to occlude arterioles and capillaries appear in the blood, they are rapidly and efficiently filtered by the lungs(16). Indeed, it has been observed that in 75% of all patients displaying classic symptoms of fat embolism, the lung is the only organ which possesses embolic fat(47). Unfortunately, this remarkable filtration process results in adverse effects to normal lung structure and function, evidenced by a progressive downhill course in the patient's condition. At autopsy, the lungs are engorged with whole blood, frequently weighing 2 to 3 times their normal weight. This finding suggests intra-alveolar hemorrhage and histological examinations of such tissue have revealed numerous areas of completely disintegrated alveolar structure(57). Consequently, it has been proposed that there are two phases to the pathogenesis of fat embolism: the mechanical obstruction of the smaller vessels in the pulmonary vasculature, and the hydrolysis of the emboli's neutral fats to free fatty acids which then chemically

interact with the pulmonary vessels' endothelium. It is this secondary, or chemical, phase that undermines alveolar structure and produces the life-threatening intra-alveolar hemorrhage. In addition to the above, pulmonary embolism, through its mechanical obstruction of the pulmonary vasculature, affects the blood flow occurring within the pulmonary vascular bed. Consequently, drastic alterations ensue in both the local hemodynamics and cardiac function.

Oleic acid represents over 60% of the free fatty acid pool found in mammals(22). Intravenous injection of small dosages results in both acute and chronic pulmonary lesions that are virtually identical to those of the fat embolism syndrome(18). Thus, the administration of oleic acid to experimental animals has become a popular model with which to study both the patho-anatomical lesions and patho-physiological changes consequent to this syndrome. A key constituent of the latter category is increased permeability pulmonary edema.

2.1.11 OLEIC ACID-INDUCED PULMONARY EDEMA:

The embolic pathology induced by the intravenous injection of oleic acid is characterized by a reliable and reproducible dose dependency. This fact was considered in designing the experimental model described later in this thesis(see section 5.2.2). One of the principal

characteristics of NMR imaging is the relatively long scan times required to generate high-quality in-vivo images. These are lengthened further by the incorporation of respiratory-gated data acquisition. Thus it became apparent that in order to acquire sufficent NMR data to reliably quantify and describe pulmonary edema, the experimental animals' survival would have to be assured for at least several hours(~4-5) after the administration of oleic acid.

Extensive histological examinations of the pathology induced by small dosages of oleic acid(0.045 and 0.09 gm/kg, or 0.05 and 0.1 ml/kg) have been performed by Derks and Jacobovitz-Derks(18). These investigators employed dosages sufficiently small to permit survival of the experimental animals for a considerable period of time. Examination of the resulting diseased lung tissue was then carried out at various times over a 48 hour interval, with both light and electron-microscopy. The following was observed with light-microscopy:

1)1 hour: irregularly distributed edematous areas; alveolar capillaries are diffusely congested

2)2-3 hours: edema and capillary congestion are more severe; polymorphonucleocytes have infiltrated the alveolar septae; intravascular fat emboli

3)4 hours: same as above; macrophages have infiltrated the perivascular connective tissue

4)6-12 hours: maximal congestion, edema, hemorrhage, and septal necrosis

5)24 hours: above observations have decreased in severity; remaining edema is prominent in the perivascular areas, macrophages exist in zones of sclerosis

6)48 hours: acute lesions are increasingly less severe

The following was observed with electron-microscopy:

1)1 hour: capillaries obstructed with recent thrombi formed of fibrin, platelets, and cell debris; endothelial and Type II cells are necrotic and separated from their basal membranes; alveolar septal connective tissue is edematous

2)2 hours: erythrophagocytosis and polymorphonucleocytes are in the pulmonary vessels

3)4 hours: capillary obstruction has disappeared; endothelial cells show cytoplasmic modifications; large pinocytotic vacoules are present, as well as myelin-like figures and lipid droplets

4)6-48 hours: above observations persist; Type II cells are normal

The aim of studies involving oleic acid-induced pathology is not to simulate the clinical fat embolism syndrome, but to observe the development of pulmonary patho-anatomical lesions and patho-physiological changes which follow the administration of free fatty acids. The cytotoxicity of free fatty acids is proportional to their degree of unsaturation, and hence, their chemical activity(57). Their site of action has been localized to the intercellular junction, where it has long been known that cohesion between cells is dependent upon the action of calcium ions(61). However, free fatty acids possess a pronounced affinity for calcium ions and quickly immobilize them, resulting in a loss of intercellular cohesion and consequent disruption of the alveolar-capillary membrane(35). This sets in motion a virtual cascade of pathology including surfactant inhibition, edema, hemorrhage, and eventually alveolar collapse(58). The outcome of this is a marked diminution of oxygen transfer.

It has been demonstrated that this resultant hypoxemia may induce 100% fatality within five hours of an intravenous oleic acid injection as small as 0.075 ml/kg, or ~0.067 gm/kg(2). Thus the incorporation of mechanical ventilation and 5 cm H_2O positive end-expiratory pressure is essential for maintaining experimental animal survival after the injection of free fatty acids, both at the aforementioned and larger dosages.

2.1.12 THE MEASUREMENT OF EVLW CONTENT:

The accurate measurement of EVLW in a clinical setting is a difficult endeavour. From a theoretical standpoint, one must be able to determine the fluid component of the blood, which may constitute up to 65% of the total lung weight(21), and subtract this value from the total lung water content. This necessitates determination of the pulmonary hematocrit. The pulmonary blood distribution, and consequently the pulmonary hemotocrit, throughout the lung is unfortunately non-uniform, varying principally along a gravity-dependent axis. Thus, the patient's position must always be considered during any such measurement. Moreover, the pulmonary hematocrit has been shown to be significantly different than that of the peripheral circulation(21,41,60), dictating localized hemotocrit determinations, or appropriate corrective measures when employing peripheral blood samples.

Although two intravascular markers would be ideal, one for the plasma component and one for the erythrocytes, in cases of increased permeability edema, the plasma marker may easily give erroneous results(66), as these are invariably bound to plasma proteins such as albumin. The traditionally chosen erythrocyte marker is hemoglobin(Hb), although radioisotope tracers such as Chromium^{51} (Cr^{51}) have equally been employed over the past two decades. Unfortunately, there is some controversy within the literature regarding the accuracy of the Hb marker. It has been proposed(66) that during analysis of dry homogenized lung tissue, Hb in the supernatant may prove to be artefactually concentrated due to the exclusion of Hb from the water present within the pellet. Consequently, an overestimation of blood volume would result. In addition, although Hb and Cr^{51} have been found to give comparable determinations of blood volume in normal lungs, such has not been the case for hemorrhagic oleic acid-induced edematous lungs, where discrepancies between the two erythrocyte markers may approach 30%(66). Conversely, Julien and co-workers(34) compared Hb and Cr^{51} as intravascular markers under normal conditions, high-pressure edema, and increased permeability edema, and found no difference between the two methods in all three groups.

Investigators have also described spatial distributions of the pulmonary hematocrit varying along a dorsal-ventral axis of the lung(21) while employing Hb as an erythrocyte marker. However, such studies examined the lung following

exsanguination, and after it had been frozen with dry-ice (-79°C.) in a prone position. Freezing with dry-ice possesses several advantages: no perivascular cuffing, alveolar flooding, or any other regional lung water disturbances(21). Of course, there can be no denying that the lung is in fact damaged by such a process, as it exhibits large areas of extravasated blood and grossly distorted histology. More germane to the above discussion is the fact that this method of freezing is relatively slow, such that the freezing of large intact lungs require 24-48 hours for completion. During this time, blood settles to the more gravity-dependent regions of the lung, especially when vessel capacitance has been increased by exsanguination. Consequently, differences between measurements of regional pulmonary hemotocrit, and thus blood volume, would in such circumstances be expected to chiefly reflect post-mortem conditions and not those existent in-vivo. The work of Baile et al.(3) supports this hypothesis.

Assessment of lung mechanics has been traditionally employed for detecting the presence of excess fluid within lung tissues. Unfortunatley, this methodology has thus far failed tc provide a reliable manner for detecting the initial stages of this pathological condition, as perceivable alterations in lung mechanics are present only in patients which exhibit roentgenographic and ausculatory characteristics of late pulmonary edema. Moreover, this technique is incapable of providing any quantitative

measurements of existing edema fluid.

Alterations in alveolar gas exchange similarily occur with the onset of lung edema. However, these are not at all specific to this disease process and are consequently of limited use.

Single and multiple indicator-dilution techniques have been developed which involve markers or tracers that are non-exchangable with alveolar gas. These are intravascularly injected and their concentration measured, either in the pulmonary arterial blood or, if they are γ-ray emitting, by appropriate external probes or cameras. The simplicity of these techniques, from both a mathematical and experimental viewpoint, has continued to attract interest. Despite considerable refinement over the past two decades, these techniques' measurements of lung water have however proved frustrating. Thus, these procedures remain more investigative tools than clinical ones.

In more practical terms, further limitations preventing accurate clinical measurements of EVLW include a host of complicated equipment and maneouvers at the bedside. Consequently, non-invasive diagnostic imaging becomes an attractive alternative with which to assess pulmonary edema. However, there are considerable limitations to currently available methodologies.

Thoracic roentgenography is most often relied on clinically for the detection and assessment of pulmonary edema, although the inability to quantify radiographic

findings significantly reduces the efficiency of this technique. It has been estimated that at least a 30% change in EVLW is required before detection via roentgenography is achieved(66). As such, one may well question whether this technique is capable of distinquishing between vascular congestion, atelectasis, and bonafide edema.

Computerized tomography(CT), while possessing better spatial localization capabilities than roentgenography, determines image contrast by differences in spatial density. Thus it too requires pronounced changes in EVLW to prove of clinical benefit. In addition, CT cannot distinquish between extravascular and intravascular lung water without the administration of appropriate intravascular markers.

With these technical limitations, and the above described theoretical and practical considerations, it is not surprising that, at a 1980 convention workshop devoted to the clinical measurement of EVLW, it was stated: "current methods for measuring lung water content in man are limited, by both methodological and population variances, to accuracies and sensitivities of about 20-30%"(66). It is clear that, although this level of sensitivity is adequate to measure extensive pulmonary edema, it represents a serious limitation for the detection of early interstitial fluid accumulation. Therefore, the development of an imaging modality capable of both spatially visualizing and quantifying the early alterations of EVLW content associated with disease is clearly warranted.

THE THEORY OF NUCLEAR MAGNETIC RESONANCE (NMR) IMAGING

2.2.1 BASIC NMR THEORY:

The phenomenon of Nuclear Magnetic Resonance(NMR) is a consequence of all atomic nuclei presenting constituents (protons and neutrons) with magnetic properties. More importantly, there are many nuclear species in which these constituents are unpaired. Such bodies therefore possess both a nuclear magnetic moment and a spin angular momentum. These two quantites are related, one to another, in such a fashion as to form a descriptive parameter, the gyromagnetic ratio, which is unique for each nuclear species:

$$[\underline{\mu} / I(\hbar/2\pi)] = \gamma \qquad (2.2.1)$$

where $\underline{\mu}$ is the nuclear magnetic moment, I is the nuclear spin quantum number, h is Planck's constant(6.63×10^{-34} joule-sec), and γ is the gyromagnetic ratio, expressed in radians seconds^{-1} Tesla^{-1}.

When placed within an externally-applied magnetic field, B_0, the spin angular momentum induces such nuclei to precess about the axis of B_0 as they experience the torque of B_0 acting on their spin magnetic moment. This phenomenon is analogous to a top, with its angular momentum existing along its spinning axis, precessing about the Earth's

gravitational field. Furthermore, quantum mechanics dictates that the orientation of the nuclear spin magnetic moment, with respect to B_0, be quantized.

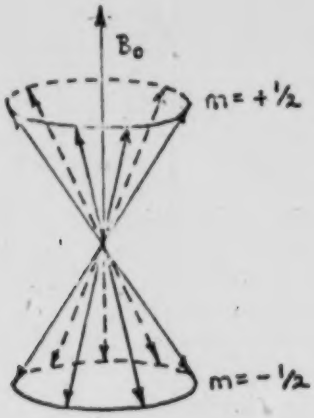

FIGURE 2.2.1: The possible orientations that may be taken by the magnetic moments of a nucleus with I = 1/2 when placed in an externally-applied magnetic field, B_0.

The number of allowed orientations is 2I + 1. For example, since H^1 has an I value of 1/2, its nuclear spins are thus restricted to two orientations. The components of the magnetic moment parallel to the angular momentum vector $[I(I-1)]^{1/2}$ cannot be measured as they are not collinear with B_0. Instead, these components exist at some discrete angle such that they precess about B_0 on the surface of a cone, with its axis either parallel or anti-parallel to the externally-applied magnetic field(see Fig. 2.2.1). The energy difference between these two orientations is:

$$\Delta E = \gamma(h/2\pi)B_0 \qquad (2.2.2)$$

Since the energy exchange between the nuclear spin system and the external environment is a thermally balanced phenomenon, the spin populations follow a Boltzmann distribution. When B_0 is small in magnitude, such as that of the earth(0.5×10^{-4}T), the energy dissipated by molecular rotation and/or tumbling is sufficient to induce transitions from one energy state to another. Under such conditions, Maxwell-Boltzmann statistics dictate that the population difference between nuclei in these two states is small, though certainly discernable. However, if B_0 is of appreciable magnitude, 2.35T, a significant excess number of nuclei will align parallel to the field. B_0 is, in this case, sufficiently large that transitions from one energy state to another are not so easily induced as described above, and thus a small majority of nuclei will reside in the lower energy state, parallel to B_0. As the population ratio of these two states is dependent on the absolute temperature and B_0, it follows that:

$$(n_\alpha/n_\beta) = e^{-\Delta E/kT} = e^{-\gamma(h/2\pi)(B_0/kT)} \qquad (2.2.3)$$

where n_α and n_β are the population of nuclei in the lower and upper energy states respectively, k is the Boltzmann constant (1.38×10^{-23} joule molecule^{-1} °K.), and T is the absolute temperature(see Fig. 2.2.2).

A simple model suggests that transitions from one energy state to another may be induced if sufficient energy is received to satisfy the Bohr frequency condition and, in so doing, reverse the orientation of $\underline{\mu}$.

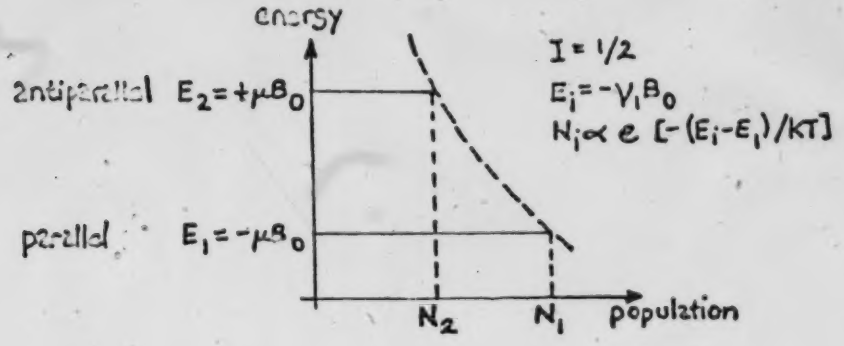

FIGURE 2.2.2: The population distribution of nuclear magnetic moments positioned parallel and anti-parallel to the orientation of an externally-applied magnetic field, B_0 , where $\nu = \omega_0/2\pi$.

This can be stated as:

$$\Delta E = (h/2\pi)\omega_0 \qquad (2.2.4)$$

where ω_0 is the angular precessional frequency of the nuclear spin magnetic moment(see Eq. 2.2.6 and Fig. 2.2.3). This suggests that such transitions can be brought about through application of electromagnetic irradiation of angular frequency ω_0, such that from equations 2.2.2 and 2.2.4:

$$(h/2\pi)\omega_0 = \gamma(h/2\pi)B_0 \qquad (2.2.5)$$

which leads to:

$$\omega_0 = \gamma B_0 \qquad (2.2.6)$$

The above is a description of the resonance condition. The resonance frequency, ω_0, is termed the Larmor frequency and is uniquely determined by γ and B_0. Each nuclear species will therefore possess a unique precessional frequency within a given B_0. The fact that ω possesses a marked sensitivity to $B_{experienced}$ provides NMR with its discriminating qualities between nuclei in slightly different magnetic environments. For nuclei commonly investigated with NMR techniques, ω_0 exists between zero to several hundred megahertz(MHz), in magnetic fields of typically available spectroscopy and imaging systems, and thus falls into the radiowave portion of the electromagnetic spectrum.

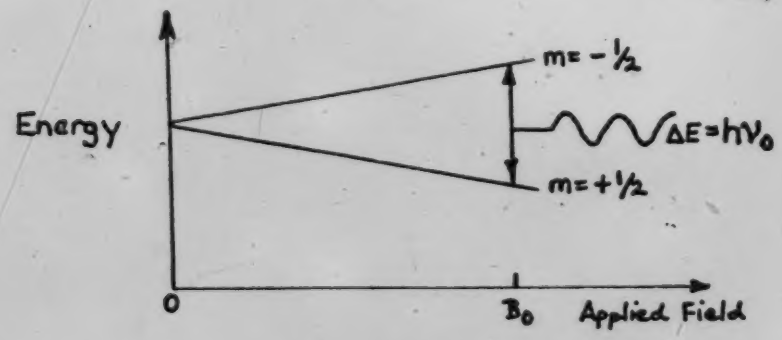

FIGURE 2.2.3: The respective energies of the two orientations outlined in FIGURE 2.2.2 for a nucleus with I = 1/2, expressed as a function of the externally-applied magnetic field, B_0 .

As outlined previously, when nuclei possessing a spin of 1/2 are placed within a sufficiently large B_0, a small majority will align parallel to the axis of B_0. When one considers the vector sum of these identical nuclear magnetic moments aligning parallel to the axis of B_0 over a unit volume, one is in fact considering a macroscopic magnetization vector, $\underline{M}$ (see Fig. 2.2.4). This $\underline{M}$ obeys the Larmor relationship and precesses about B_0 at the angular frequency ω_0. Since nuclear magnetic moments in this state are parallel to B_0, $\underline{M}$ will also parallel B_0 at thermal equilibrium. If spin interactions are neglected, the change in $\underline{M}$ with respect to time can be expressed as:

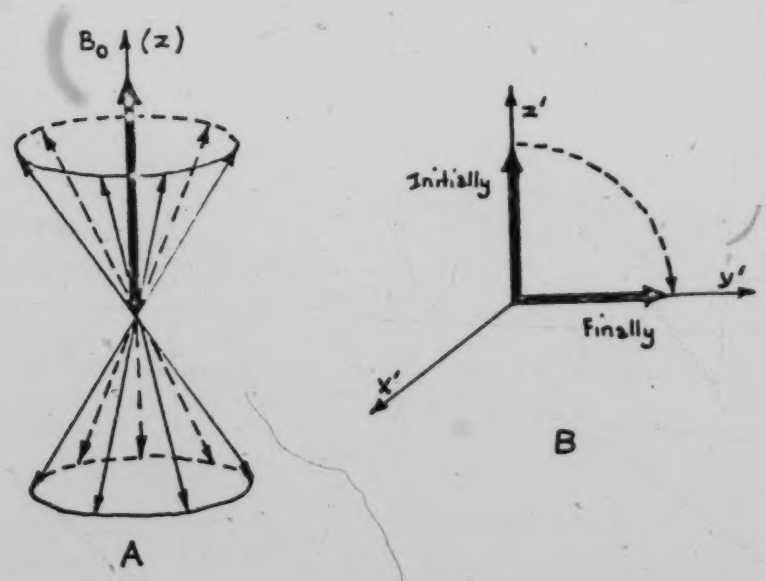

FIGURE 2.2.4A: The macroscopic magnetization vector, $\underline{M}$ (denoted by the large arrow pointing upwards along the Z-axis of the laboratory frame).

FIGURE 2.2.4B: The effect upon this magnetization vector by an RF pulse of sufficient duration to re-orient $\underline{M}$ perpendicular to the Z'-axis of the rotating frame.

$$d\underline{M}/dt = \underline{M} \times (\gamma B_0) \qquad (2.2.7)$$

In NMR experimentation, it is the behaviour of this macroscopic magnetization vector that one is primarily concerned with, both as one forcibly rotates it by applying appropriate electromagnetic irradiation and as it precesses and relaxes back towards thermal equilibrium.

Although a complete description of such NMR phenomena requires the employment of quantum mechanics, certain aspects of this description can be understood adequately and clearly in terms of classical physics. Consequently, the following discussion will contain a mixture of the two; that chosen in any one instance will be dependent upon which provides the simpler, or more helpful, picture of what is being described.

2.2.2 THE ROTATING FRAME OF REFERENCE:

A major problem in attempting to visualize the motion of the macroscopic magnetization vector in a static magnetic field existing in the laboratory frame of reference, is that all perturbations towards or away from the B_0 axis are superimposed on the rapid Larmor precession itself. However, the effect of the static field may be removed by working within a co-ordinate system precessing about B_0 at an

angular frequency ω_0. In this rotating frame of reference, the nuclear spins will not appear to precess at all, but rather to remain stationary. Consequently, the transformation to the rotating frame greatly simplifies the overall understanding of the NMR experiment.

The mathematical argument for the rotating frame is as follows. The macroscopic magnetization vector is a function of time, $\underline{M}(t)$, and can be thought of as being separated into components along the right-handed cartesian co-ordinates:

$$\underline{M}(t) = \underline{i}M_x(t) + \underline{j}M_y(t) + \underline{k}M_z(t) \qquad (2.2.8)$$

where $\underline{i}$, $\underline{j}$, and $\underline{k}$ are orthogonal unit vectors of the laboratory frame which can, at most, rotate with an instantaneous angular velocity $\underline{\omega}$:

$$\delta\underline{i}/\delta t = \underline{\omega} \times \underline{i}\ ,\ \delta\underline{j}/\delta t = \underline{\omega} \times \underline{j}\ ,\ \delta\underline{k}/\delta t = \underline{\omega} \times \underline{k} \qquad (2.2.9)$$

The time derivative of $\underline{M}(t)$ in the laboratory frame is:

$$\begin{aligned} d\underline{M}/dt &= \underline{i}\delta M_x/\delta t + M_x\delta\underline{i}/\delta t + \underline{j}\delta M_y/\delta t \\ &\quad + M_y\delta\underline{j}/\delta t + \underline{k}\delta M_z/\delta t + M_z\delta\underline{k}/\delta t \\ &= \underline{i}\delta M_x/\delta t + \underline{j}\delta M_y/\delta t + \underline{k}\delta M_z/\delta t \\ &\quad + [\underline{\omega} \times (\underline{i}M_x + \underline{j}M_y + \underline{k}M_z)] \\ &= \delta\underline{M}/\delta t + (\underline{\omega} \times \underline{M}) \end{aligned} \qquad (2.2.10)$$

where $\delta\underline{M}/\delta t$ represents the time rate of change for $\underline{M}$ with

respect to the co-ordinate system $\underline{i}$, $\underline{j}$, and $\underline{k}$.

When considering the rotating frame of reference, one may conclude, from Eqs. 2.2.7 and 2.2.10, that:

$$\delta\underline{M}/\delta t + (\underline{\omega} \times M) = \underline{M} \times (\gamma \underline{B}_0)$$
$$\delta\underline{M}/\delta t = \underline{M} \times \gamma(B_0 - \omega/\gamma) \qquad (2.2.11)$$

where the terms in parentheses may be thought of as representing the effective magnetic field, $\underline{B}_{eff}$. This reveals that, in the rotating frame, $\underline{M}$ will precess about $\underline{B}_{eff}$ at an angular frequency equal to $\gamma\underline{B}_{eff}$. Such a situation is exactly analoqous to the precession of $\underline{M}$ about $\underline{B}_0$ within the laboratory frame. Thus, at the Larmor frequency, the precession of the rotating frame is in the same sense and at the same rate as that of the macroscopic magnetization vector. Hence:

$$\underline{\omega} = -\gamma B_0 \underline{k} \qquad (2.2.12)$$

In such a situation, $\underline{B}_{eff} = 0$, $\delta\underline{M}/\delta t = 0$, and $\underline{M}$ remains stationary with respect to the orthogonal unit vectors $\underline{i}$, $\underline{j}$, and $\underline{k}$. Finally, these above three unit vectors rotate at ω_0 with respect to the laboratory frame of reference.

2.2.3 THE EFFECT OF ROTATING MAGNETIC FIELDS:

As described in section 2.2.1, transitions between the two permitted energy states, when I = 1/2, may be induced by applying an oscillating, or rotating, magnetic field of angular frequency ω, that satisfies equation 2.2.4.

This applied magnetic field, produced by electromagnetic irradiation, is defined by:

$$\underline{B}(t) = \underline{i}2B_1(t)\cos \omega t \qquad (2.2.13)$$

and is described as having two components, each of amplitude B_1. One of these rotates in a clockwise fashion, the other counter-clockwise. This situation is equivalent to the splitting of plane-polarized light into left and right-handed circularly-polarized components. The two components of B_1 may be stated as:

$$B_{clockwise} = B_1(\underline{i}\cos \omega t - \underline{j}\sin \omega t)$$
$$B_{counter\text{-}clockwise} = B_1(\underline{i}\cos \omega t + \underline{j}\sin \omega t) \qquad (2.2.14)$$

The clockwise component will thus rotate in the same sense as the nuclear spins' precession, while the counter-clockwise component will rotate in the opposite sense. At the Larmor frequency, ω_0, $B_{counter\text{-}clockwise}$ may be ignored since its overall effect is negligible. Moreover, since $B_{clockwise}$ and $B_{counter\text{-}clockwise}$ differ only in their

direction of rotation, there is no loss in completeness in considering only one component of $\underline{B}(t)$. Therefore the applied rotating magnetic field can be described as:

$$B_1(t) = B(\underline{i}\cos \omega t - \underline{j}\sin \omega t) \qquad (2.2.15)$$

In combining $\underline{B}_1(t)$ and the observation that $\underline{M}_0$ in thermal equilibrium points along the $\underline{k}$ axis($\underline{B}_0 = B_0\underline{k}$), equation 2.2.7 becomes within the laboratory frame:

$$d\underline{M}/dt = \underline{M} \times \gamma[\underline{B}_0 + \underline{B}_1(t)] \qquad (2.2.16)$$

The above represents the equation of motion for the macroscopic magnetization vector within the laboratory frame of reference.

When one considers the rotating frame, and arbitrarily positions $\underline{B}_1$ along the X' axis, equation 2.2.16 becomes:

$$\begin{aligned} \delta\underline{M}/\delta t &= \underline{M} \times [\underline{k}(\omega - \gamma B_0) + \underline{i}\gamma B_1] \\ &= \underline{M} \times \gamma \underline{B}_{eff} \end{aligned} \qquad (2.2.17)$$

where:

$$\underline{B}_{eff} = \underline{k}(B_0 - \omega/\gamma) + \underline{i}B_1 \qquad (2.2.18)$$

The macroscopic magnetization vector will precess in a cone of half-angle θ about $\underline{B}_{eff}$(see Fig. 2.2.5) at an

angular frequency $\gamma \underline{B}_{eff}$, where θ is defined as:

$$\theta = \tan^{-1}[B_1/(B_0 - \omega/\gamma)] \qquad (2.2.19)$$

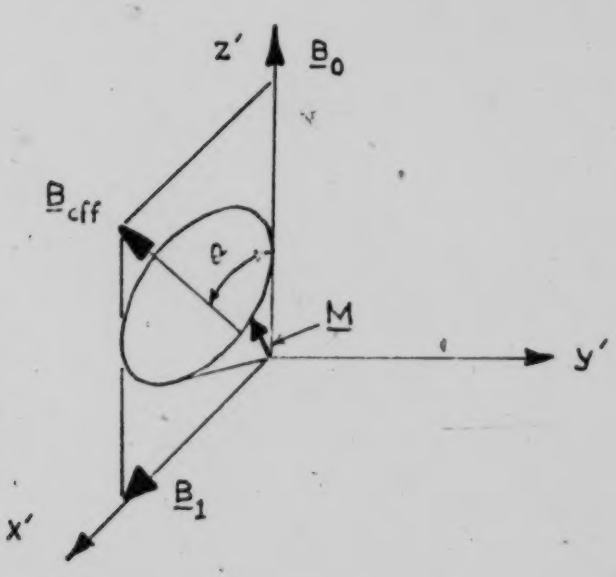

FIGURE 2.2.5: The effective magnetic field, $\underline{B}_{eff}$, and the precession of the magnetization vector $\underline{M}$ about it, within the rotating frame of reference.

The equality of the Larmor frequency and the angular resonance frequency of the B_1 field is analogous to other resonance phenomena for which the "driving" frequency is equal to a characteristic frequency of the system in question.

If the resonance condition is exactly met, i.e. $\omega_{rf} = \omega_0$, then $\underline{B}_{eff} = \underline{i}B_1$. B_1 will now exert a torque on the macroscopic magnetization and will perturb it away from its initial position parallel to $\underline{B}_0$. The magnetization will now precess in a plane perpendicular to the $\underline{B}_1$ direction. The

angle through which the magnetization precesses is dependent upon the duration of the $\underline{B}_1$ field:

$$\theta = \gamma B_1 t_\omega \qquad (2.2.20)$$

where t_ω is the duration of the $\underline{B}_1$ field. Following the application of a $\underline{B}_1$ field of duration t_ω, the X'-Y' component of the total resultant magnetization(see Fig. 2.2.6) is described by:

$$M_{x'-y'} = M_0 \sin \omega t \qquad (2.2.21)$$

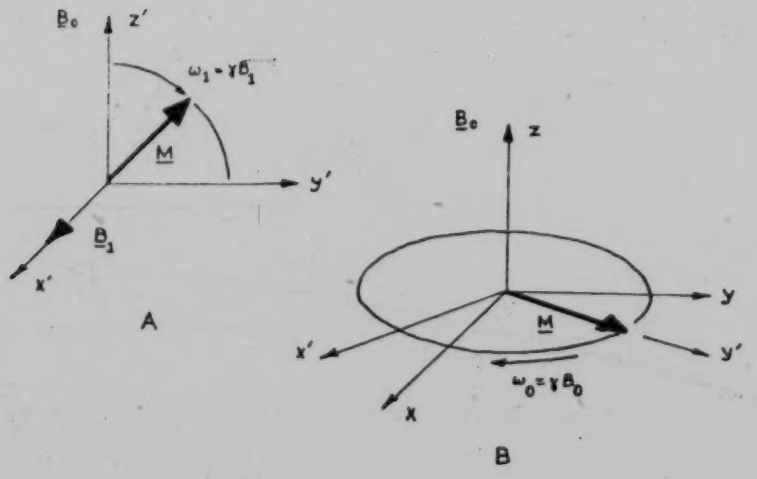

FIGURE 2.2.6A: The application of a $\underline{B}_1$ magnetic field as manifested through the application of an RF pulse, with time duration t_ω.

FIGURE 2.2.6B: The resultant effect of this applied $\underline{B}_1$ field upon the magnetization vector $\underline{M}$.

2.2.4 DETECTION OF THE NMR SIGNAL:

In the absence of any externally-applied $\underline{B}_1$ field and its consequent perturbation of the nuclear spins, the nuclear spins precess about $\underline{B}_0$ at their characteristic Larmor frequency. At any moment in time, the net component of macroscopic magnetization in any direction within the XY plane of the laboratory frame is small. Therefore, little NMR signal is detected in a circumferential receiver coil, which has to be oriented perpendicular to the direction of $\underline{B}_0$. As described previously, an externally-applied $\underline{B}_1$ field, in the form of an RF pulse, will tilt the net nuclear magnetization away from the Z-axis, through an angle θ, towards the XY plane of the laboratory frame or the X'-Y' plane of the rotating frame of reference(see Fig. 2.2.7a).

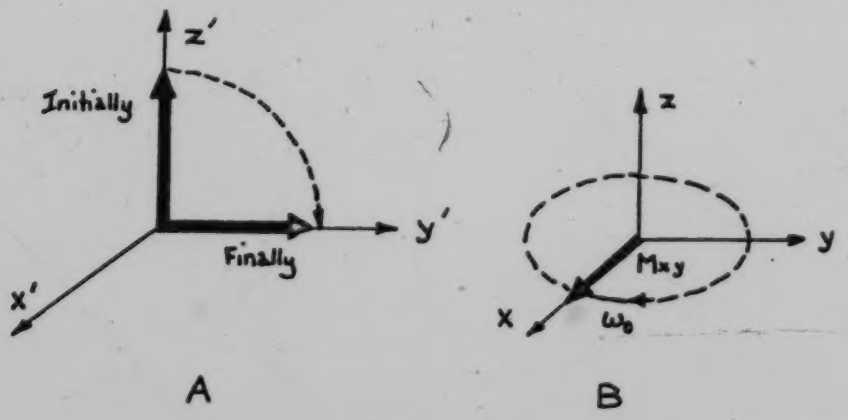

FIGURE 2.2.7A: The effect of the applied $\underline{B}_1$ field in tilting the net nuclear magnetization away from the Z'-axis of the rotating frame.

FIGURE 2.2.7B: The X'Y' components of magnetization, produced as a result of the applied $\underline{B}_1$ field, rotating about the Z - axis with angular frequency ω_0.

Following the termination of this RF pulse, the nuclear spins will experience only the effects of B_0 and thus will continue to precess about its axis. However, a net component of magnetization, M_{x-y}, has now been created in the X-Y plane(see Fig. 2.2.7b). In so doing, a voltage or electromotive force(emf), oscillating at ω_0, will be induced in the above described receiver coil, in complete analogy to an electrical generator. The magnitude of this emf is dictated by Faraday's law of magnetic induction, which states that the emf in a circuit is proportional to the rate at which the magnetic flux changes through the circuit. Thus the amplitude of this induced emf is proportional to M_{x-y}. Hence the NMR signal induced in a receiver coil, oriented around the sample along the Z-axis of the laboratory frame, will increase for longer t_ω, achieving a maximum for $\theta = \pi/2$, where $\sin\omega t = 1$. The application of such electromagnetic irradiation is described as a $\pi/2$ or 90° radio-frequency(RF) pulse. With further increase in t_ω, $\underline{M}$ will precess through increasingly larger angles relative to $\underline{B_0}$. The acquired NMR signal will continually decrease, achieving zero for a π or 180° RF pulse, where $\sin\omega t = 0$.

Under ideal circumstances, the constituent magnetic moments of the net magnetization would continue to rotate about $\underline{B_0}$ in a coherent fashion and M_{x-y} would retain its initial amplitude, or that existing at the termination ofthe RF pulse. However, in more realistic situations, the constituent magnetic moments begin to dephase due to the

effects of inhomgeneities of the $\underline{B}_0$ field, and to tranverse magnetization relaxation processes(see section 2.2.5). Consequently M_{x-y} decreases with time after the termination of the RF pulse, thus producing a continually diminishing emf. This decaying emf signal is a free precession signal and, owing to its decay in the absence of any $\underline{B}_1$ effects, is described as a free induction decay(FID).

In most instances, the NMR signal is detected in quadrature: the signal and reference channel inputs, the latter of which is phase shifted by 90° relative to the former, are passed to two nominally identical phase sensitive detectors with the outputs being amplified, digitized, and stored in memory blocks as real and imaginary components of the FID. Signal components above and below ω_0 are spread over a finite band about ω_0 in the frequency domain. This band is shifted and centered about $2\omega_0$ and 0 radians second^{-1} by multiplying the acquired signal by a reference frequency ω_0. This is subsequently passed through a low-pass filter to retain only those components centered about 0 radians second^{-1}($\omega = 0$). After the real and imaginary components of the FID are analysed via the process of complex Fourier transformation, they may be resolved into its real and imaginary components in a frequency spectrum centered at $\omega = 0$. This is the origin about which any signal may be detected at either $+\Delta\omega$ or $-\Delta\omega$. The above technique is termed Quadrature Phase Sensitive Detection (QPSD).

Since the QPSD reference channel and the acquired nuclear signal are often times not at the same frequency, the observed FID is commonly in the form of a beat pattern corresponding to the difference in frequencies between the QPSD reference channel and that of the acquired nuclear signal(see Fig. 2.2.8a). This NMR signal initially exists within the time domain. However, by use of Fourier transformation, a frequency spectrum may be derived from the acquired FID waveform. The obtained frequency spectrum is typically a bell-shaped curve in fluid, single species systems, whose actual shape is dependent upon the exact nature of the decay(see Fig. 2.2.8b). For example, an exponential FID in time will give rise to a Lorentzian shape of the frequency spectrum.

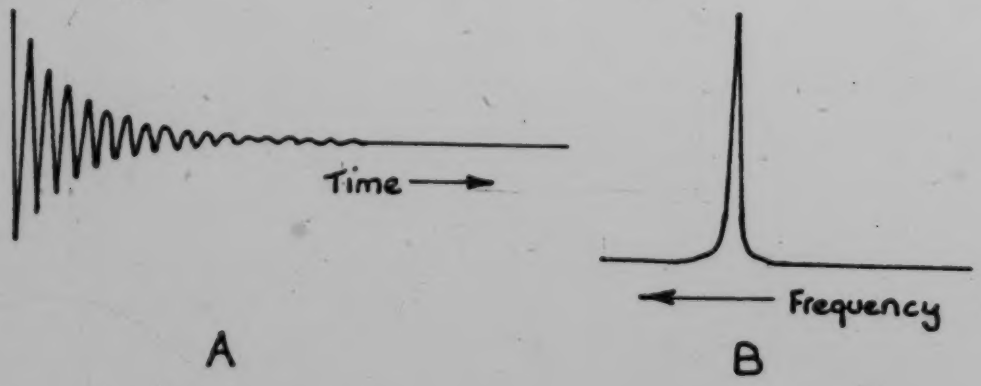

FIGURE 2.2.8A: An FID waveform.

FIGURE 2.2.8B: The frequency spectrum, following Fourier transformation, derived from the FID waveform depicted in FIGURE 2.2.8A.

2.2.5 THE BLOCH EQUATIONS:

When the magnitude of the interactions between neighbouring nuclei are dominant, the duration of the corresponding FID is very short and the practical requirements of NMR imaging become severe. Therefore, an analytical technique such as NMR imaging proves optimal under conditions where the effective nuclear interactions are weak and the acquired FIDs are appreciably long and typically exponential in character. These are the existing conditions for the majority of NMR's biomedical applications. In situations such as these, the behaviour of the resultant nuclear magnetization may be described by a phenomenological model outlined in 1946 by Felix Bloch.

This model is a set of simple equations derived from phenomenological arguments, proposed for the description of the magnetic properties of nuclei within externally-applied magnetic fields. Moreover, for the liquid systems associated with the biomedical applications of NMR, these equations have, in most cases, provided a correct quantitative description of the phenomena's detailed behaviour.

The first portion of the model proposed by Bloch assumes that the motion of the macroscopic magnetization, within a static, homogeneous magnetic field, may be superimposed on the motion of the free spin magnetization and expressed as:

$$d\underline{M}/dt = \underline{M} \times \gamma \underline{B}_0 \qquad (2.2.22)$$

When one considers the recovery of thermal equilibrium after an RF pulse perturbation, the following must be assumed:

1)The rate of recovery, which can be expressed as dX/dt, is proportional to the initial displacement from thermal equilibrium. By analogy, this may be stated as:

$$dX/dt = k[(X_0 - X(t)] \qquad (2.2.23)$$

where X_0 is the thermal equilibrium value of a variable x(t).

2)One would therefore anticipate M_z being established according to:

$$dM_z/dt = (M_0 - M_z)/T_1 \qquad (2.2.24)$$

where T_1 is the time constant for the longitudinal recovery of M_z, which has an equilibrium value of M_0.

3)Since the thermal equilibrium value of the transverse magnetization is zero, it decays at a rate described by:

$$dM_x/dt = -M_x/T_2 \quad \text{and} \quad dM_y/dt = -M_y/T_2 \qquad (2.2.25)$$

where T_2 is the time constant for the transverse relaxation of M_x and M_y.

Thus, by combining the torque applied by the magnetic field on M with an exponential relaxation of the XY components(M_x and M_y) and the longitudinal recovery of the XZ component, one obtains the Bloch equation in the laboratory frame:

$$d\underline{M}/dt = \underline{M} \times \gamma\underline{B} - \left[M_x\underline{i} + M_y\underline{j} \right]/T_2 + \left[M_z - M_0 \right] \underline{k}/T_1 \qquad (2.2.26)$$

where $\underline{i}$, $\underline{j}$, and $\underline{k}$ are unit vectors. The above equation may be stated in terms of its three components, existing along the X, Y, and Z axes. During NMR imaging, B will consist of B_0, $B_1(t)$, and $B_g(x,y,z)$, the last representing the magnetic field created by linear gradients. At this point let us accept on faith that throughout RF excitation the influence of B_g may be minimized(see section 2.2.10 for a detailed description), whereas between RF pulses $B_1(t)$ is zero. Thus, there are at least two formats of the Bloch equation applicable to NMR imaging. The two formats are that corresponding to a time-dependent B and that corresponding to a time-independent B.

Occassionally, additional terms are added to the above general equation to describe the effects of phenomena such as diffusion within a linear gradient, but these remain outside the scope of this discussion. More importantly, one must always bear in mind the limited validity of the Bloch model, for there are numerous instances where its governing assumptions and conditions are not applicable.

2.2.6 MAGNETIZATION RELAXATION PROCESSES:

The return of M_z to thermal equilibrium is termed the spin-lattice, or longitudinal, magnetization relaxation. The term spin-lattice relaxation refers to the fact that energy received during RF pulse excitation is, after termination of that pulse, eventually lost through interactions of the nuclear spins with their surroundings, collectively labelled the "lattice". However, for the purposes of this discussion we will refer to this phenomenon as the longitudinal relaxation since the return of M to thermal equilibrium results in a corresponding recovery of the magnetization parallel to $\underline{B}_0$, termed M_z. The return of the nuclear spins to thermal equilibrium often, but not always, describes an exponential function.

The recovery of M_z may be stated as:

$$[dM_z(t)/dt] = k[M_0 - M_z(t)] \qquad (2.2.27)$$

where k is a constant. This leads to the following solution when the recovery precedes from the termination of a 90° RF pulse, or when $M_z(t) = 0$:

$$M_z(t) = M_0[1-e^{-kt}] \qquad (2.2.28)$$

If the return of the nuclear spins to thermal equilibrium indeed follows an exponential function, then k may be derived in terms of a characteristic time constant T_1, i.e. $T_1=k^{-1}$, such that:

$$M_z(t) = M_0(1-e^{-t/T_1}) \qquad (2.2.29)$$

All mechanisms for longitudinal relaxation involve thermal motion inducing a modulation of the magnetic interaction associated with the nuclear spins. When modulated, this magnetic interaction, which may be interpreted in terms of a local magnetic field(b_{local}), gives rise to a time-varying magnetic field at each nuclear site. Upon Fourier transformation, there is found a component of this time-varying field at $_0$. It is this component which induces transitions between the individual nuclear energy states and, in so doing, establishes the process of magnetization relaxation.

Energy conservation is observed throughout the entire NMR phenomenon, as the energy received by the nuclear spins during RF excitation is, following the termination of the RF

pulse, exchanged between the nuclear spin system and the surrounding thermal energy bath. This thermal energy bath is always very close to thermal equilibrium because of its large thermal capacity. Thus, there are more molecular motions existing at a lower energy state, able to receive energy from the nuclear spins, than there are those existing at higher energy states capable of supplying it to the involved nuclear spins. Magnetic interactions between the nuclear spins and their surroundings therefore tend to act as net "relaxers", rather than "exciters", of the particular spin system in question.

If one considers a pair of nuclear spins, infinitely far apart from each other and then brought together to a normal internuclear distance within a molecule, one obtains an energy of interaction(E_I) that is a constant for a particular molecular arrangement. If this E_I is time-dependent then it will be distributed in both frequency and time when the involved spins are induced to move randomly with respect to one another. This frequency dependence of the power spectrum of the motion is termed the spectral density, $J(\omega)$, and is influential in determining T_1^{-1} at the Larmor frequency for a particular nucleus. Unfortunately, the calculation of $J(\omega)$ is extremely complex, as molecular motion is difficult to describe exactly. Such motion is not completely random, and may even be anisotropic, due to interactions between atoms and molecules. $J(\omega)$ may be described for a stationary random process with an

exponential correlation function as:

$$J(\omega) = \tau_c/(1 + \omega^2 \tau_c^2) \qquad (2.2.30)$$

where τ_c is the correlation time and characterizes the involved molecular motion. Such a description assumes that when such molecular motion, be it rotational or translational, occurs very rapidly, τ_c is short, and when the molecular motion is slow, τ_c is long. Thus, for a given τ_c, pressure, and temperature, $J(\omega)$ may be considered as a constant for small values of ω ,and then trails off proportional to ω^{-2} for large values of ω(see Fig. 2.2.9).

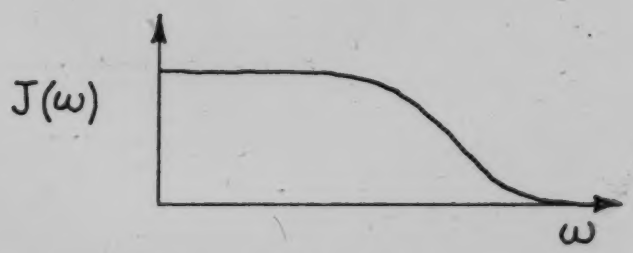

FIGURE 2.2.9: The spectral density function, $J(\omega)$, represented as a function of angular frequency ω, for T_1 magnetization relaxation processes.

Temperature is influential in determining the shape of the curve for $J(\omega)$, but not the area under it, hence $J(\omega)d\omega$ remains constant. At low temperatures, $J(\omega)$ will appear restricted to the lower values of ω, yet will spread out over a continually increasing range of angular frequencies as temperature increases. Since dipole-dipole interactions can induce transitions at both ω_0 and $2\omega_0$, it follwos that:

$$W = k[J(\omega_0) + J(2\omega_0)] \qquad (2.2.31)$$

where W is the total transition probability per unit time. Moreover, since $W \propto T_1^{-1}$, then:

$$T_1^{-1} = k\left[\frac{\tau_c}{1 + \omega_0^2 \tau_c^2} + \frac{4\tau_c}{1 + 4\omega_0^2 \tau_c^2}\right] \qquad (2.2.32)$$

If one were to sample $J(\omega)$ at a specific ω, e.g. at ω_0(or the Larmor frequency) T_1^{-1} would achieve a maximum at a particular temperature(see Fig. 2.2.10). This corresponds to the temperature at which the $J(\omega)$ contribution, at the Larmor frequency, is maximal. It is thus during this condition, when $\omega_0\tau_c = 0.62$(or ~1), that the relaxation processes will be more efficient. Under these conditions the molecular motion "tunes in" with the system's resonance frequency at this temperature. For biomedical applications, one is primarily concerned with fluid systems and hence

$\tau_c << \omega_0^{-1}$ or $\omega_0 << \tau_c^{-1}$. This corresponds to the high temperature region(~300°K.).

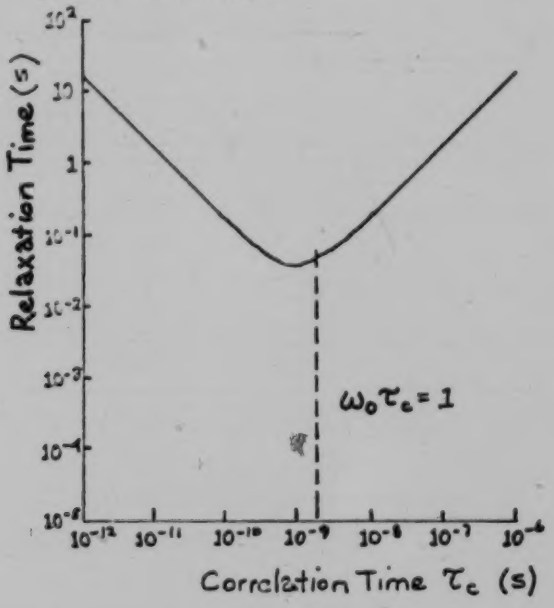

FIGURE 2.2.10: A depiction of the relationship between the proton longitudinal relaxation time T_1 and the correlation time, τ_c.

Spin-spin, or transverse, magnetization relaxation is a process which involves the magnetization within the XY plane of the laboratory frame, or M_{xy}. In contrast to longitudinal relaxation, transverse relaxation is, often times, not adequately described as a single exponential function. This is commonly attributed to compartmentalization effects, or situations in which the nuclei possessing different values of τ_c are physically separated. Moreover, τ_c for the various compartments in these situations is appreciably long relative to the rate of transverse relaxation(R_2). Consequently, τ_c may influence R_2 to such an extent that the acquired FID waveform may be resolved into either a number

of different exponential functions or into non-exponential (e.g. Gaussian) functions.

The transverse relaxation process involves the interaction of neighbouring nuclei, without any exchange of acquired energy, with the surrounding environment. When this process is complete, and thermal equilibrium is achieved, $M_{xy}=0$. Thus, upon termination of the applied RF pulse, the return to thermal equilibrium may be expressed:

$$[dM_{xy}(t)/dt] = -k(M_{xy}) \qquad (2.2.33)$$

where k is a constant. If k is defined in terms of a characteristic relaxation time constant T_2, i.e. $k=T_2^{-1}$, then the solution to the above equation is:

$$M_{xy}(t) = e^{-t/T_2} \qquad (2.2.34)$$

In the ideal case, the transverse magnetization within the rotating frame, $M_{x'-y'}$, would remain static and of constant amplitude. However, in realistic situations a more complex scenerio exists. The individual local magnetic fields(b_{local}) that the nuclei experience, vary appreciably from one nuclear site to another. This may be described as:

$$B_{experienced} = \underline{B_0} \pm b_{local} \qquad (2.2.35)$$

which gives rise to the relationship:

$$\omega_{experienced} = \omega_0 \pm (\gamma b_{local}) \qquad (2.2.36)$$

In terms of the macroscopic magnetization, the important point to be concluded from the above observations is that the individual nuclear magnetic moments will not all precess at the same value of ω. Local magnetic fields which reinforce $\underline{B}_0$ will induce nuclei under their influence to precess at an angular frequency greater than ω_0, while local fields which oppose $\underline{B}_0$ will induce nuclei to precess slower than ω_0. This will cause the individual nuclear magnetic moments within the rotating frame to dephase, or "fan out", one from another. The end result is that the resultant $M_{x'-y'}$ continually decays, as does the magnitude of the induced emf acquired in the receiver coil(see Fig. 2.2.11).

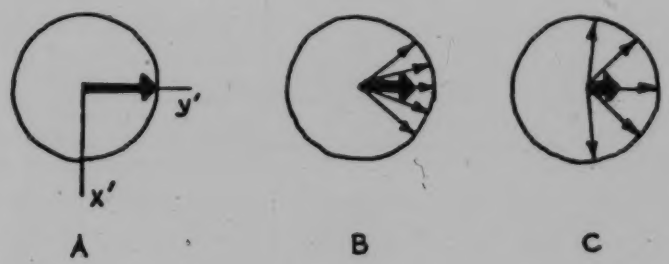

FIGURE 2.2.11: A representation of the dephasing of the individual nuclear magnetic moments, together with the resultant decay of $M_{x'-y'}$, immediately following the application of a 90° RF pulse.

Accurate measurement of T_2 may prove difficult, depending on its actual magnitude. If it is appreciably long, >100 msec, then $\underline{B}_0$ inhomogeneities may contribute to the establishment of various b_{local} values, thus enhancing the dephasing of the nuclear spins within the transverse plane. Transverse relaxation in the presence of $\underline{B}_0$ and B_1 inhomogeneities, in addition to the above sample-related b_{local} processes, may be characterized by the time constant T_2^*. However, the application of RF pulse excitation sequences may be tailored to successfully minimize the adverse effects of $\underline{B}_0$ and B_1 inhomogeneities and consequently maximize the sample-related T_2 processes. Hence, the effects of both $\underline{B}_0$ and $\underline{B}_1$ inhomogeneities are considered reversible, while those consequent to molecular processes within the investigated sample are considered irreversible.

If T_2 represents the time constant describing the M_{xy} exponential decay resulting from transverse relaxation, the following observation may be made concerning the resonance peak linewidth:

$$T_2^{-1} = (\Delta\omega_0/2) = \pi(\Delta\nu_{1/2}) \qquad (2.2.37)$$

where $\Delta\omega_0$ is the spread of angular frequencies for the nuclear magnetic moments dephasing in the transverse plane, and $\Delta\nu_{1/2}$ is the full linewidth at 50% maximum amplitude of the resultant resonance peak. Thus one may conclude that T_2

and resonance linewidths are inherently associated(see Fig. 2.2.12).

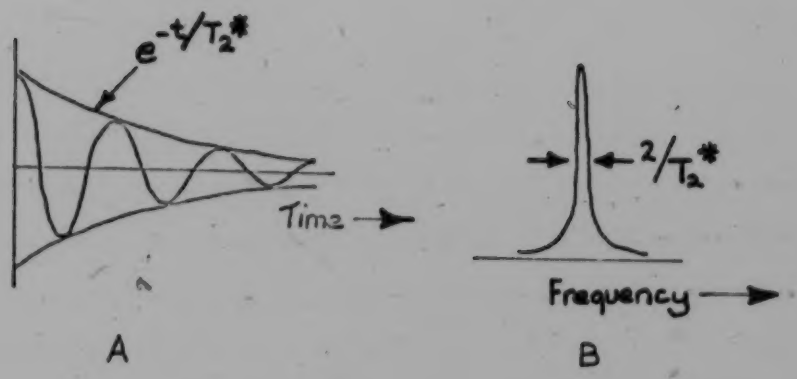

FIGURE 2.2.12: The relationship between the time constant for the dephasing of the transverse magnetization components T_2^* (depicted in A), and the linewidth of the associated proton resonance peak (depicted in B).

Finally, T_2^{-1} is found to be dependent upon both ω_0 and τ_c in a similar fashion to T_1^{-1}. However, there is one important distinction. T_2^{-1} is more influenced by the component of the spectral density at $\omega=0$(see Fig. 2.2.13).This provides T_2 with a considerably greater sensitivity to slower molecular motions.

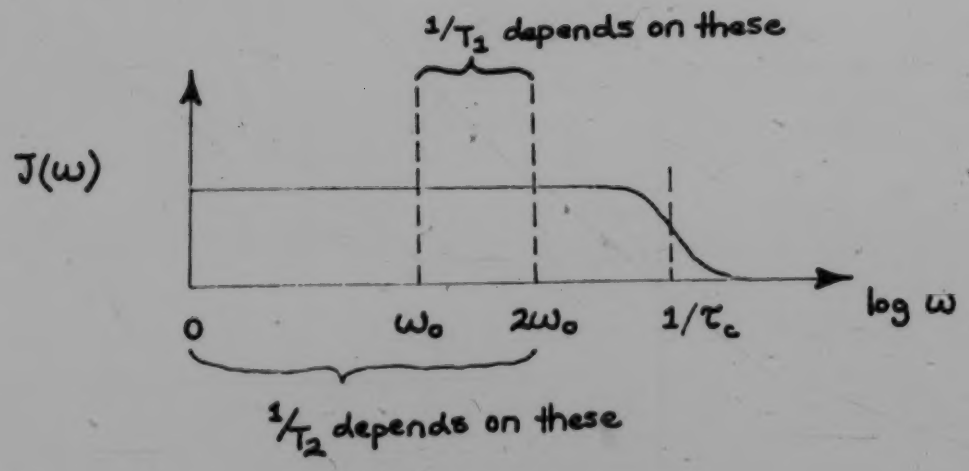

FIGURE 2.2.13: The relationship between the spectral density function, $J(\omega)$, and the angular frequency for transverse magnetization relaxation processes. T_1 is the time constant for longitudinal magnetization relaxation, while T_2 is that for transverse magnetization relaxation.

2.2.7 THE TWO-SITE RAPID EXCHANGE MODEL OF RELAXATION:

The previous section outlined relaxation processes from essentially a theoretical standpoint. Our discussion will now elaborate on these processes as they occur within living tissues, in addition to the model most commonly employed to explain their behaviour under such circumstances.

If P_i denotes the fraction of water present in the ith phase and T_i describes a general relaxation time, then for the slow exchange situation(T_i<< lifetime in the ith phase):

$$M(t) = \sum_{i=1}^{n} P_i e^{-t/T_i} \qquad (2.2.38)$$

where M(t) represents a normalized magnetization. Each phase thus relaxes independently with a characteristic time constant T_i. Such a situation exists in the presence of compartmentalization, where involved nuclei are physically barred from diffusing between the various regions present. For the case of rapid exchange(T_i>> lifetime in the ith phase):

$$M(t) = e[-t/\sum_{i=1}^{n} (P_i/T_i)] \qquad (2.2.39)$$

In such a case the whole system relaxes with a characteristic time constant T_i described by:

$$T_1^{-1} = \sum_{i=1}^{n} (P_i/T_i) \qquad (2.2.40)$$

Most analyses of relaxation data acquired from living tissues assumes that water protons, by far the most influential nuclear species in determining the magnitude of the obtained proton NMR signal, exist in two different phases denoted "bound" and "free"(see Fig. 2.2.14). The majority(>90%) of such protons are considered as being in the free state and exhibit NMR properties similar to those of water possessing an appropriate concentration of cellular salts. The remaining fraction is thought of as being bound to the surface of macromolecules. However, the exact

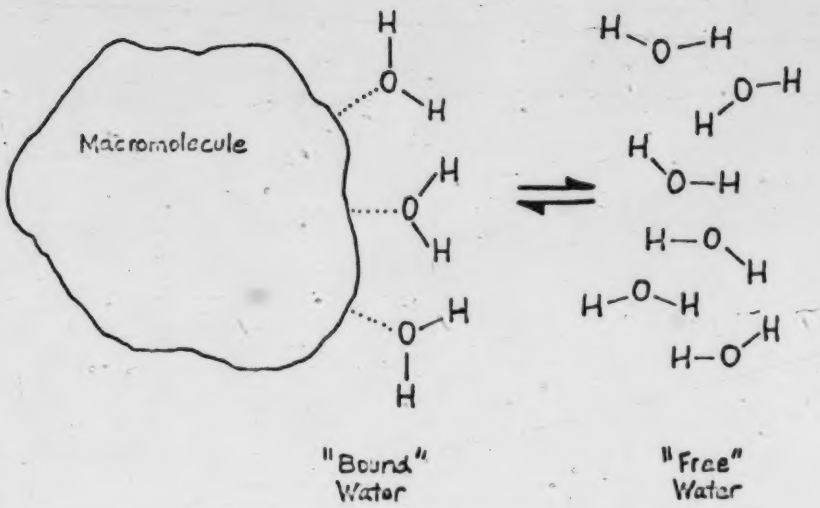

FIGURE 2.2.14: A diagrammatic representation of water protons simultaneously existing in the "bound" and "free" phases.

definition of "bound" varies with the particular model under consideration. It may be that the water protons are rigidly and irrotationally bound or, on the other hand, that they are capable of restricted, possibly anisotropic, motion. The principal evidence for the existence of these two phases for water protons lies in the observation that cooling of tissues below the freezing point of water results in formation of ice from only part of the total cell water (38). This component has been identified directly with the bound phase(4), although such an assignment is certainly not universal among researchers. The magnetic interaction that leads to the relaxation processes is dipolar in origin, although other interaction mechanisms have been suggested.

These include paramagnetic centers bound to macromolecules (32), chemical exchange, and anisotropy of b_{local}(10). The associated correlation times, proposed to explain the obtained relaxation data, fall into three categories:

1)free phase, τ_{cf}: $\sim 10^{-12}$ sec.
2)bound phase, τ_{ob}: $\sim 10^{-9}$-10^{-8} sec.
3)exchange time, τ_e: $\sim 10^{-6}$-10^{-5} sec.

It has been a common observation in biomedical applications of NMR techniques that relatively minor(<10%) changes in tissue water content can elicit dramatic alterations in T_1(~100%). Such findings are indeed consistent with the above described two-site-rapid-exchange model for water proton behaviour. In biomedical applications, where one is chiefly concerned with liquid systems existing at ~300°K., a water proton samples both environments during its characteristic relaxation time. This may be stated as:

$$R_{1_{obs}} = P_a R_{a1} + P_b R_{b1} \qquad (2.2.41)$$

where R is equal to T_1^{-1}, and P_a and P_b are the proportions of water existing in the free and bound phases respectively. In such systems, R_{a1} and R_{b1} may be two orders of magnitude apart. Therefore, subtle, reciprocal alterations in the two values of P would indeed generate large changes in $R_{1_{obs}}$.

One observes the same phenomenon for T_2, although for different reasons. When in the free phase, motion is fast, and averaging of the experienced b_{local} very good. Consequently, T_2 is lengthy. Alternatively, when nuclei are in the bound phase their motion is significantly slower and the averageing of the experienced b_{local} is relatively poor. Hence, under such circumstances, T_2 tends to dramatically shorten. This may be expressed in the following relationship:

$$R_{2_{obs}} = P_a R_{a2} + P_b R_{b2} \qquad (2.2.42)$$

where R_2 is equal to T_2^{-1}.

Since water present within living tissues is, in nature and in terms of its associated NMR parameters, an essentially dilute solution of water and the appropriate cellular salts, it may prove beneficial to consider the behaviour of protons existent within such an environment and the reasons behind this behaviour. In dilute solutions the majority of the water present acts as a pure liquid, while the remainder associates with the solute. The degree of this association is dependent upon the solute's concentration. Most solute molecules will possess a hydration "sheath", a layer of water perhaps several molecules thick and which is loosely bound to the solute's surface. This sheath is principally held in position both by electrostatic forces, consequent to the high dipole moment of the water molecule,

and by hydrogen binding consequent to the numerous proton donor and acceptor sites. The water molecules present within the hydration sheath may actually exist in a highly packed arrangement, whose freedom of motion is constrained by the attraction to the solute molecule's surface. However, such water molecules cannot be regarded as existing in a rigid lattice structure. The solute molecule may be thought of as possessing virtually no water within its internal construction. In addition to attracting water molecules to its surface, it may also subject such molecules to a variety of different environments created by the constituents of its numerous branches or side-chains. For example, if the solute is a protein molecule, then differing environments could certainly be created by the component amino-acids. Ionic regions and polar groups would prove attractive to water molecules. If τ_c is a measure of the time between periods of molecular motion then, with the presence of such polar groups, τ_c would increase for the involved protons, and hence local relaxation times would shorten. Alternatively, hydrophobic regions would prove much less attractive, thus decreasing τ_c and lengthening the associated relaxation times.

Both the exact nature and concentration of a solution influence that solution's proton relaxation times. An in-vitro protein solution will represent a fairly viscous gel for 0-3 gm. H_2O/gm. protein, and the corresponding relationship between water content and T_1 is approximately

linear. However, if there exists >3 gm. H_2O/gm. protein, the solute proves to be completely dissolved, and the nature of the relationship between water content and T_1 changes.

Interactions between different water protons in a dilute protein solution can be described as possessing four possible, and related, components(see Fig. 2.2.15):

a)water protons exchanging with protein protons
b)water protons tightly bound to the protein surface
c)water protons loosely bound to the protein molecule
d)water protons existing in the bulk liquid water

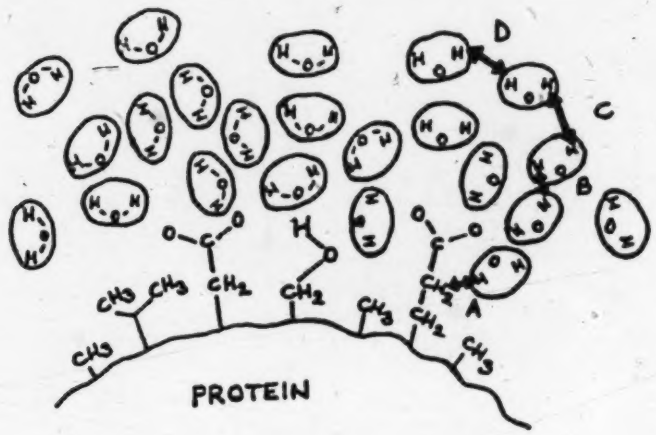

FIGURE 2.2.15: A highly diagrammatic representation of the various arrangements of water protons (A, B, C, and D) close to the surface of a large protein molecule.

Exchanges of spin and spin energy can occur in and between all these components, so it is perhaps understandable that there still lacks a model to adequately explain relaxation processes for even this simplest of examples for biomedical systems. There is considerable controversy over the degree of influence of macromolecules on the co-existent water protons. Some researchers believe that there is indeed sufficient influence to suggest that all water residing within living cells is structured(45), while others maintain that macromolecules only elicit such effects over a distance of one to two water molecule diameters. There is evidence for the former argument. This includes the observation that cells appear capable of mediating against concentration effects brought about by partial dehydration, thus preventing significant alteration in cellular reaction rates. Structuring of a substantial proportion of the cellular water could produce this behaviour. Thus, in summary, the complexity of living systems tends to suggest that some degree of water structuring must exist within living, functional cells.

2.2.8 SPIN ECHOES:

It has been related previously(see section 2.2.6) that the characteristic relaxation time describing the decay of M_{xy}, in the presence of B_0 field inhomogeneities is

represented by T_2^*. This may be related to the decay of M_{xy} elicited by irreversible molecular processes, within the investigated sample, as follows:

$$T_2^{-1*} = T_2^{-1} + \gamma(\Delta B_0 \pm \Delta B_1) \qquad (2.2.43)$$

It follows that if ΔB_0 was to be continually minimized, T_2^* would increase until it eventually equaled T_2. If B_0 inhomogeneities were to predominate, little valuable information concerning sample-related transverse relaxation would be provided by the FID. Experiments designed to minimize the deleterious effects of ΔB_0 were initially developed by Hahn(26) and have become known as spin-echo techniques. They are founded on the assumption that ΔB_0 is essentially constant in both time and space.

Following the application of a 90° RF pulse along the X-axis of the laboratory frame, the effected nuclear spins will be tipped into the XY plane. If ΔB_0 is substantial in magnitude, these spins will rapidly dephase within the XY plane, resulting in a rapid loss of both M_{xy} and the consequent emf induced in the receiver coil. However, if at a time τ later a 180° RF pulse is applied about the X-axis, each one of these spin isochromats will be rotated 180° along the X-axis. Any magnetization along the Z direction will be simply inverted to the -Z direction and thus be of no consequence. Within the XY plane, those spins precessing ahead of the average by a certain amount will, after the

180° RF pulse, lag behind the average by this same amount. Those spins initially precessing slower than the average by a certain amount will, following the refocussing(180°) RF pulse, be ahead of the average by the same amount. Thus, these spin isochromats will, at a time 2τ, rephase along the -Y axis to form a net magnetization called a spin "echo", and consequently will give rise to a regrowth of the induced emf(see Fig. 2.2.16).

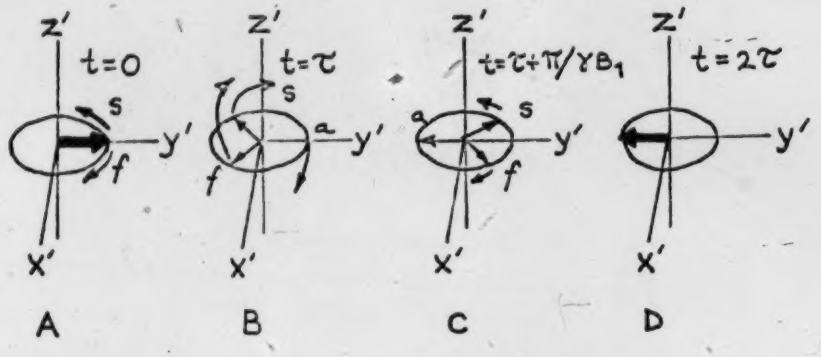

FIGURE 2.2.16: The Hahn spin-echo pulse excitation sequence:

A) dephasing of the transverse magnetization components following the 90° RF pulse
B) the application of a 180° RF pulse at $t = \tau$, and the resultant phase inversion
C) the rephasing of the transverse components at $t = \tau + \pi/\gamma B_1$
D) the generation of the spin-echo at $t = 2\tau$

[a = average transverse magnetization components, f = faster than average magnetization components, and s = slower than average transverse magnetization components]

The echo occurs at 2τ since the time required for rephasing the involved spin isochromats equals that needed to dephase them to the extent possessed immediately prior to the 180° RF pulse. If no sample-related transverse relaxation occurs

during the time interval 2τ then the spin echo will possess the identical amplitude as the initial M_{xy} signal. However, if dephasing of the spin isochromats does indeed occur as a result of transverse relaxation processes, this effect on M_{xy} cannot be removed nor minimized by the refocussing properties of the 180° RF pulse due to the random nature of these sample-related processes. Therefore the observed spin-echo amplitude will diminish by $e^{-2\tau/T_2}$.

It is a simple extrapolation of the above that enables one to discriminate against short values of T_2. By lengthening the time interval τ, a lesser number of spins contained within a short T_2 sample will refocuss following the 180° RF pulse, as their dephasing has now largely been due to irreversible processes and not those created by B_0 inhomogeneities. Consequently, only the spins of sample areas possessing relatively longer values of T_2 will undergo refocussing, and thus it will be these which eventually rephase to generate a spin echo.

It is possible to apply the 180° refocussing pulse along the Y-axis of the laboratory frame and to hence rephase the spins along this axis, such that the achieved spin echo will possess the same sign(±) as the original FID.

The above techniques prove important in the employment of spin-echo images to determine T_2. Attaching additional 180° RF pulses to the simple 90°-τ-180° sequence results in a spin-echo train, which was devised by Carr and Purcell (7)(see Fig. 2.2.17). The obtained spin-echo amplitude will

decay proportional to $e^{-2\tau/T_2}$. In practice, Carr-Purcell(CP) echo trains result in underestimation of the T_2 actually present within an investigated sample. This is due to B_1 inhomogeneities and the consequent imperfections in the 180° RF pulses. One method of compensating for these effects is

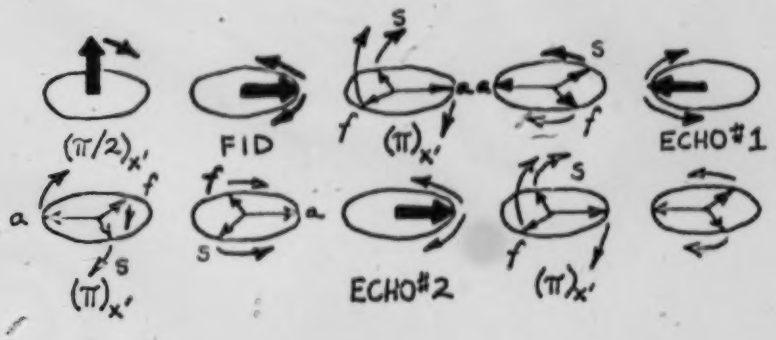

FIGURE 2.2.17: The Carr-Purcell spin-echo RF pulse excitation sequence. Note that because both the 90° and the 180° RF pulses are applied along the X'-axis, the orientation of the individual spin echoes will alternate between the -y' and the +y' axes.

to alternate the phase of the individual 180° RF pulses by 180°(see Fig. 2.2.18).

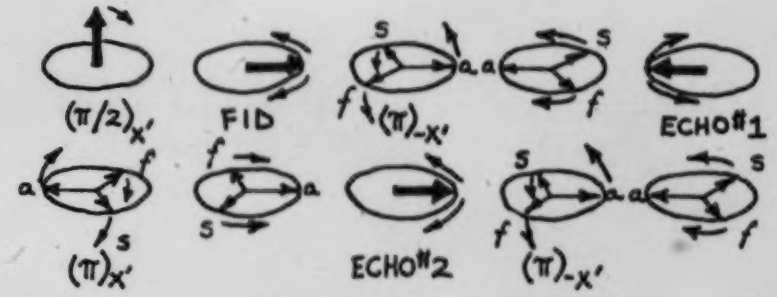

FIGURE 2.2.18: The Carr-Purcell spin-echo RF pulse excitation sequence with 180° phase alternation for each of the individual 180° RF refocussing pulses.

This creates the sequence:

$$90°(+x) - \tau - [180°(+x) - \tau - 180°(-x)]^n$$

where n is the number of repetitions for the 180° phase-shift cycle incorporated for the refocussing RF pulse. Errors in pulse length are thus cancelled on alternate spin echoes. A slightly simpler and more common modification to the CP pulse sequence is that of Meiboom and Gill(49). In this instance, all the employed 180° RF pulses are phase-shifted 90° with respect to the initial 90° RF pulse, resulting in the familiar CPMG sequence:

$$90°(+x) - \tau - [180°(+y) - \tau - 180°(-y)]^n$$

In so doing, all obtained spin-echoes will now form along the axis of B_1 for the 180° RF pulses, regardless of tip angle imperfections in the refocussing pulses(see Fig. 2.2.19).

B_1 inhomogeneities produce errors in the measurement of T_2 when such measurements are acquired with a spin-echo train, or multiple spin-echo, techniques . Unfortuantely, the more significant of these cannot be removed through use of the above pulse sequences.

Elaboration concerning the multiple spin-echo pulse sequences employed for the imaging and relaxometryinvestigations described in this thesis, is

provided in sections 4.2 and 5.2.

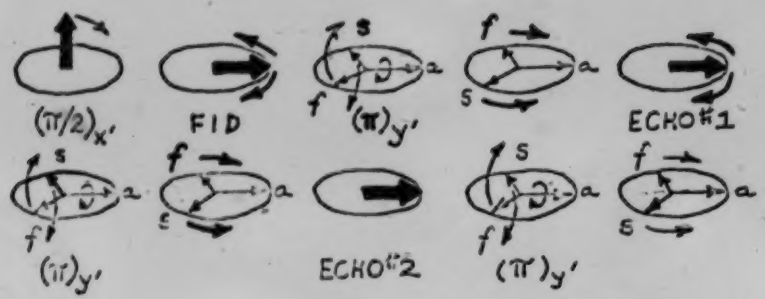

FIGURE 2.2.19: The Carr-Purcell-Meiboom-Gill spin-echo RF pulse excitation sequence. Note that because the individual 180° RF refocussing pulses are phase shifted by 90° with respect to the initial 90° RF pulse, all spin echoes form along the +y' axis.

2.2.9 2DFT IMAGE RECONSTRUCTION:

The fundamental objective in NMR imaging is to spatially encode the individual nuclear signals. This is accomplished through use of well-defined magnetic field gradients which describe a spatial variation in the amplitude, but not the direction, of an applied magnetic field. The most common of these employed in NMR imaging may be described by a linear function. One example has the gradient centered at the origin of the laboratory frame's co-ordinate system. Increasing magnitude of the gradient field is then added to, or subtracted from, the main externally-applied field B_0, as one travels farther out

along the gradient axis. These gradients establish different spatial locations possessing different amplitudes of the applied magnetic field, and therefore ensure that the resonance frequency of the involved nuclear spins varies in a controlled manner from one spatial location to another. Although it is possible to perform NMR imaging in three dimensions, it is much more common to first define a plane, or "slice", of known thickness through the sample(see section 2.2.10) and then to encode for spatial identification within this two-dimensional slice. When such a technique is employed, the gradients also play a crucial role in the initial definition of the imaging slice desired.

The imposition of a linear gradient G_r onto a static magnetic field B_0 divides the sample into elemental slices perpendicular to the gradient direction r, with each slice at a distance r from the origin possessing its own resonance condition defined by:

$$\omega_r = \gamma(B_0 \pm G_r \cdot r) \qquad (2.2.44)$$

Following the termination of an RF pulse, any magnetization component normal to the Z-axis of the laboratory frame will precess around this axis at ω_r and thus induce an emf, in an appropriately located receiver coil, at this same frequency. In selecting from the overall emf components at discrete frequency intervals, and then analysing their respective amplitudes, one obtains a measure of the resonating nuclei

at each value of r. Determination of the individual frequency components, and their respective amplitudes, is achieved through Fourier transformation of the time-domain emf waveform(see section 2.2.4). The resultant frequency-domain envelope is therefore a calibrated measure of the nuclear density existing along the gradient direction(see Fig. 2.2.20). Although the magnitude of M_{xy} has been demonstrated in this discussion to be influenced by a number of different parameters, for our purposes we will assume that only nuclear spin density is the affecting factor.

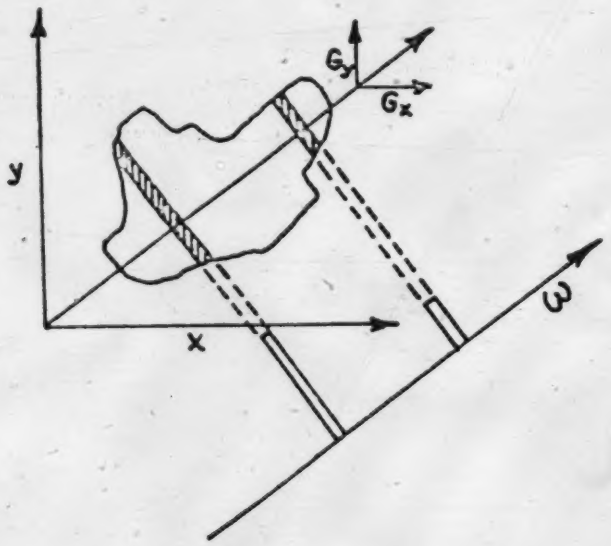

FIGURE 2.2.20: The measurement of nuclear density at different locations, and hence angular frequencies, along the direction of a linear magnetic-field gradient.

Spatial encoding via two-dimensional Fourier transformation (2DFT) is a technique which owes its inception to the work of Kumar, Welti, and Ernst(37). Two

orthogonally-positioned linear gradients are employed in a sequential fashion(see Fig. 2.2.21). The purpose of the former, G_{phase}, is to encode the associated cartesian co-ordinate into the NMR signal by determining the phase of M_{xy} at the start of the latter gradient interval. This phase angle, ϕ, is dependent on both the magnitude and the time duration of G_{phase}. The purpose of the latter gradient, G_{read}, is to encode the associated cartesian co-ordinate

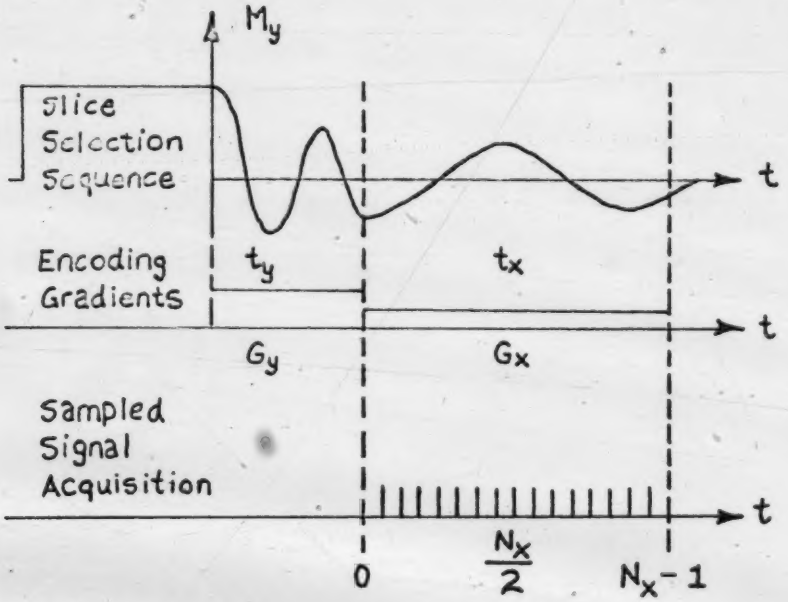

FIGURE 2.2.21: A theoretically possible sequence of magnetic-field gradient pulses used in two dimensional Fourier transform (2DFT) imaging. Data acquisition occurs from t = 0 until t = N_x - 1 .

into the NMR signal by dictating the magnetization rotation frequencies of the rotating frame and therefore determine the oscillation frequency of the emf acquired during data

sampling. In order to generate the complete NMR data set, sequences of FIDs are sampled, each corresponding to a different G_y. To bring about these sequential variations in ϕ at a specific r value, one may "step" either the magnitude of G_{phase} or the time interval over which it is active, between the individual FIDs.

Consider two elemental samples positioned asymmetrically within the XY plane at locations i and ii(see Fig. 2.2.22). We will assume that imaging slice definition has occurred previously, thus enabling us to concentrate on the evolution of the magnetization. As the magnetization develops under the influence of G_{phase}, the sample at i will contribute a component precessing about the Z-axis at an angular frequency:

$$\omega_i = \gamma G_{phase} \cdot Y_i \qquad (2.2.45)$$

where Y_i represents the position of sample i along the axis of the phase-encoding gradient, assumed here to be the Y axis of the laboratory frame. If this magnetization component has $\phi_i(0) = 0$ at $t = 0$, then at $t = t_y$:

$$\phi_i(t_y) = \gamma G_{phase} \cdot Y_i \cdot t_y \qquad (2.2.46)$$

The period of influence governed by G_{read} will start with:

$$m_{x_i} = m_{0_i} \sin \phi_i \qquad (2.2.47a)$$

$$m_{y_i} = m_{0_i} \cos \phi_i \qquad (2.2.47b)$$

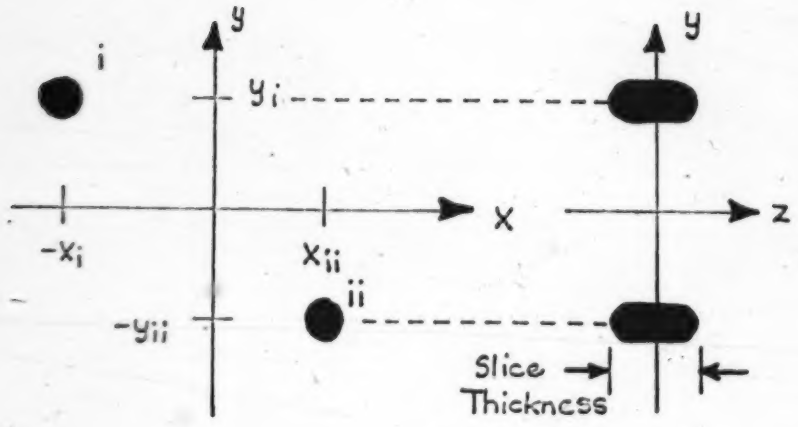

FIGURE 2.2.22: A representation of two elemental magnetizations, i and ii, positioned at $-X_i Y_i$ and $X_{ii}-Y_{ii}$ respectively.

in the laboratory frame. G_{read} will impose a different precessional frequency on the magnetization acquired from the sample at position i, described by:

$$\omega_i = \gamma G_{read} \cdot x_i \qquad (2.2.48)$$

where x_i represents the position of the sample i along the axis of the read gradient, assumed in this instance as the X-axis of the laboratory frame. The components of the magnetization within the rotating frame then become:

$$m_{x_i} = m_{0_i} \text{Sin } \phi_i + \gamma G_{read} \cdot x_i \cdot (t-t_y) \qquad (2.2.49a)$$

$$m_{y_i} = m_{0_i} \text{Cos } \phi_i + \gamma G_{read} \cdot x_i \cdot (t-t_y) \qquad (2.2.49b)$$

Similar expressions for a sample's magnetization components of the rotating frame, positioned at ii, may be obtained by exchanging frequencies $\gamma G_{phase} \cdot Y_i$ and $\gamma G_{read} \cdot X_i$ for $\gamma G_{phase}\ Y_{ii}$ and $\gamma G_{read}\ X_{ii}$ respectively in the above equations.

During the NMR experiment, QPSD of the acquired nuclear signal at the central resonance frequency, $\omega_0=\gamma B_0$, will produce two FID waveforms, corresponding to component sums of the i and ii magnetization, as described by the above equations. Complex Fourier transformation of these two FID waveforms, with respect to $(t-t_y)$, will produce frequency-domain components at both f_i and f_{ii}(see Fig. 2.2.23). The individual components, within the rotating frame, may be defined as:

$$X_{component} = m_{x_i} + m_{x_{ii}} = F_R \qquad (2.2.50a)$$

$$Y_{component} = m_{y_i} + m_{y_{ii}} = F_I \qquad (2.2.50b)$$

and the total signal may be defined as:

$$F = F_R + iF_I \qquad (2.2.51)$$

where the relative magnitudes of F_R and F_I will be governed by ϕ_i and ϕ_{ii} at time $(t-t_y) = 0$. A second Fourier

transformation, this time with respect to t_y, will give rise to a second frequency map of nuclear spin density(see Fig. 2.2.24). In converting the Fourier amplitudes into image-pixel intensities, this above map becomes a two-dimensional NMR image.

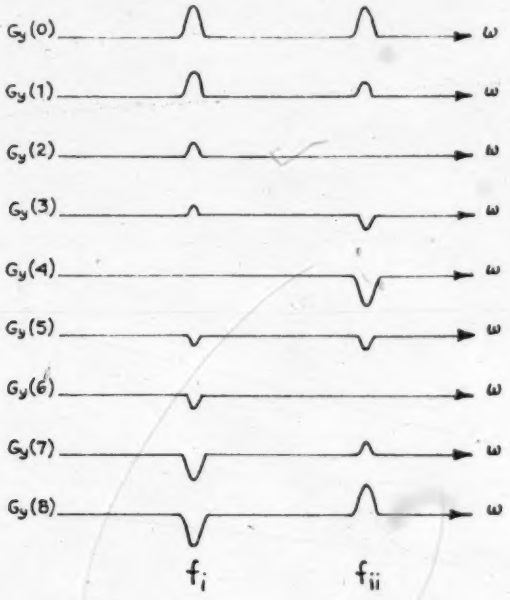

FIGURE 2.2.23: The frequency-domain components, both at f_i and f_{ii}, after a complex Fourier transformation of two different FID waveforms, with respect to $t-t_y$.

This technique of two-dimensional Fourier transform image reconstruction(2DFT) is considerably less artifact prone than are projection reconstruction techniques, but nevertheless cannot be successfully used where short acquisition intervals(<50 msec) are demanded. Under such circumstances, projection reconstruction may provide

improved results. NMR images may be generated from the 2DFT raw data matrix that represents the modulus of the spectral components($[m_{x_i}^2 + m_{y_i}^2]^{1/2}$), the real or imaginary components(m_{x_i} or m_{y_i}), and the phase of the components ($\phi = \arctan[m_{y_i}/m_{x_i}]$). This is achieved through conversion of the desired components or calculated quantites into image-pixel intensities.

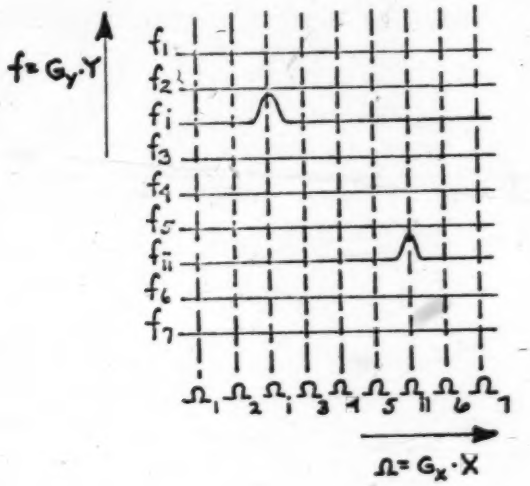

FIGURE 2.2.24: A two dimensional data array following a second complex Fourier transformation of the same two FID waveforms, as described in FIGURE 2.2.24, with respect to t_y .

2.2.10 SLICE DEFINITION AND SELECTIVE RF EXCITATION:

The incorporation of 2DFT into NMR data acquisition procedures involves the definition of an imaging slice such that all nuclei within this region are selectively excited

without the perturbation of neighbouring nuclei on either side of the slice. One can achieve this by encoding either a unique or limited bandwidth of resonance frequencies into the slice region with a linear magnetic field gradient. Then, by incorporating this bandwidth into that of the applied RF excitation pulse, one can selectively excite nuclei within this slice. Although a guide to the shape of the selectively-excited region may be obtained by considering the Fourier transform, or frequency-domain spectrum, of the employed RF waveform, a better appreciation of the process is obtained by examining how the individual magnetization components in the sample are affected by the RF pulse.

During RF excitation, the individual magnetization components will precess in the rotating frame around B_{eff}, which is comprised of the time-varying $\underline{B}_1$ field and a static component in the direction of $\underline{B}_0$, or $\underline{b}(r)$, where $\underline{b}(r)=G_r \cdot r$. $\underline{k}B_{eff}$ may, in the presence of a magnetic field gradient, be described by a slightly modified form of equation 2.2.18:

$$B_{eff} = \underline{k}(B_0 + G_r \; r - \omega/\gamma) + \underline{i}B_1 \qquad (2.2.52)$$

When the applied RF excitation is in the form of an intense square pulse, i.e. $B_1 >> b(r)$ for all r, then $B_{eff}(r) = B_1$ for all r. Consequently, all components m(r) of the total magnetization M will rotate in the Z'-Y' plane of the rotating frame and, on termination of a 90° RF pulse, will

all lie parallel to the -Y axis. Thus one observes:

$$m_y(r) = -m_0(r)$$
$$m_x(r) = 0$$
$$m_z(r) = 0$$

and $\phi(r)$ of the resultant XY magnetization, $m_{xy}(r)$, relative to the Y-axis, is zero. The net result is that all nuclei in the sample are equally excited and thus precess at an angular frequency described by equation 2.2.44.

If the intensity of the applied RF excitation is reduced, i.e. $0<B_1<<b(r)_{max}$, then B_{eff} is no longer the same for all values of r. The magnetization of those nuclei in the linear gradient near r=0 will still behave in the same manner, i.e. as they did for the position where $B_{eff}(r)=B_1$, and they will continue to be rotated into the XY plane. However, at the extremes of r, where $b(r)>>B_1$, B_{eff} will exist along the Z-axis and nuclei in these regions will experience little movement in the magnetization away from the Z-axis. Hence, at the termination of the RF pulse, one observes:

$$m_x(r) \sim 0$$
$$m_y(r) \sim 0$$
$$m_z(r) \sim m_0(r)$$

where the determining factor for the actual magnitude of

these components is the amplitude of offset b(r) relative to B_1(see Fig. 2.2.25). This phenomenon is termed an "off resonance" effect. From the above, it appears that a weak B_1 is a pre-requisite for selective excitation of a narrow slice involving nuclei around r = 0.

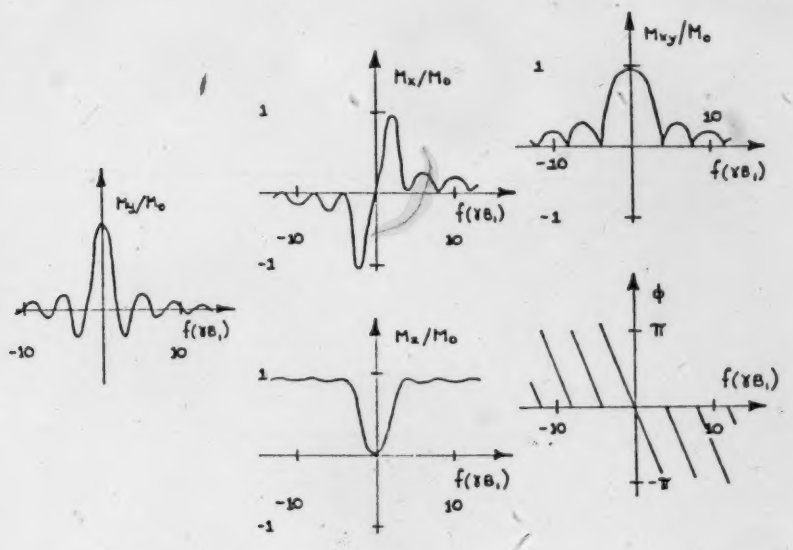

FIGURE 2.2.25: The various elemental magnetization components and phase distribution following the application of a wide bandwidth-rectangular 90° RF pulse.

It is an additional requirement of selective excitation that the boundaries of the involved region are as sharp as possible, and that the relative phase of adjacent magnetization components do not prevent observation of the NMR signal. In the boundary region where B_1~b(r) and B_{eff} is parallel neither to the X nor the Z-axis, all magnetization

components will, in general, be finite at the completion of an intense square RF pulse. The initial phase of $m_{xy}(r)$ is distributed over 2π and thus the resultant signal will be small in magnitude. The variation with offset frequency of both $m_y(r)$ and $m_x(r)$ bears a very close resemblance to the real and imaginary portions of the Fourier transform, or frequency spectrum, of the excitatory RF pulse. One might therefore conclude that, in exciting nuclei with a time-domain waveform whose frequency spectrum has a sharp cut-off, the excited slice of nuclei will exhibit similar attributes. One such time-domain envelope is a sinc function(sin x/x) where, for the purposes of suppressing the "wings" of this function(which is theoretically infinite in time), it is multiplied by a Gaussian envelope. The acquired frequency-domain spectrum will be the convolution of a rectangle with the narrower Gaussian function(see Fig. 2.2.26). Despite the ensuing frequency spectrum possessing slightly sloping boundaries, excitation with such a modulated RF waveform will produce a well-defined slice, the edges of which will exhibit a finite width.

Having so shaped the excitatory RF waveform, it is additionally necessary to overcome the phase distribution which exists, at the end of the applied RF pulse, for the magnetization components within the XY plane. Fortunately, this phase angle is a fairly linear function of the frequency offset. A reversal of the gradient after the

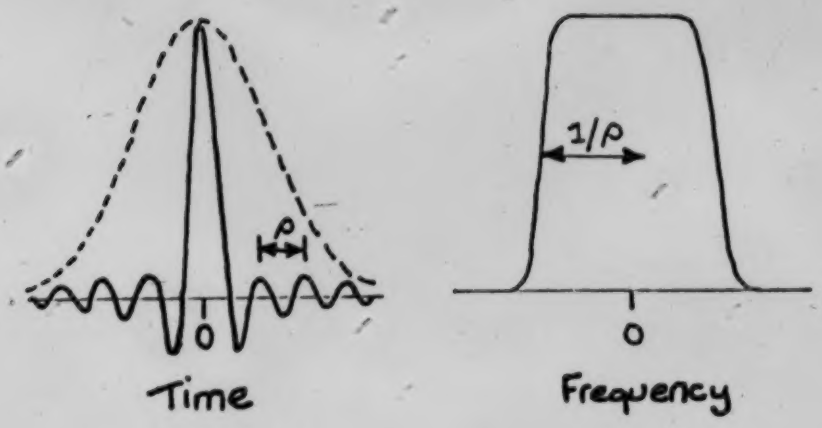

FIGURE 2.2.26: A representation of the tailored excitation function of a sinc RF pulse (left), together with its associated frequency-domain envelope (right).

termination of the RF pulse will consequently induce the individual magnetization components to rephase(see Fig. 2.2.27). A refocussed signal will then occur at some time

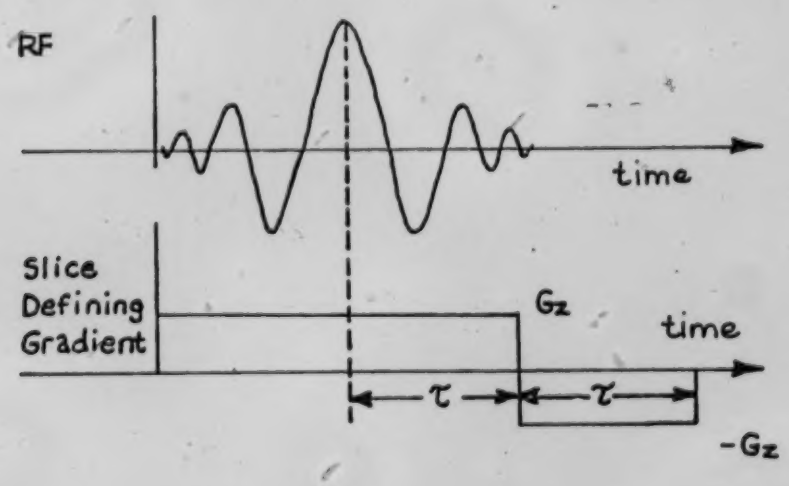

FIGURE 2.2.27: An NMR slice-defining pulsed magnetic-field gradient sequence together with an appropriately tailored RF pulse.

later, depending on the gradient strength and the intensity of the RF pulse. This refocussed signal derives solely from the selectively-excited slice. It is therefore possible to observe the nuclear spins in that slice by incorporating alternating magnetic-field gradients and selective RF excitation, the latter in the form of weak, carefully modulated RF waveforms. However, due to the interaction of B_{eff} with the off-resonance nuclear spins, pulse angles greater than 90° result in non-uniform distributions of spin excitation, both within and away from the desired slice. This must be corrected for, if quantitative NMR parameters are sought while employing totally-selective excitation techniques.

2.3.1 THE APPLICATION OF NMR IMAGING TO CLINICAL MEDICINE: A BRIEF HISTORICAL PERSPECTIVE

In 1946, both Felix Bloch and E.M. Purcell independently published(5,58) the first description of NMR and magnetization relaxation, as observed in ordinary matter. The impact of their work was both immediate and pronounced. The phenomenon of NMR has since been detected in nearly all the magnetic nuclei contained within the periodic table and in all forms of matter(1). In addition, later experimental work has led to the discovery of the fine, detailed structure of the NMR phenomenon, which arises from both chemical shifts and spin-spin couplings. This discovery established NMR as an invaluable analytical tool, such that a chemical, or biochemical, laboratory is no longer considered properly equipped without a high resolution NMR spectrometer. Consequently, whereas the initial applications of NMR were primarily restricted to physics and physical chemistry, today they have extended to a wide variety ~~of~~ disciplines, ranging from archeology to medicine.

One of the first biomedical applications of NMR to attract international attention occurred in 1971 at the State University of New York in Brooklyn, where Raymond Damadian was investigating the magnetization relaxation behaviour of water in bacterial cells as a function of the intracellular concentration of Na^+ and K^+(12). It had been

previously demonstrated that the intracellular concentration of alkali ions may be altered in cancerous tissues. Damadian extended these earlier studies in the hope of demonstrating cancer-induced alterations in the magnetization relaxation processes. It was later found that the magnetization relaxation times of certain tumors in rats were indeed lengthened in relation to those of normal tissues(13) although this finding was certainly not universally supported. Nevertheless, the ability to discriminate between cancerous and normal tissues on the basis of relaxation times proved so promising that Damadian further extended this work to humans. Unfortunately, these later studies revealed that the above discrimination was certainly not the consistent, clear-cut phenomenon that it was originally thought to represent. Nevertheless, the early pioneering results of Damadian attracted international attention towards future bio-medical applications of NMR.

In 1973, at the State University of New York in Stony Brook, Paul Lauterbur explored the possibility of generating spatial images derived from NMR principles(42). Initially described as zeugmatography(from Greek, meaning "that which joins together"), this proposed imaging modality involved computer reconstruction from projections. The first such image, generated from four projections, depicted two water-filled capillary tubes. Although the image proved to possess rather poor spatial resolution, it represented the beginning for all NMR imaging techniques in use today.

One of the early images of a biological specimen (a mouse) was acquired in 1979 at the University of Aberdeen, Scotland (46). Twenty-five projections obtained over a one hour scanning time were employed to generate longitudinal, or spin-lattice, relaxation data which were then ranked on a 10-point colour-coded scale. In 1977, Damadian achieved success with an imaging methodology entitled field focussing NMR, or FONAR, and later published images of a live rat with an implanted tumor(14) and of a normal human chest(15). At this time, the FONAR technique sampled the desired tissue region one point at a time, an extremely time-consuming procedure. However, researchers at the University of Nottingham, England were meanwhile employing a line scan method in which all points along a projected line were sampled simultaneously. Planar images were then compiled by progressing through the sample in one line increments. This proved to be considerably more time efficient than FONAR's point-scan technique. Initial images generated by the University of Nottingham's line scan method were published in 1978(47). Another University of Nottingham research group developed a variant form of this line scan method, employing alternating perpendicular magnetic-field gradients to select a line within the specimen. Not only did this simplify the imaging procedure, but as well, solved many of the resolution problems inherent in the earlier line scan imaging methods. Preliminary images of the wrist and forearm(30), generated by this later method, were

subsequently followed in 1980 by images of the human brain(31).

Since hydrogen is the most abundant element in tissues, and possesses an appropriate nuclear spin quantum number, the proton(H_1) represents the preferential nucleus for NMR imaging, both in the above described preliminary achievements and today's diagnostic usage. Although some initial steps have been taken in developing imaging methods based on C^{13}, F^{19}, Na^{23}, and P^{31}, the relatively lower tissue concentrations of these nuclei present appreciable practical limitations, such as a lowered sensitivity to alterations in the nuclei's environment, diminished signal-to-noise ratio(S/N), and a poorer anatomical resolution.

Since in H_1 images much of the NMR signal derives from the proton in water, it is theoretically possible to gain clinically useful information regarding pathological conditions in which either the water content is altered or where the intra and/or inter-molecular binding of the proton is different from the normal situation. Thus, although pathology has traditionally been regarded in anatomical terms, analysis by NMR techniques may permit discrmination of normal and diseased tissues in chemical-physiological terms. This represents an attractive attribute for a non-invasive diagnostic imaging modality, for most physicians would agree that chemical or physiological alterations in diseased tissues precede those manifested through anatomy.

2.3.2 THE APPLICATION OF NMR IMAGING TO THE QUANTIFICATION AND DESCRIPTION OF LUNG WATER: A LITERATURE REVIEW

The facts that the application of NMR to the quantification and description of lung water is a comparatively recent development, and that there exist numerous technical difficulties associated with such an application, has greatly restricted the size of both the experimental and clinical literature. Thus, it is quite possible to present this literature in total, to discuss what has been accomplished, and to elaborate on what still need be accomplished in future investigations.

The researchers who initially proposed employing NMR techniques to detect and quantify lung water were Lauterbur (43) and his graduate student, J.A. Frank(23) in 1977. They examined the relationship between the in-vivo longitudinal relaxation of excised lung tissue and the water content of the lung tissue, as calculated from a wet to dry ratio(W/D). The resulting linear relationship was sufficiently reproducible that Lauterbur and Frank concluded that it may be feasible to employ such an application of NMR within a clinical setting. However, it was to be several years before other investigators were to follow on this suggestion.

In 1982, Hayes et al.(28) used a line scan imaging methodology(three perpendicular magnetic-field gradients within a static field of 0.94T) to detect and quantify lung

water. The quantification procedure was developed with four $CuSO_4$-doped solutions of H_2O and D_2O(H_2O/D_2O = 100, 75, 50, and 25%) which were imaged and later analysed for signal intensity. Since D_2O should not produce an NMR signal at the H_2O resonance frequency, it was reasoned that these images would establish a relationship between H_2O content and NMR signal intensity. Signal intensity values for all images were normalized to that of the 100% H_2O solution. Imaging was then performed on either the lungs of intact dead animals or on isolated lungs, in both of which saline had been previously instilled via the central airway. By selecting such imaging specimens, the need for incorporating respiratory-gated data acquisition procedures was avoided. Image signal intensity was then compared to the wet lungs' H_2O content, calculated from W/D values normalized for the dry lung weight. Results obtained with the normalized signal intensities of the H_2O/D_2O phantoms correlated well with the actual phantom H_2O content and provided confidence for the in-vitro lung measurements. In addition, when lung sample weight was extrapolated to correspond to zero NMR signal intensity, the predicted sample weight represented 98% of the actual in-vitro dry lung sample weight.

Despite the acquisition of encouraging preliminary results, these studies are unfortuantely inconclusive. Proton density alone is unable to differentiate between areas of increased signal intensity as caused by atelectasis, infection, tumor, passive congestion, and

pulmonary edema. The acquisition of longitudinal or transverse relaxation information will aid in disclosing the actual cause for the increased signal intensity. Moreover, the calculation of lung water content by simple W/D values will include the blood fluid component, and will thus tend to overestimate the extravascular lung water(EVLW) content. Plasma or erythrocyte markers would enable a correction for the inclusion of blood water.

Skalina and co-workers(64) performed a more detailed investigation concerning the effect of increased permeability pulmonary edema on proton NMR relaxation times. Edema was produced by an intravenous injection(50 mg/kg and 100 mg/kg) of alloxan, an oxidized product of uric acid, whereas control animals received only an intravenous injection of saline. Rats were mechanically ventilated with a tidal volume of 8-10 ml, delivered at 60-80 breaths/minute, and with 0-5 cm H_2O end-expiratory pressure. After sufficient time had elapsed to allow a uniform edema distribution, the animals were sacrificed and T_1 and T_2 calculated from in-vitro lung samples at 0.12T and with an inversion-recovery and CPMG pulse sequence respectively. Relaxation times were found to be linearly related with blood-free lung water measurements. As a result, these authors proposed the use of relaxation times to distinguish between different causes of increased signal intensity common to all forms of lung edema.

This investigation represents an excellent preliminary assessment of NMR's capability to detect alterations in EVLW. The authors successfully related changes in lung water content with those of relaxation times, although no mention was made concerning the number of data points used to express the individual relaxation times. In addition, hemoglobin was employed to assess blood water volume, thus resulting in more reliable determinations of EVLW.

Cutillo et al.(11) extended the earlier work of Hayes and co-workers(28), in producing T_2-weighted images of excised, unperfused rat lungs which were continually inflated with humidified air to 20 cm H_2O transpulmonary pressure. These measurements were carried out at 0.94T with a line scan imaging technique. Unfortunately, the transverse magnetization decay was estimated from only two data points and the in-vitro lung sample W/D values were not corrected for blood fluid volume. Nevertheless, significant correlation(r=0.91) was observed between these parameters.

This same investigation group was responsible for the description of a tissue-related irreversible transverse magnetization decay phenomenon(52) which produces unusually short T_2 when observed in images of either excised lungs or of the lungs within a living experimental animal. A similar NMR phenomenon was observed in a slurry of 5 μm alumina particles in H_2O, which suggested that extensive air-H_2O interfaces may act as a source of spatially-dependent magnetic field inhomogeneities. This finding led to the

development of a subtraction image methodology which incorporated both symmetric(90°-tau-180°-tau-spin echo) and asymmetric(90°-tau-180°-tau′-spin echo) pulse sequences. Variable magnetic field gradients were used to aid in the refocussing of the transverse magnetization components such that spin echoes were produced at various times(tau or tau′) after the 180° RF refocussing pulse. The subtraction images were acquired for both live and dead rats with or without oleic acid-induced pulmonary edema and were reconstructed as follows:

$$\frac{\text{NMR symmetric signal-NMR asymmetric signal}}{\text{NMR symmetric signal}}$$

These subtraction images were found to compliment conventional NMR images and provided additional information concerning regional lung inflation.

However, the authors did not address the validity of these findings, for spatially-dependent magnetic field inhomogeneities are dependent upon two factors: the static magnetic field itself and the tissue's suseptibility to that field. Neither of these is appreciably altered by lung inflation. Consequently, one must question whether or not this observation is related to the usage of a two-point fit for T_2. It would be worthwhile to examine this phenomenon in a detailed analytical fashion, perhaps with multiple spin-echoes.

In 1985, Carroll and co-workers(8) presented the first application of NMR imaging to the detection of lung water in humans. Normal human volunteers were studied both in the supine and prone position in a 0.5T whole-body imaging system. Single spin-echo images were acquired at various repetition times(T_R) with combined respiratory and cardiac-gated data acquisition. Although cardiac gating substantially reduced heart motion artefacts, enhanced signal intensity from slowly flowing blood masked the lungs' normal EVLW signal by approximately 44%. However, acquired images did reveal a gravity-dependent gradient of signal intensity within the lung(extreme spatial variations averaged 238±28%). This investigation also examined the influence of elevating the pulmonary hydrostatic pressure, in sheep, on the NMR image signal intensity. The elevated hydrostatic pressures were produced by the inflation of a left-atrial balloon, after which the anaesthetized animals were intubated and maintained with high-frequency ventilation(100 breaths/minute, P_{aw} = 75-80 cm H_2O). When employing such a mode of mechanical ventilation, chest wall excursions are minimal, thus reducing the necessity for respiratory gating. The elevated hydrostatic pressures sufficiently increased EVLW content to elevate the NMR signal intensity by approximately 600% over the normal condition. This observation was most pronounced within the gravity-dependent portions of the lung. Prior to imaging, all experimental animals underwent a multiple-indicator

dilution examination(where triated H_2O, C^{14}-urea, I^{125}-albumin, and Cr^{51}-erythrocytes are injected into the jugular vein as a bolus, and are then rapidly retrieved in sequential samples from the aorta) in order to ascertain the normal lung water content. After inflation of the left-atrial balloon and subsequent imaging, this examination was repeated. The elevation of pulmonary hydrostatic pressures increased EVLW by 30-83% in all animals.

Despite the acquisition of good quality spin-echo images, changes in EVLW were assessed in terms of image signal intensity. It has been related previously that, by itself, proton density is unable to distinguish between numerous pathophysiological conditions and as such is inconclusive.

The first successful attempt to measure the longitudinal relaxation time(T_1) of in-vivo edematous lung tissue was made by Wexler et al.(72) in 1985. Increased permeability pulmonary edema was induced in dogs with endobronchial saline lavage(15 ml/kg). The animals were mechanically ventilated (O_2/halothane), although respiratory-gated data acquisition was not employed. The authors defended this decision with the argument that a cylindrical phantom containing $MnCl_2$, moving through the imaging plane along a perpendicular axis, produced only a 3% deviation in the calculated T_1. However, the validity of such a phantom in representing the actual respiratory motion of an experimental animal was not addressed. T_1 was also

calculated with only two single spin-echo images, each acquired at a different T_R. The experimental animals were imaged at 0.15T in a whole-body imaging system, with T_1 of the edematous lung regions calculated in a fashion identical to that of the $MnCl_2$ phantom. After completion of the lung imaging, the experimental animals were sacrificed and approximately 20 tissue samples taken from each lung, with emphasis being made on the edematous regions. These were then analysed in a 0.25T spectrometer for both T_1 and T_2, which were calculated from 32-point saturation recovery and Hahn techniques respectively. Finally, in-vivo T_1 measurements from the acquired images were related to EVLW, acquired from the samples via the usual W/D measurements, without correction for blood fluid volume. The correlation coefficient was only 0.7, which may well be related to the particular analytical techniques employed.

Later in 1985, Schmidt et al. undertook a series of investigations designed essentially along more practical lines. Their initial study(62) sought to determine the capability of NMR to differentiate between increased permeability and hydrostatic pulmonary edema. Increased permeability edema was induced in rats by intravenous injection of oleic acid(0.05 -1.0 ml/kg), whereas hydrostatic edema was induced by a continuous intravenous infusion of saline delivered at a rate of 0.7-2.0 ml/minute. Imaging was then performed sixty minutes later at 0.35T with a single spin echo technique at five different imaging slice

locations within the edematous lungs. The animals were then sacrificed and the lungs removed en bloc. In-vitro spectrometric analysis of individual lung tissue samples for T_1 and T_2 was carried out at 0.25T with 32-point saturation recovery and Hahn spin-echo techniques respectively. Results were correlated with EVLW, as calculated from W/D measurements, without correction for blood fluid volume. The acquired images were analysed for signal intensity alone. Although both experimental models produced an extensive increase in lung-image signal intensity, that of hydrostatic edema was more centrally distributed throughout the lung. Spectrometric analysis of the lung tissue samples revealed a similarity of T_1 in both forms of edema, but a shorter T_2 in the hydrostatic variety. Image signal intensity pertaining to hydrostatic edema was also observed to change less for a given change in EVLW than that of increased permeability edema.

A later study by this same group(63) assessed the influence of Gadolinium-DTPA(G-DTPA) upon the relationship of image signal intensity and lung water content. G-DTPA was administered in two dosages(0.05 and 0.1 mM/kg) five minutes prior to imaging, one each to separate portions of the experimental animal(rat) population. All animals had previously received an intravenous injection of oleic acid(0.05-0.1 ml/kg) to induce increased permeability pulmonary edema. The presence of G-DTPA produced an easily observable increase in signal intensity in images of short

T_R(0.5 second) depicting pulmonary edema. However, the increase in signal intensity observed in edema images acquired with G-DTPA and with a short T_R, did not exceed that acquired in the absence of G-DTPA and with a long T_R(2.0 seconds). G-DTPA was thus revealed to distribute rapidly into pulmonary edema, permit improved sensitivity at shorter pulse sequence T_R, and significantly decrease total scan time.

The investigations discussed above constitute the experimental literature pertaining to the application of NMR techniques to the quantification and description of lung water. There exist a number of research abstracts, yet the majority of these describe the pilot studies to the aforementioned endeavours. There also exists a number of technical articles relating to the development of pulse sequences, respiratory-gated data acquisition procedures, data post-processing techniques that propose to abolish the need for respiratory gating, and mechanical high-frequency ventilators that maintain experimental animals with a minimum of chest wall excursions. However related these may be to NMR imaging of the in-vivo lung, they at most represent an associated and interesting sidelight not particularly germane to this review, and consequently will not be further discussed. For the purposes of this literature review there remains only the discussion of two investigations from Aberdeen, Scotland, that dealt principally with the imaging of human subjects.

The first of these, by Johnston and co-workers(33), assessed the ability of NMR imaging to detect pulmonary pathologies in human lungs excised at autopsy. The intact excised lungs of ten females(aged 62-77) were intubated and inflated with intermittent positive-pressure ventilation which maintained the lungs at full inflation throughout the imaging procedure. The lungs were positioned within a Perspex model of the thorax, in order to support them in their natural configuration, and then imaged at 0.08T with the spin-warp pulse sequence. The acquired images, made approximately 32 hours after death, and the resultant quantitative data(proton density and T_1) were compared with both the specimens' macroscopic and microscopic appearances. Although edematous lung tissue appeared more dense than normal lung tissue in all proton density images, there was no differentiation possible between inflammatory edema and that resulting from cardiac failure. Pulmonary infarcts similarily presented elevated signal intensities and were frequently surrounded by a relatively less dense zone of edema. Most surprising however, was the observation that differences in T_1 between normal, edematous, and infarcted lung tissue did not reach significance. This may be due, at least partially, to the prolonged elapsed time(32 hours) between death and imaging of the lung tissue. It has been previously demonstrated(69) that such an interval would, in itself, produce deviations of the longitudinal relaxation from that observed in-vivo in the same tissue.

The second of these Aberdeen investigations was undertaken by MacLennan et al.(44), who employed the same 0.08T imaging system and spin-warp pulse sequence(generating solely proton density images) to measure the total EVLW of normal human volunteers. Six individuals(average age=32) were imaged in the supine position, commencing with the lung apices and progressing in 2 cm increments to the level of the diaphragm. A bottle of $CuSO_4$-doped H_2O was positioned in each of the sequential imaging planes, to act as a standard. The desired lung-fields were outlined in all acquired images as the region of interest(ROI), with EVLW for each imaging slice calculated from relationships between the proton density of the standard and the ROI. Total EVLW was then ascertained by this calculation procedure summated over all imaging slices.

This quantitative technique, when later verified in a study involving experimental animals, produced a 30% underestimation of the actual EVLW, as determined from W/D measurements. The authors proposed that the extensive air-H_2O interface phenomenon described by Morris et al.(52), may have artefactually produced shorter longitudinal relaxation, and thus created artefactually low values of proton density within the in-vivo lung. However, one will remember that this interface phenomenon pertained to an effect on the transverse relaxation only. In addition, these authors related changes in lung water to only one NMR parameter, proton density, and assessed actual EVLW from W/D

measurements without correction for blood fluid volume.

It is intended that by way of this literature review, the reader will appreciate the current status of the application of NMR techniques to the detection, quantification, and description of EVLW. Although some excellent preliminary work has been accomplished, much work remains to be done involving fundamental concerns:

1) improved image quality, since both paucity of signal and continual respiratory motion throughout the NMR scan degrade the S/N from the in-vivo lung

2) more accurate measurements of in-vivo tissue relaxation times

3) correction of post-mortem determinations of EVLW for blood fluid volume, since the blood fluid component of the lung is not always discernable within NMR images

BIBLIOGRAPHY:

1) Abragam, A. The Priciples of Nuclear Magnetism. Oxford, England: Oxford University Press, 1961.

2) Foster, M.A.. Magnetic Resonance in Medicine and Biology. Oxford, England: Pergamon Press, 1984.

3) Fukushima, E. and S.B.W. Roeder. Experimental Pulse NMR: A Nuts and Bolts Approach. Reading, Massachusetts: Addison-Wesley Publishing Co., Ltd., 1981.

4) Gadian, D.G.. Nuclear Magnetic Resonance and its Applications to Living Systems. Oxford, England: Oxford University Press, 1982.

5) Mansfield, P. and P.G. Morris. NMR Imaging in Biomedicine, Supplement II of Advances in Magneitc Resonance, J.S. Waugh, editor. New York, New York: Academic Press, 1982.

6) Staub, N.C.. Lung water and Solute Exchange, Volume 7 of Lung Biology in Health and Disease. New York, New York: Marcel Dekker, Inc., 1978.

6) West, J.B.. Respiratory Physiology: The Essentials. Baltimore, Maryland: Williams and Wilkins Co., 1974

REFERENCES:

1) Andrew, E.R.. Foreword, in Nuclear Magnetic Resonance and Correlative Imaging Modalities, edited by C.L. Partain and J.A. Sorenson. New York, New York: Society of Nuclear Medicine, Inc., 1984.

2) Ashbaugh, D.G. and T. Uzawa. Respiratory and hemodynamic changes after injection of free fatty acids. J. Surg. Res. 8: 417-423, 1968.

3) Baile, E.M., P.D. Pare, R.W. Dahlby, and J.C. Hogg. Regional distribution of extravascular water and hematocrit in the lung. J.Appl. Physiol. 46: 937-942, 1979.

4) Belton, P.S., K.J. Packer, and T.C. Sellwood. Pulsed nmr studies of water in striated muscle II: spin-lattice relaxation times and the dynamics of the non-freezing fraction of water. Biochem. Biophys. Acta 304: 56-64, 1973.

5) Bloch, F., W.W. Hansen, and M.E. Packard. Nuclear Induction. Phys. Rev. 70: 460-474, 1946.

6) Butcher, E.O.. The penetration of fat and fatty acids into the skin of the rat. J. Invest. Dermat. 20) 43-48, 1953.

7) Carr, H.Y. and E.M. Purcell. Effects of diffusion on free precession in nuclear magnetic resonance experiments. Phys. Rev. 94: 630-638, 1954.

8) Carroll, F.E., J.E. Loyd, K.B. Nolop, and J.C. Collins. MR imaging parameters in the study of lung water: a preliminary study. Invest. Radiol. 20: 381-387, 1985.

9) Conhaim, R.L. and N.C. Staub. Effect of inflation volume on protein leakage across the alveolar barrier in fluid-filled isolated dog lung. Physiologist 24: 16, 1981.

10) Cooke, R. and R. Wien. The state of water in muscle tissue as determined by proton nuclear magnetic resonance. Biophysical J. 11: 1002-1017, 1971.

11) Cutillo, A.G., A.H. Morris, D.D. Blatter, T.A. Case, D.C. Ailion, C.H. Durney, and S.A. Johnson. Determination of lung water content and distribution by nuclear magnetic resonance. J. Appl. Physiol. 57: 583-588, 1984.

12) Damadian, R.. Biological ion exchanger resins I: quantitative electrostatic correspondance of fixed charge and mobile counter ion. Biophys. J. 11: 739-760, 1971.

13) Damadian, R.. Tumor detection by nuclear magnetic resonance. Science 171: 1151-1153, 1971.

14) Damadian, R., L. Minkoff, M. Goldsmith, M. Stanford, and J. Koutcher. Field focussing nuclear magnetic resonance(fonar): visualization of a tumor in a live animal. Science 194: 1430-1431, 1976.

15) Damadian, R., M. Goldsmith, and L. Minkoff. NMR in cancer xvi: fonar image of the live human body. Physiol. Chem. Phys. 9: 97-100, 1977.

16) Deland, F.H.. Bone marrow embolism and associated fat embolism to the lungs. Thesis, Mayo Foundation, Graduate School of the University of Minnesota, March 1956.

17) Derks, C.M. and R.M. Peters. The role of shock and fat embolus in leakage from the pulmonary capillary. Surg. Gynecol. Obstet. 137: 945-948, 1973.

18) Derks, C.M. and D. Jacobovitz-Derks. Embolic pneumopathy induced by oleic acid. Amer. J. Pathol. 87: 143-158, 1977.

19) Drinker, C.K.. Pulmonary Edema and Inflammation. Cambridge, Massachusetts: Harvard University Press, 1945.

20) Fein, A.M., S.K. Goldberg, M.L. Lippman, R. Fischer, and L. Morgan. Adult respiratory distress syndrome. Br. J. Anaesth. 54: 723-736, 1982.

21) Flick, M.R., A. Perel, W. Kageler, and N.C. Staub. Regional extravascular lung water in normal sheep. J. Appl. Physiol. J. Appl. Physiol. 46: 932-936, 1979.

22) Fonte, D.A. and F.X. Hausberger. Pulmonary free fatty acids in experimental fat embolism. J. Trauma 11: 668-672, 1971.

23) Frank, J.A.. Thesis, State University of New York in Stony Brook, 1977.

24) Gatzy, J.T.. The mode of chloride secretion by lung epithelium. Amer. Rev. Resp. Dis. 127: S14, 1983.

25) Gee, M.H. and D.O. Williams. Effect of lung inflation on perivascular cuff fluid volume in isolated dog lung lobes. Microvasc. Res. 17: 190-201, 1979.

26) Hahn, E.L.. Spin echoes. Phys. Rev. 80: 580-594, 1950.

27) Harman, J.W. and F.J. Ragaz. The pathogenesis of experimental fat embolism. Amer. J. Pathol. 26: 551-564, 1949.

28) Hayes, C.E., T.A. Case, and D.C. Ailion. Quantitation of lung water by nuclear magnetic resonance imaging. Science 216: 1313-1315, 1982.

29) Hills, B.A.. What forces keep the air spaces dry?. Thorax 37: 713-717, 1982.

30) Hinsaw, W.S., P. Bottemley, and G.N. Holland. Radiographic thin-section image of the human wrist by nuclear magnetic resonance. Nature 270: 722-723, 1977.

31) Holland, G.N., W.S. Moore, and R.C. Hawkes. Nuclear magnetic resonance tomography of the brain. J. Comp. Assist. Tomog. 4: 1-3, 1980.

32) Hollis, D.P., J.S. Econmov, L.C. Parks, J.C. Eggleston, L.A. Saryan, and J.L. Czeister. Nuclear magnetic resonance studies of several experimental and human malignant tumors. Cancer Res. 33: 2156-2160,1973

33) Johnston, P.W., F.M. MacLennan, J.G. Simpson, and F.W. Smith. Nuclear magnetic resonance imaging of pulmonary infarction and oedema in excised cadaver lungs. Mag. Res. Imaging 3: 157-161, 1985.

34) Julien, M., M.R. Flick, J.M. Hoeffel, and J.F. Murray. Accurate reference measurement for post-mortem lung water. J. Appl. Physiol. 56: 248-253, 1984.

35) King, E.G., W.W. Wagner, D.G. Ashbaugh, L.P. Latham, and D.R. Halsey. Alterations in pulmonary microanatomy after fat embolism: in vivo observations via thoracic windows of the oleic acid embolized canine lung. Chest 59: 524-530, 1971.

36) Kuhne, H. and K.H. Kremser. Die klinische bedeutung der traumatischen fettembolie. Beitr. Klin. Chir. 195: 385-394, 1957.

37) Kumar, A., D. Welti, and R.R. Ernst. NMR fourier zeugmatography. J. Mag. Res. 18: 69-83, 1975.

38) Kuntz, I.D., T.S. Brassfield, G.D. Laws, and G.V. Purcell. Hydration of macromolecules. Science 163: 1329-1331, 1969.

39) Lachmann, B., B. Robertson, and J.Vogel. In vivo lung lavage as an experimental distress syndrome. Acta Anaesth. Scand. 24: 231-236, 1980.

40) Lachmann, B., B. Jonson, M. Lindroth, and B. Robertson. Modes of artificial ventilation in severe respiratory distress syndrome. Crit. Care Med. 10: 724-732, 1982.

41) Larsen, O.A.. The hematocrit of the lung in man. Scand. J. Clin. Lab. Invest. 18: 112-118, 1966.

42) Lauterbur, P.C.. Image formation by induced local interactions: examples employing nuclear magnetic resonance. Nature 242: 190-191, 1973.

43) Lauterbur, P.C.. Paper presented at the Engineering Foundation Conference on Comparative Productivity of Techniques for Non-Invasive Medical Diagnosis, Henniker, N.H., August 1976.

44) Ling, G.N.. The physical state of water in living cells and its physical significance. Intern. J. Neurosci. 1: 129-152, 1970.

45) MacLennan, F.M., M.A. Foster, F.W. Smith, and G.A. Crosher. Measurement of total lung wtare from nuclear magnetic resonance images. Br. J. Radiol. 59: 553-560, 1986.

46) Mallard, J., J.M.S. Hutchison, W. Edelstein, C.R. Ling, and M. Foster. Imaging by nuclear magnetic resonance and its biomedical implications. J. Biomed. Engin. 1: 153-160, 1979.

47) Mansfield, P., I.L. Pykett, P.G. Morris, and R.E. Coupland. Human whole body line scan imaging by nmr. Br. J. Radiol. 51: 921-922, 1978.

48) Mason, R.J., M.C. Williams, and J.H. Widdicombe. Fluid and electrolyte transport across the monolayers of alveolar type II cells in vitro. Amer. Rev. Resp. Dis. 127: 524, 1983.

49) Meiboom, S. and D. Gill. Modified spin echo method for measuring nuclear relaxation time. Rev. Sci. Instr. 29: 688, 1958.

50) Meyrick, B.O.. Pathology of pulmonary edema. Sem. in Resp. Med. 4: 267-273, 1983.

51) Miller, W.S.. The Lung(2nd edition). Springfield, Illinois: Charles C. Thomas & Co., 1947.

52) Morris, A.H., D.D. Blatter, T.A. Case, A.G. Cutillo, D.C. Ailion, C.H. Durney, and S.A. Johnson. A new nuclear magnetic resonance property of the lung. J. Appl. Physiol. 58: 759-762, 1984.

53) Muir, A.L., D.L. Hall, P. Despas, and J.C. Hogg. Distribution of blood flow in the lungs in acute pulmonary edema in dogs. J. Appl. Physiol. 33: 763-769, 1972.

54) Muir, A.L., J.C. Hogg, A. Naimark, and W. Chernecki. The effect of alveolar liquid on the distribution of blood flow in dog lung. J. Appl. Physiol. 39: 885-890, 1975.

55) Naimark, A., B. W. Kirk, and W. Chernecki. Regional Water Volume, Blood Volume, and Perfusion in the Lung, in Central Aerodynamics and Gas Exchange. Turin, Italy: Minerva Medica, 1971.

56) Pattle, R.E.. The surface lining of lung alveoli. Physiol. Rev. 45: 48-79, 1965.

57) Peltier, F.. Fat embolism III: the toxic properties of neutral fat and free fatty acids. Surgery 40: 665-670, 1956.

58) Peltier, F.. The diagnosis of fat embolism. Surg. Gynecol. Obstet. 121: 371-379, 1965.

59) Purcell, E.M., H.C. Torrey, and R.V. Pound. Resonance absorption by nuclear magnetic moments in a solid. Phys. Rev. 69: 37-38, 1946.

60) Rapaport, E., H. Kuida, F.W. Haynes, and L. Dexter. Pulmonary cell and plasma volumes and pulmonary hematocrit in the normal dog. Am. J. Physiol. 185: 127-132, 1956.

61) Robertson, J.D.. The function and metabolism calcium in the invertebrata. Biol. Rev. 16: 106-133, 1941.

62) Schmidt, H.C., D.G. Tsay, and C.B. Higgins. Pulmonary edema: an mr study of permeability and hydrostatic types in animals. Radiol. 158: 297-302, 1986.

63) Schmidt, H.C., M.T. McNamara, R.C. Brasch, and C.B. Higgins. Assessment of severity of experimental pulmonary edema with magnetic resonance imaging: effect of relaxation enhancement by g-dtpa. Invest. Radiol. 20: 687-692, 1985.

64) Skalina, S., H.L. Kundel, G. Wolf, and B. Marshall. The effect of pulmonary edema on proton nuclear magnetic resonance relaxation times. Invest. Radiol. 19: 7-9, 1984.

65) Sladen, A., M.B. Laver, and H. Pontoppidan. Pulmonary complications and water retention in prolonged mechanical ventilation. New Engl. J. Med. 279: 448-453, 1968.

66) Staub, N.C. and J.C. Hogg. Conference report of a workshop on the measurement of lung water. Crit. Care Med. 8: 752-759, 1980.

67) Staub, N.C.. Alveolar flooding and clearance. Amer. Rev. Resp. Dis. 127: 544-550, 1983.

68) Staub, N.C.. Pathophysiology of Pulmonary Edema, in Edema, edited by N.C. Staub and A.E. Taylor. New York, New York: Raven Press, 1984.

69) Thickmann, D.L., H.L. Kundel, and G. Wolf. Nuclear magnetic resonance characteristics of fresh and fixed tissue: effect of elapsed time. Radiol. 148: 183-185, 1983.

70) West, J.B., C.T. Dollery, and A. Naimark. Distribution of blood flow in isolated lung; relation to vascular and alveolar pressures. J. Appl. Physiol. 19: 713-724, 1964.

71) West, J.B.. Respiratory Physiology: The Essentials. Baltimore, Maryland: The Williams & Wilkins Co., 1974.

72) Wexler, H.R., R.L. Nicolson, F.S. Prato, L.S. Carey, S. Vinitski, and L. Reese. Qunatitation of lung water by nuclear magnetic resonance imaging: a preliminary study. Invest. Radiol. 20: 583-590, 1985.

73) Wynne, J.W. and J.H. Modell. Respiratory aspiration of stomach contents. Ann. of Int. Med. 87: 466-474, 1977.

PRELIMINARY IN-VIVO NMR IMAGING EXPERIMENTS

3.1 INTRODUCTION:

Recent investigations concerning the application of Nuclear Magnetic Resonance Imaging(NMRI) to pulmonary pathophysiology have revealed the remarkable sensitivity of this new imaging modality to lung water content (2,4,11,12,14). Results from these early studies suggest the future employment of NMRI both to visualize spatially and to quantify lung water. In order to attain these objectives, images free of noise and artefacts must be consistently acquired, from which reliable in-vivo calculations of proton density(ρ) and tissue relaxation times T_1 and T_2 may be made. However, in using methodologies predominant on contemporary clinical NMRI systems these two objectives may be exclusive. Thus the acquisition of high quality images does not necessarily infer valid in-vivo tissue relaxation times.

It is indicative of the magnitude of the technical difficulties associated with the acquisition of both quality images and reliable quantitative information, that the majority of pulmonary NMRI investigations detect changes in

A version of this chapter has been published.
Phillips, D.M., Lunt, J.A., Man, S.F.P., and
Allen, P.S. 1987. Mag. Res. Imaging 5:137-147.

lung water content with image-pixel intensities(2,11), two point calculations of in-vivo T_1 and T_2(14), or in-vitro T_1 and T_2 measurements(4,11,12). These experiments led to the development of a methodology for respiratory-gated data acquisition that provides high-quality multiple spin-echo(MSE) images of the lung, but which utilizes a radio-frequency(RF) pulse sequence comprising selective RF pulses and spin conditioning. Although selective RF pulses were found to produce optimal results in terms of image quality, care must be exercised when quantitative parameters are derived from such images. Selective RF inversion or refocussing pulses produce spatial distributions of both the tip angle and the phase of the transverse magnetization, which give rise to deviations of the measured relaxation indices from the relaxation times which are meaningful on an absolute scale(7,8,10). In contemporary clinical NMRI systems, the use of non-selective RF inversion or refocussing pulses is not at all common due to their substantial power requirements. In the light of this, it is unfortunate that most published reports concerning the application of NMRI to experimental pulmonary edema do not address the question of how meaningful are the measured relaxation indices which they contain.

In addition to outlining a methodology for acquiring high-quality in-vivo MSE images of the lung in both the normal and the edematous state, this chapter also explores alternative strategies using non-selective refocussing

pulses and spin conditioning and compares their reliability for providing either good quality images or accurate quantitative relaxation measurements.

3.2 EXPERIMENTAL:

This investigation was divided into two parts. The first consisted of an NMR imaging study of an animal model of pulmonary edema, using respiratory-gated RF pulse sequences, with the transverse relaxation time calculated from MSE images. The second part comprised an in depth study of a stationary phantom which compared transverse relaxation indices obtained from MSE images of the phantom, using the same RF pulse sequences as used in the animal model, with T_2 measurements obtained from an in-vitro analysis of the phantom constituents.

3.2.1 Imaging System and RF Sequences:

NMR images of both the experimental animal and the stationary phantom were acquired at 2.35T in a 40 cm bore magnet and using a Brucker CXP spectrometer(Bruker Spectrospin, Karlsruhe, West Germany). Gradient strengths of 3.5 mT m^{-1} resulted in a slice thickness of approximately 3 mm and an in-plane spatial resolution of 1.72 mm by 0.86 mm for a 128x256 raw data matrix interpolated to a 256x256

pixel image matrix. The RF field, B_1, and static field, B_0, inhomogeneities over a total imaging volume representative of an experimental animal have been measured at 10% and 7 ppm respectively. All images described are of the MSE type, generated by a selective 90° RF pulse followed, after a delay period($T_e/2$) of 13 milliseconds(ms), by a train of either four selective or four non-selective 180° RF pulses separated by T_e. Data acquisition employed phase-cycled signal averaging. The sequence repetition period(T_R) was 1.0 second(s) for the imaging of the normal lung and 1.5 s for the imaging of the edematous lung. Total scan times for a respiratory-gated image were respectively 15 minutes and 20 minutes when repetition intervals of 1.0 s and 1.5 s were employed.

Three different RF pulse sequences were developed for comparison purposes, all of which made allowance for respiratory gating(see Fig. 3.2.1). Two of the sequences provided for spin conditioning(5), one did not. Spin conditioning is a process whereby a pseudo nuclear spin steady state is established with continual excitation by RF pulse sequences separated by a constant T_R. However, data acquisition for image formation occurs only during a pre-selected portion of the respiratory cycle. The first RF pulse sequence stimulated the nuclear spin system only during data acquisition, thus establishing relatively long periods of RF pulse quiescence. Of the two RF pulse sequences incorporating spin conditioning a difference in

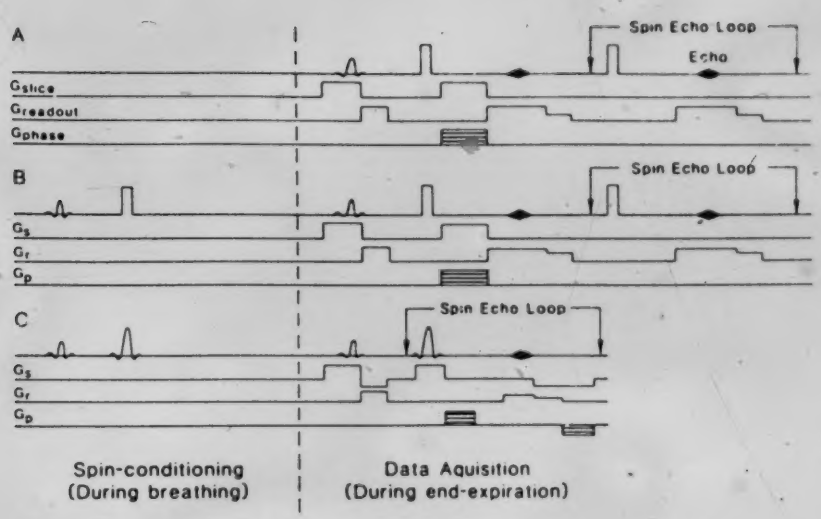

FIGURE 3.2.1: The three different respiratory-gated RF pulse excitation sequences developed for the preliminary in-vivo NMR imaging experiments:

A) no spin conditioning, a selective 90° RF pulse, and four non-selective 180° RF pulses

B) spin conditioning, a selective 90° RF pulse, and four non-selective 180° RF pulses

C) spin conditioning, a selective 90° RF pulse, and four selective 180° RF pulses

the nature of their 180° RF pulses was tested. One employed a selective 180° refocussing pulse, the other a non-selective 180° refocussing pulse. This latter type of 180° pulse was also used within the first pulse sequence where spin conditioning was not employed. The three pulse sequences may therefore be abbreviated as follows:

NSN: NO SPIN CONDITIONING/ SELECTIVE 90°/ NON-SELECTIVE 180°
SCSN: SPIN CONDITIONING/ SELECTIVE 90°/ NON-SELECTIVE 180°
SCSS: SPIN CONDITIONING/ SELECTIVE 90°/ SELECTIVE 180°

3.2.2 Imaging of a Cat Model of Pulmonary Edema:

Prior to imaging, an adult mongrel cat(approx. 4 kg body weight) was sedated with an intra-muscular injection of xylazine hydrochloride(2.2 mg/kg). Atropine sulphate(0.03 mg/kg) was combined in this injection to prevent hypersecretion within the airways. After approximately five minutes, the animal was anaesthetized with an intra-muscular injection of ketamine hydrochloride(20 mg/kg), followed by repeated injections(10 mg/kg) as deemed necessary. A tracheostomy was performed and a 4 mm ID cannula introduced into the central airway. The animal was then placed supine within a plexiglass tray, constructed especially for accomodating animals in a superconducting magnet bore. The animal was ventilated with an Ohio anaesthesia ventilator

(Airco. Inc., Madison, Wisconsin) at a tidal volume of approximately 30 ml and at a rate of approximately 12 breaths/minute. This particular type of ventilator allows for passive expiration, a characteristic essential for our method of respiratory-gated data acquisition. A pressure port on the central airway cannula was connected via plastic tubing to a pressure transducer(model no. 10287, Statham Instru. Co., Oxnard, California) which generated the central airway pressure signal(P_{aw}) for the electronic gating circuit(see Appendix).

Respiratory gating of the NMR spectrometer was achieved by means of a trigger signal which rose from zero to 5 V and so disabled the spectrometer after P_{aw} had passed a threshold of approximately 5.0 millivolts. The disable trigger level was maintained throughout the respiratory cycle created by the ventilator. After the completion of the inspiratory portion of the respiratory cycle, a delay time window of 0.75 s was established to ensure the return of the lungs to their resting position prior to switching off the disable trigger in order to facilitate data acquisition. Data acquisition for image formation occurred during end-expiration, or when the disable trigger was absent, a period of time lasting ~1.5-2.0 seconds. Because of its inherently longer data acquisition period as compared to that achieved by a sinusoidally driven ventilator pump, passive expiration was desired.

The experimental animal was imaged initially in the pre-edematous condition with all three MSE pulse sequences. Pulmonary edema was then bilaterally produced with an endotracheal lavage(5 ml/kg) of 0.1 Normal HCl performed twice to ensure only moderate edema formation. Following the completion of both lavages, imaging was then repeated at intervals of 20-25 minutes with all three RF pulse sequences over the following three hours. Although increasing T_R beyond a value of 1.5 s for imaging of the edematous condition would have increased the signal intensity from the edematous lung regions, it would also have drastically lengthened the total scan time when combined with respiratory gating. Since endotracheal lavage is a dynamic model of pulmonary edema, the signal intensities generating the image will be averages of the accumulating edema fluid taken over the scan period. The longer the total scan time, the greater the change in the lung tissue's water content in such a dynamic model, and the poorer will be the precision of the images' serial representation of the dynamic process. Thus, it was decided to only moderately increase the T_R when imaging the edematous state in order to maintain a practical total scan time.

3.2.3 Phantom Study:

In the study of the stationary phantom, images were acquired with the same three pulse sequences as were used before and the transverse relaxation indices derived from these were compared with T_2 values obtained from in-vitro measurements of the phantom constituents. From the images the quantitative parameters(transverse relaxation indices) were determined by a locally developed region of interest (ROI) software routine. Care was exercised to ensure that the defined ROIs possessed the same size and location within all the images acquired with all of the different pulse sequences. The area defined by an ROI was typically 180 pixels and together with an imaging slice thickness of 3 mm, this represents an approximate volume of 0.43 cm^3. The decay of the signal intensity from the given ROI throughout the MSE train was analysed by means of an exponential curve-fitting routine and the transverse relaxation index evaluated.

To obtain the transverse relaxation time, T_2, of the phantom constitutents, the Carr-Purcell-Meiboom-Gill(CPMG) pulse sequence was employed, incorporating wide bandwidth rectangular 180° pulses separated by 32 ms and administered by means of a sinusoidal coil large enough to ensure a uniform RF field throughout the sample. Three T_R values were selected for this aspect of the investigation: 1.0 s and 1.5 s for comparison with imaging sequences and 15.0 s for

observing the effect of allowing complete recovery of the longitudinal magnetization.

The phantom was composed of TX-150(Oil Centre Research Inc., Lafayette, Louisianna), an organic hydrate which, when mixed in a 1/10 concentration with tap water, produces a homogeneous rubber-like consistency that closely resembles the complex dielectric properties of human tissues(6). The dielectric constant of the resultant composition can be varied over a wide range by altering the TX-150/tap water concentration, while the conductivity can be controlled by the salinity of the TX-150 material itself. It was for these characteristics, together with the closer correspondance of the proton molecular motion of the tissue situation, that this material was chosen over the usual aqueous solutions of paramagnetic ions. This phantom, carefully fashioned to possess a nearly identical filling factor as the anaesthetized experimental animal, was positioned within the same circumscribing RF coil as employed for the in-vivo animal experiments and subsequently imaged both under conditions which simulated spin conditioning(SCSN and SCSS pulse sequences) and under those which did not(NSN pulse sequence). To further reproduce the conditions of the in-vivo animal experiments, respiratory-gated data acquisition was incorporated throughout. In this instance, the mechanical ventilator was made to inflate a collapsible rubber balloon with an identical tidal volume and ventilatory rate as used for the anaesthetized experimental

animal. A pressure port, situated at the neck of the balloon, was again connected via plastic tubing to the transducer which generated the pressure signal for the electronic gating circuit.

3.3. RESULTS:

3.3.1.Imaging of a Cat Model of Pulmonary Edema:

Proton images of the pre-edematous condition are presented in Figs. 3.3.2-3.3.4. Each of these figures illustrates the spin-echo images produced by one or other of the RF pulse sequences employed in this investigation. Although the first echo of each MSE train produced by the three contrasting pulse sequences may be considered to be of acceptable quality, it is in the later echoes that the benefits of the selective 180° pulse in the SCSS pulse sequence become apparent. The later spin echoes produced by the other two pulse sequences contain extensive artefacts along the phase-encoding direction. Indeed, these artefacts are such that any transverse relaxation measurement derived from such images would be of doubtful validity. Consequently no such calculation was attempted from the lung images acquired with either the SCSN or the NSN pulse sequences. In comparing the MSE images acquired with both the SCSS and

SCSN pulse sequences it would seem that these extensive artefacts along the phase-encoding direction are primarily associated with use of non-selective 180° RF refocussing pulses. Images acquired with the SCSN and NSN pulse sequences appear to be equally poor. Thus although not every possible permutation of spin conditioning, non-selective 180° RF refocussing pulses, and selective 180° RF refocussing pulses was investigated, the results obtained suggest that as far as qualitative spin echo image appearance is concerned, the process of spin conditioning alone is of little consequence. Spin conditioning is expected to be important when quantitative conclusions are drawn. In the SCSS case, all four spin echoes produced are of good quality, although a noticeable decline in the signal/noise ratio is apparent with progression through the MSE train(see Fig. 3.3.2). This decline is moreover, above and beyond that which would normally be expected from the exponential decay of signal intensity due to spin-spin interactions.

The same qualitative observations were made of the images depicting the edematous condition. The later echo images acquired with the SCSN and NSN pulse sequences were as poor for the edematous state as they were for those for the normal state. Hence their quality does not warrant display. Nevertheless, the rapid increase of siganl intensity from lung regions as they become increasingly more edematous is immediately apparent in the depicted image,

FIGURE 3.3.1 (A) and (B)

FIGURE 3.3.1: Four MSE images of the upper thorax of a cat, without pulmonary edema, acquired with the SCSS pulse excitation sequence (TR=1.0 s). On the previous page, (A) has Te=26 ms and (B) has Te= 52 ms. On this page, the upper image has Te=78 ms and the lower image has Te=104 ms.

FIGURE 3.3.2: Two spin-echo images from a sequence of four MSE images of the upper thorax of a cat, without pulmonary edema, acquired with the SCSN pulse excitation sequence(TR=1.0 s). In the upper image Te=26 ms and in the lower image Te=78 ms. Note the extensive artefacts present along the phase-encoding axis in the later spin-echo image.

FIGURE 3.3.3: Two spin-echo images from a sequence of four MSE images of the upper thorax of a cat, without pulmonary edema, acquired with the NSN pulse excitation sequence(TR=1.0 s). In the upper image Te= 26 ms and in the lower image Te=104 ms. As in FIGURE 3.3.2, note the extensive artefacts present along the phase-encoding axis in the later spin-echo image.

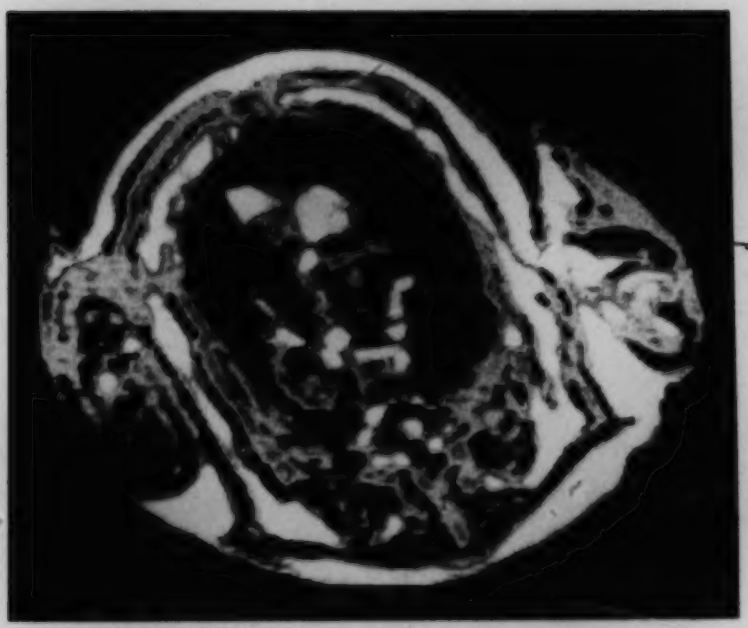

FIGURE 3.3.4: One spin-echo image from a sequence of four MSE images of the thorax of a cat, with pulmonary edema, acquired with the SCSS pulse excitation sequence(TR=1.0 s). In this image Te=26 ms. The NMR imaging slice employed in this figure is not identical to that used in the two previous figures.

acquired within 30 minutes of the bilateral endotracheal lavage(see Fig. 3.3.5). The consequent increase in the calculated proton transverse relaxation index from these regions confirms the previously reported sensitivity of NMRI in detecting this pathophysiological condition (2,4,11,12,14). Quantitative parameters from all the imaging sequences are presented in Table 3.3.1.

3.3.2 Phantom Study:

It is clear from the results of the study of the stationary phantom, that the principal disadvantages of the RF pulse sequences possessing non-selective 180° RF pulses clearly apply to the in-vivo condition only. When the subject of imaging is a stationary phantom lacking blood flow, all three of the RF pulse sequences investigated are capable of producing MSE images of acceptable quality(see Fig. 3.3.6). Indeed, in these circumstances, the imaging RF pulse sequences incorporating non-selective 180° pulses produce an echo train with a substantially prolonged decay time relative to that produced while incorporating selective 180° pulses. The data presented in Table 3.3.2 lists the quantitative parameters of the phantom as derived from the images and from the in-vitro relaxation measurements. These data confirm what might have been expected, namely that the imaging pulse sequences utilizing non-selective 180° pulses

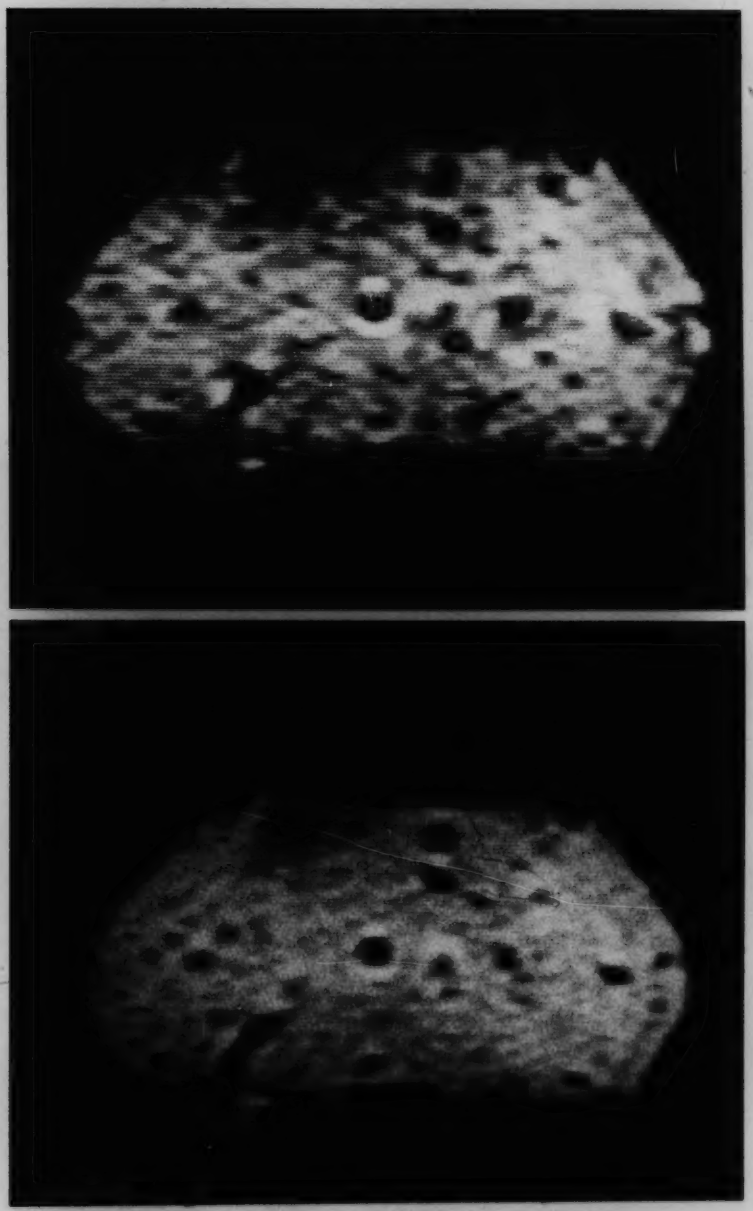

FIGURE 3.3.5 (A) and (B)

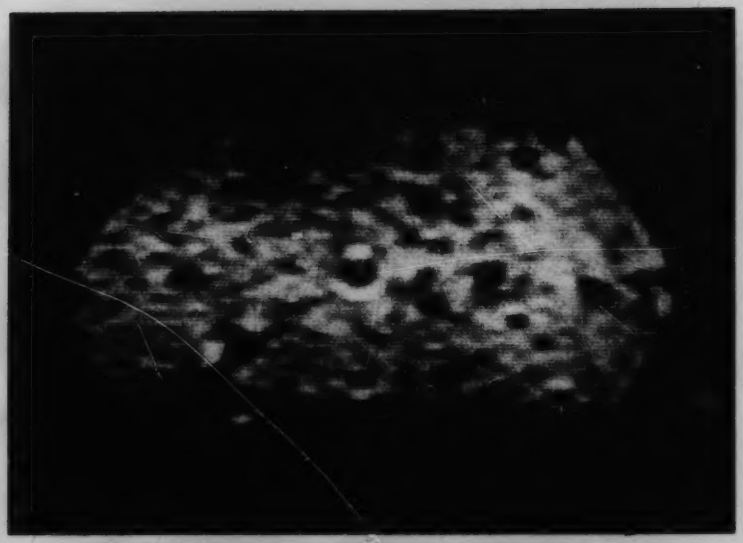

FIGURE 3.3.5: Later spin-echo images of a stationary phantom from sequences of four MSE images produced by the three different RF pulse excitation sequences(TR=1.0 s):

On the previous page,

A) a second spin-echo image, Te=52 ms, acquired with the SCSS pulse excitation sequence.

B) a third spin-echo image, Te=78 ms, acquired with the SCSN pulse excitation sequence. Note the absence of any artefacts along the phase-encoding axis(compare with the later spin-echo image of FIGURE 3.3.2).

On this page,

C) a fourth spin-echo image, Te=104 ms, acquired with the NSN pulse excitation sequence. Note again the absence of any artefacts along the phase-encoding axis(compare with the later spin-echo image of FIGURE 3.3.3).

TABLE 3.3.1 T_2(ms) FROM NMR IMAGES

	Pulse Excitation Sequence:		
	SCSS	SCSN	NSN
Animal: Normal (T_R = 1.0 s)	*	**	**
Animal: Edema (T_R = 1.5 s)	79±3	**	**
Phantom: Complete (T_R = 1.0 s)	81±2	150±2	162±3
Phantom: Complete (T_R = 1.5 s)	82±2	152±2	164±3

Data presented represents the mean of five repetitions ± 1 Standard Deviation. There was no significant difference between T_2 measurements carried out at the two T_R values for any one pulse excitation sequence($p>0.05$).

* No signal present. T_2 calculation not performed.

** No signal and/or extensive artefacts present. T_2 calculation not performed.

TABLE 3.3.2: COMPARISON OF PHANTOM T_2 DETERMINATIONS FROM NMR IMAGES AND FROM SPECTROMETRIC ANALYSIS

Pulse Sequence:	T_R = 1.0 s	T_R = 1.5 s	T_R = 15.0 s
CPMG	152±1 ms	151±1 ms	152±1 ms
SCSS	81±2 ms*	82±2 ms*	-
SCSN	150±2 ms†	152±2 ms†	-
NSN	162±3 ms*	164±1 ms*	-

Data presented represents the mean of five repetitions ± 1 Standard Deviation. Unpaired and paired Student's t-test was used where appropriate. There was no significant difference between T_2 measurements carried out at the T_R values for any one pulse sequence($p>0.05$)

† No significant difference between CPMG T_2 measurements and specified NMR imaging T_2 measurement($p>0.05$).

* Significant difference between CPMG T_2 measurement and specified NMR imaging T_2 measurement($p<0.001$).

produce transverse relaxation indices essentially identical to the T_2 values of the reference in-vitro measurements.

In comparing the images of the phantom acquired with all of the pulse sequences employed, it is apparent that the absence of spin conditioning is difficult to discern through image quality alone. However, when comparing the validity of the quantitative parameters derived from the SCSN and NSN sequence images(see Table 3.3.2) the absence of spin conditioning is clearly apparent.

3.4 DISCUSSION:

This investigation was undertaken in order to develop an optimal RF pulse sequence and data acquisition procedure for acquiring in-vivo MSE images of both the normal and edematous lung. Furthermore, it was desired that these data would be of sufficient quality to enable spatially dependant measurements to be made of an in-vivo transverse relaxation index which would have validity on an absolute scale of T_2. From the results of this investigation, it appears that for the purposes of obtaining quality in-vivo MSE images the inclusion of respiratory gating, of spin conditioning, and of totally selective RF pulses is advantageous. The physical reasons for this are not entirely obvious and the following justification is therefore provided.

Respiratory gating was incorporated into the data

acquisition procedure to accomodate the substantial respiratory motion of the cat. In the absence of gating this motion would produce significant ghosting patterns along the phase-encoding direction of the image during the relatively long scan times required for NMRI. Although techniques of mathematically manipulating either the time or the frequency domain data have been developed to overcome this ghosting(1,3,13) they frequently demand several questionable assumptions, namely, 1) the thorax may be represented by a homogeneous, cylindrical phantom, 2) respiratory motion may be represented by the movement of such a phantom in one single dimension, 3) excursions of the thoracic cage during respiration may be adequately described assuming a constant velocity and 4) the respiratory oscillation pattern remains virtually unchanged throughout an entire 8 to 15 minute data acquisition. We therefore chose not to rely on such mathematical manipulations.

Following the incorporation of respiratory gating into the data acquisition procedure, long periods of RF pulse quiescence are established which necessitate the inclusion of spin conditioning into that procedure. Although the requirement of spin conditioning in the presence of respiratory gating has been previously established(5), a mechanism describing how, in the absence of spin conditioning, systematic errors in T_2 calculations could arise has hitherto been lacking in the clinical NMRI literature. Spin conditioning creates a constant T_R for RF

excitation such that a pseudo steady state is established whereby receiver d.c. offsets and artifactual free induction decay(FID) signals resulting from imperfect refocussing pulses are essentially the same for each excitation. By alternating the phase of the seletive 90° RF pulse, the summation of these error terms reduces to zero when the constitutent averages are added. Thus the perceived spin echo intensity, and any subsequent calculation of relaxation indices, is governed by the spin echo amplitude alone. In contrast however, the absence of spin conditioning would give rise to a highly variable T_R which produces long periods of RF pulse quiescence, as well as periods of frequent excitation. Because of this variable T_R, the error signals described above may vary between successive averages and despite phase alternation of the selective 90° RF pulse, the summed error term will not be completely reduced to zero and will therefore enter into the calculation of spin echo signal intensity. In such a situation, as spin echo amplitude decreases, the perceived signal intensity will appear to decay at a rate different from that which is actually the case. Thus erroneous measurement of relaxation indices would be expected.

This phenomenon is best illustrated by the quantitative results of the stationary phantom study(see Table 3.3.2). The above mechanism is consistent with the observation of longer transverse relaxation indices determined from the gated RF pulse sequence lacking spin conditioning(NSN) than

are obtained from sequences that incorporate it(SCSN and SCSS).

In addition to the inclusion of gating and spin conditioning, RF pulse sequences comprising totally selective RF pulses provided optimal lung images of both the normal and edematous states. The need for selective pulses arises from the large volumetric-blood-flow rate that occurs in the lungs. The lungs are the only organs in the body that receive the entire cardiac output, this being a combination of blood supply for their own nutritive and metabolic needs and that intended for gas exchange within the alveoli. Thus during data acquisition there is a tremendous volume of blood moving through the imaging plane in a highly pulsatile manner.

Non-selective RF pulses excite the nuclear spin system throughout the entire volume of the RF coil. However this RF pulse excitation is not entirely uniform throughout this volume, as it would be in the ideal case, but instead is spatially distributed for several reasons. The imperfect nature of a non-selective 180° RF refocussing pulse will therefore create small but finite XY magnetization components of differing amplitudes throughout the volume of the RF coil outside the slice defined by the selective 90° pulse. When such RF pulses are used in the presence of flow perpendicular to the imaging plane, nuclear spins in the flowing liquid outside of the imaging plane will be excited by any of the 180° pulses in the MSE train. In addition,

components of the FID created by the imperfect 180° pulse may appear in the spin echo acquisition window. However, in contrast to typical clinical pulse sequences, the necessary refocussing required following the simultaneous application of a selective 90° pulse and G_{slice}, is provided after the non-selective 180° pulse in the gradient pulse schemes associated with both the SCSN and NSN imaging pulse sequences(see Fig. 3.3.1A and B). This refocussing gradient pulse rapidly dephases the artefactual FID created by imperfections of the non-selective 180° pulse. Consequently, such artefacts are substantially reduced for the first spin echo. Majumdar et al.(9) have recently described the application of balanced gradients before and after the odd 180° RF pulses as a more complete solution to this same problem.

Flow phantom experiments carried out in our laboratory with liquids flowing normal to the imaging plane, have clearly demonstrated that the phase alternation procedure enables acceptable images to be obtained with pulse sequences incorporating non-selective pulses, provided that the flow is laminar(see Fig. 3.4.1). With laminar flow, the RF excitation will produce spatial distributions of magnetization that are virtually identical for each of the constitutent averages. If the flow is pulsatile however, and synchronized NMR data acquisition is not employed, different magnetization distributions will be generated at positions within the flow vessel for each of the constituent averages.

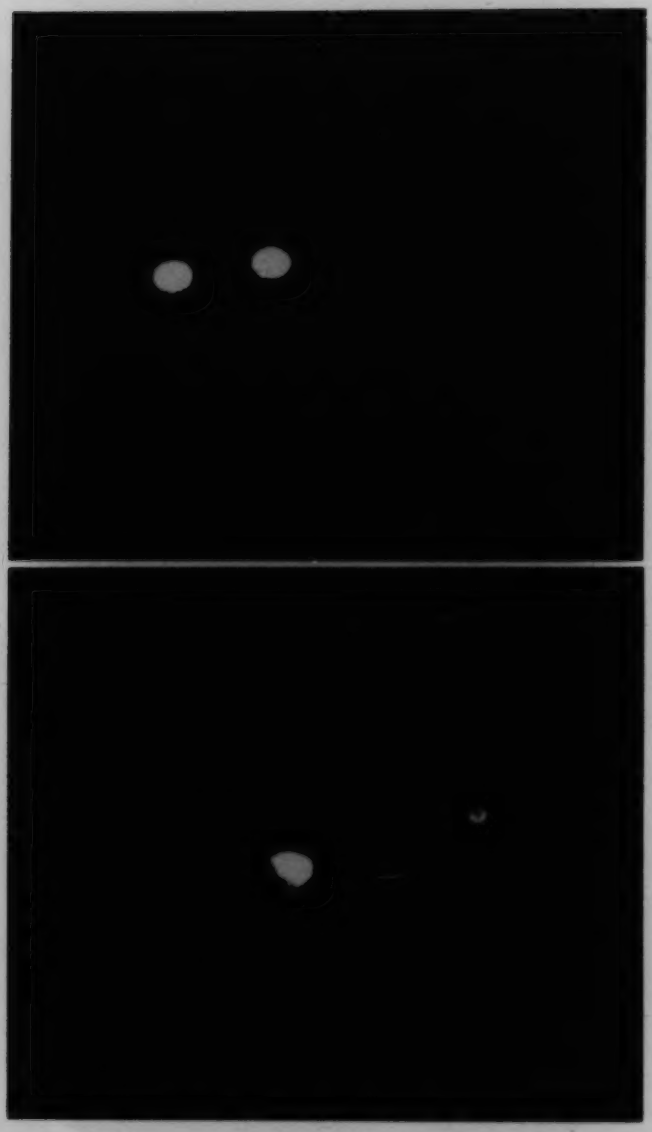

FIGURE 3.4.1: Later spin-echo images from sequences of four MSE images produced by the SCSN pulse excitation sequence, depicting a flow phantom. A U-shaped glass tube was positioned within a large flask containing 0.1M $CuSO_4$ and a transverse section imaged. The small diameter tube in the upper right is a stationary marker denoting the position of the in-flow tube immediately adjacent to it. The linear flow rate was 10 ml/s in all cases.
A) a third spin-echo image, Te=78 ms, of laminar flow
B) a third spin-echo image, Te=78 ms, of pulsatile flow

In addition, successive phase shifts induced by fluid flowing along the gradient are irregular for each of the averages. This will create irregularities in the phase of transverse magnetization components that tend to disrupt the net signal observed during the refocussing of the later echoes. Moreover, phase alternation of the selective 90° RF pulse will no longer minimize the deleterious effects of FID components from the imperfect 180° pulse, which appear in the spin echo acquisition window. Thus with pulsatile flow and non-synchronized data acquisition, these sources of error will combine to produce extensive artefacts along the phase-encoding direction, resulting in the progressively less acceptable quality of the later spin echoes. However, if data acquisition were to be synchronized with this pulsatile flow, these sources of error should be substantially reduced, and consequently allow the employment of non-selective 180° refocussing pulses.

By means of entirely selective RF pulses, the nuclear spins within the flowing blood will not under ideal circumstances be excited until they enter the imaging plane. Thus the problem of creating XY magnetization components within the flowing blood outside of the imaging plane is substantially reduced. The acquired signal data will still however be perturbed a minimal amount due to the nuclear spins within the flowing blood entering or leaving the imaging slice.

Notwithstanding the improvements in image quality afforded by the inclusion of respiratory gating, spin conditioning, and entirely selective RF pulses, the use of selective 180° pulses in an MSE sequence gives rise to its own problems if the sequence is intended to disclose meaningful quantitative information as well. The problems arise first from the inability to completely realign the distributed-phase transverse-magnetization components produced during the selective pulse and secondly from the power spectrum of the RF excitation magnetic field which is non-uniform across the bandwidth of the defined slice, thus causing a distribution of tip angles across the slice thickness. Joseph and co-workers(7), even after optimally shaping a sinc function selective RF pulse and its B_1 field, demonstrated that only near the center of a 1.0 cm thick imaging slice are the nuclear spins rotated through a full 180°. Over the remaining portions of the slice nuclear spin rotation may not even approximate to this value. The resultant transverse magnetization for the entire selectively excited slice is thus a composite of the different individual values existing between the slice boundaries. Measurements of transverse relaxation indices incorporating selective 180° pulses therefore reflect the existence of transverse magnetization phase distributions and do not often correspond to T_2 determinations made in-vitro with uniform B_1 fields(7,8,10). This observation is confirmed in our work by the differences in the T_2

measurements made of the stationary phantom with the various in-vivo RF pulse sequences and of the phantom's constituents with the in-vitro CPMG sequence(see Table 3.3.2). The imaging pulse sequence utilizing non-selective 180° pulses and spin conditioning produces T_2 values essentially identical to those of the reference in-vitro measurement technique(the correlation coefficient of the exponential curve fitting routine was typically 0.99). The non-selective 180° pulses produce much more reliable results since they affect all spins of the stationary phantom identically, provided spatial non-uniformities of the B_1 field are negligible. Consequently, the nuclear spins contained within the imaging plane, as defined by the much more efficient selective 90° pulse, will be uniformly rotated and echo refocussing will be optimal.

In the case of the stationary phantom, quality MSE images may be obtained with a pulse sequence capable of providing transverse relaxation indices possessing validity on an absolute scale of T_2. The more successive quality echo images of the phantom one possesses, the greater the confidence in the validity of these indices. Unfortunately in the in-vivo condition this is not the case. Although the employment of selective RF pulses provides quality MSE images of the in-vivo lung, valid transverse relaxation indices cannot be expected from images so acquired. Under such circumstances the acquisition of quality MSE images and valid quantitative information appear exclusive.

The power requirements needed to generate anything but selective RF pulses on contemporary clinical NMRI systems are prohibitively large. It has been suggested previously that the use of selective 180° pulses in NMR imaging will present serious problems when quantitative information is desired(7,8,10). The results obtained confirm these suggestions. Thus it may be concluded that although selective 180° pulses provide excellent results in MSE image quality of the lung, due caution should be exercised when relating NMRI quantitative parameters that have been acquired with such methodologies.

REFERENCES:

1) Bailes, D.R., D.J. Giderdale, G.M. Byyder, A.G. Collins, and D.N. Firmin. Respiratory ordered phase encoding(rope): a method of reducing respiratory motion artefatcs in mr imaging. J. Comp. Assist. Tomog. 9: 835-838, 1985.

2) Carroll, F.E., J.E. Loyd, K.B. Nolop, and J.C. Collins. MR imaging parameters in the study of lung water: a preliminary study. Invest. Radiol. 20: 381-387, 1985.

3) Cuppen, J.J.M., J.P. Groen, J.J.E. In den Kleef, and H.A. Tuithof. Reduction of motion artefacts by data postprocessing. Proc. 4th Annual Meeting of the Society of Magnetic Resonance in Medicine, London, England: 962-963, 1985.

4) Cutillo, A.G., A.H. Morris, D.D. Blatter, T.A. Case, D.C. Ailion, C.H. Durney, and S.A. Johnson. Determination of lung water content and distribution by nuclear magnetic resonance. J. Appl. Physiol. 57: 583-588, 1984.

5) Ehman, R.L., M. McNamara, M. Pallack, H. Hricak, and C.B. Higgins. Magnetic resonance imaging with respiratory gating: techniques and advantages. Am. J. Roentgenol. 143: 1175-1182, 1984.

6) Guy, A.W.. Analyses of electromagnetic fields induced in biological tissues by thermographic studies on equivalent phantom models. IEEE Transactions on Microwave Theory and Techniques 19: 205-225, 1971.

7) Joseph, P.M., L. Axel, and M. O'Donnell. Potential problems with selective pulses in nmr imaging systems. Med. Phys. 11: 772-777, 1984.

8) Lurie, D.J.. A systematic design procedure for selective pulses in nmr imaging. Mag. Res. Imaging 3: 235-243, 1985.

9) Majumdar, S., S.C. Orphanoudakis, A. Gmitro, M. O'Donnell, and J. Gore. Eroors in the measurement of T_2 using multiple spin-echo technique mri techniques I. effects of radiofrequency pulse imperfections. Mag. Res. in Med. 3: 397-417, 1986.

10) O'Donnell, M., and W.J. Adams. Selective time reversal pulses for nmr imaging. Mag. Res. Imaging 3: 377-382, 1985.

11) Schmidt, H.C., M.T. McNamara, R.C. Brasch, and C.B. Higgins. Assessment of severity of experimental pulmonary edema with magnetic resonance imaging: effect of relaxation enhancement with g-dtpa. Invest. Radiol. 20: 687-692, 1985.

12) Schmidt, H.C., D.C. Tsay, and C.B. Higgins. Pulmonary edema: an mr study of permeability and hydrostatic types in animals. Radiol. 158: 297-302, 1986.

13) Yamashita, M., and T. Maki. Acceleration of respiratory gated imaging by reordered phase encoding in spin warp(2d-ft) method. Proc. 4th Annual Meeting of the Society of Magnetic Resonance in Medicine, London, England: 1064-1065, 1984.

14) Wexler, H.R., R.L. Nicholson, F.S. Prato, L.S. Carey, S. Vinitski, and L. Reese. Quantitation of lung water by nuclear magnetic resonance imaging: a preliminary study. Invest. Radiol. 20: 583-590, 1985.

PHANTOM EXPERIMENTS AND THE ESTABLISHMENT OF A QUANTITATIVE NMR TECHNIQUE FOR THE MEASUREMENT OF LUNG WATER

4.1 INTRODUCTION:

The development of a completely in-vivo quantitative technique was desired for determining T_1, T_2, and proton density(ρ) that would permit the assessment of temporal alterations in the fluid volume, nature, and distribution of oleic acid-induced pulmonary edema. It was a specific intention to employ neither reference nor calibration fluid vials as these are subject to technical limitations. Foremost among these is the inability of liquid solutions to simulate simultaneously the relative and the absolute changes of tissue T_1 and T_2 produced by increased water density.

The quantitative imaging technique was developed with a series of organic hydrate gel phantom experiments. This incorporated a multiple spin-echo(MSE) pulse excitation sequence to provide T_2 indices, and a saturation recovery (SR) RF pulse excitation sequence to provide both T_1 indices and an index of ρ. Quantitative NMR imaging(NMRI) parameters so obtained were verified by in-vitro spectrometric NMR

A version of this chapter has been submitted for publication. Phillips, D.M., Allen, P.S., and Man, S.F.P. 1987. J. Appl. Physiol.

analyses of the phantom gels' constituents.

Unfortunately, the quantitative imaging technique, developed from the phantom experiments to be described in this chapter, did not prove as successful as was desired. NMR image signal intensities acquired both with the SR and MSE pulse excitation sequences consistently displayed an inverse relationship with the phantom gels' water densities. This experimental finding was contrary to what was anticipated. In addition, there was always an appreciable difference between the absolute T_1 value for a phantom gel solution of any given water density and a sample of in-vivo lung tissue possessing a nearly identical water density. The influence of these shortcomings, in regards to the applicability of the developed quantitative imaging technique, will be addressed in greater detail later in this chapter(see section 4.4).

4.2 EXPERIMENTAL:

4.2.1 General Outline:

The phantoms were composed of TX-150(Oil Centre Research, Lafayette, Louisianna), an organic hydrate which, when combined with distilled water(d-H_2O), produces a homogeneous gel possessing dielectric properties that

resemble those of human tissues(2). The gel's dielectric constant may be varied by altering the TX-150/d-H_2O concentration, while the electrical conductivity may be controlled by the salinity of the TX-150 material. It was for these characteristics, as well as for the closer correspondance to tissue proton molecular motion, that this material was chosen over the more common aqueous solutions of paramagnetic ions.

Nine different TX-150/d-H_2O gel solutions were manufactured with the following concentrations, by weight: 1/1.5, 1/2, 1/4, 1/6, 1/8, 1/10, 1/12, 1/14, and 1/16. These particular concentrations were selected for the following reasons. All of the above phantom gel solutions possessed a density of ~1 gm/cm^3 of space(2). Therefore, the corresponding water density values for the above phantom gel solutions were 0.6, 0.67, 0.8, 0.86, 0.89, 0.91, 0.92, 0.93, and 0.94 gm of H_2O/cm^3 of space. Pilot studies concerning in-vivo edematous lung tissue revealed that localized edematous regions exhibiting appreciable NMR signal were markedly atelectatic and possessed a density of between 0.8 and 1.0 gm of wet lung tissue/cm^3 of space. Moreover, normal degassed, or completely atelectatic, lung tissue would not be expected to possess a water density <0.6 gm H_2O/cm^3 of space, while markedly edematous lung tissue would not be expected to exhibit a water density >0.95 gm H_2O/cm^3 of space. Hence, this range of expected lung tissue water density values was therefore effectively approximated by

that of the selected phantom gel solutions. Each gel solution was made anew on the day of experimentation. Constituents of the desired gel solutions were placed in a 250 ml Pyrex beaker and mixed with a magnetic stir-bar for 15 minutes. Completed gel solutions were then each inserted in individual 12 cm plastic test tubes(2.7 cm ID), tightly sealed with a twist cap to prevent dehydration. Care was taken to avoid air pockets in the filled test tubes. The test tubes, grouped together as a bundle whose volume approximated the filling factor of an experimental animal in the RF coil, were then positioned in the magnet bore which was continually warmed by means of a heated air source so as to approximate body temperature (37±1°C.). Static magnetic field shimming to ~0.7 ppm (70 Hz) over the entire sample volume was carried out. The gel solutions were then imaged with gated forms of the MSE and SR sequences. Gating, in this instance, was achieved by inflating a collapsible rubber balloon with the same mechanical ventilator as employed for the in-vivo studies, operating at a similar tidal volume and ventilatory rate. A pressure port, situated at the balloon's neck, was linked via plastic tubing to a pressure transducer which generated the trigger signal for the electronic gating circuit.

Spectrometric analysis of the individual phantom constituents was undertaken immediately afterwards. The desired test tube was emptied of its gel, which had by this time acquired the shape of its container. The position of

the imaging slice was determined and a sample removed from its center. This sample was placed in a dry ultra-centrifuge vial which was then centrally inserted within a solenoidal RF coil large enough to ensure a uniform RF magnetic field , B_1, throughout the sample. To obtain the transverse relaxation time, T_2, the Carr-Purcell-Meiboom-Gill(CPMG) pulse sequence was employed. This used 16 wide-bandwidth rectangular 180° RF pulses separated by 32 ms. The longitudinal relaxation time, T_1, was acquired with an inversion-recovery(IR) pulse sequence, using an initial wide-bandwidth rectangular 180° RF pulse followed, after a variable delay period(T_I), by a single similarly wide-band 90° RF pulse. Ten different T_I values were used for these experiments, ranging from 100 ms to 15 s. Throughout this time, all unanalysed gel solutions remained in their individual test tubes in a heated environment(37°C.). Phantom experiments, for each of the variables studied, were repeated on five separate occasions. All experimentation, both NMRI and subsequent spectrometric analysis, on any one occasion was completed within 4 hours of the gels' initial composition.

4.2.2 Spin Conditioning and Verification of NMRI Parameters:

In a respiratory-gated data acquisition procedure, long periods of RF pulse quiessence are created which necessitate

the inclusion of spin conditioning into that procedure. It has been described(see Chapter 3) how respiratory gating, in the absence of spin conditioning, produces errors in T_1 and T_2 evaluations.

However, the RF pulses of our imaging sequences(see Fig. 4.2.1) do not excite identical volumes for both portions of the respiratory cycle. This is a consequence of an inability to pulse the magnetic-field gradients whenever the receiver is disabled. Since data acquisition is desired during end-expiration, it is during this time only that RF pulses are coupled with magnetic-field gradients. During the remaining portion of the respiratory cycle, RF excitation must occur in the absence of magnetic field gradients. Under these conditions the bandwidth of the selective RF pulses(~500 Hz) would, together with the B_0 inhomogeneity, produce an effective imaging slice of 12 cm(±6 cm from the magnet center). Thus, in any gated imaging experiment, the RF pulses will excite proton spins in a slice whose thickness changes periodically between 12 cm and 3 mm. Because of this, it was imperative to determine if the changes in slice width would result in errors in the measurement of relaxation indices. To establish that it did not, all gel solutions were imaged both with gated and non-gated forms of the MSE(T_R=2 s) and SR(T_R=10.5, 8.4, 6.3, 4.2, and 2.1 s) sequences using non-selective 180° RF pulses(see Fig. 4.2.1A).

Respiratory-gated data acquisition procedures are more

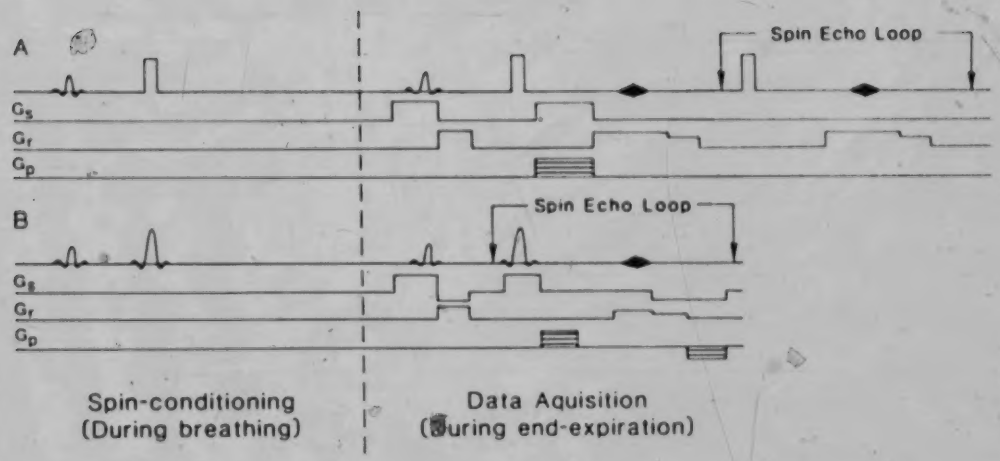

FIGURE 4.2.1: The two imaging RF pulse excitation sequences employed for the phantom experiments:

A) spin conditioning, a selective 90° RF pulse, and four non-selective 180° RF pulses

B) spin conditioning, a selective 90° RF pulse, and four selective 180° RF pulses

time consuming than ungated procedures because of the time lost during the inspiratory portion of the respiratory cycle. In order to contain the time for gated procedures within practical limits, steps are often taken to minimize the T_R values employed between each application of the RF pulse sequence. Such a limitation can lead to incomplete relaxation of one or other or both of the longitudinal and the transverse magnetization, resulting in systematic errors in the measurement of these relaxation indices. It was therefore imperative to confirm that the T_R values incorporated into the gated pulse sequences used in this study did not introduce serious errors in the in-vivo estimates of longitudinal and transverse relaxation indices. In order to verify that serious errors did not arise from this source, NMRI phantom measurements were compared with spectrometric determinations of T_1 and T_2 for the phantom gel constituents. Moreover, the values of T_1 and T_2 determined spectrometrically for the gel constituents provide such assurance, when used in conjunction with the following simple equations:

4.2.1) $M \propto M_0 e^{-t/T_2}$, for the decay of the transverse magnetization,

4.2.2) $M \propto M_0(1-e^{-TR/T_1})$, for the recovery from zero of the longitudinal magnetization,

4.2.3) $M \propto M_0(1-e^{-TR/T_1})e^{-t/T_2}$, for the recovery from zero of the observed magnetization with the employed SR imaging pulse sequence, and

4.2.4) $M \propto M_0(1-2e^{-\tau/T_1})$, for the recovery of the longitudinal magnetization from complete inversion

where M is the proton magnetization at a given time, M_0 is the thermal equilibrium proton magnetization, TR is the pulse sequence repetition time, t in Eqs. 4.2.1 and 4.2.3 is the time between the 90° RF pulse and the first 180° RF refocussing pulse, and τ in Eq. 4.2.4 is the variable time delay, T_I, between the 180° RF inversion pulse and the following 90° RF pulse. As an example, for the most dilute gel constituent with the longest relaxation times, the T_R of 2.0 s used in the MSE pulse sequence allows a 98% decay of the transverse magnetization(see Eq. 4.2.1). Thus, the shortest T_R employed with the SR pulse sequence (2.1 s) also enables 98% decay of the transverse magnetization of this most dilute phantom gel solution. The longer T_1 of the most dilute phantom gel limits the recovery of the longitudinal magnetization to only 90% of M_0, with the longest of the five T_R values(10.5 s) employed with the SR pulse sequence(see Eq. 4.2.2). However, this minor limitation, when used in the spin-conditioned mode, will lead to a

modification of the intercept and therefore to an underestimation of the true M_0, but will not affect the slope of the relaxation curve and therefore the relaxation index(T_1) obtained from it. Longitudinal relaxation for all phantom gel solutions was measured with the IR pulse sequence. The longest T_I value employed, 15 s, would thus ensure 90% recovery of M_0(see Eq. 4.2.4).

4.2.3 Correction for Selective RF Excitation:

The necessity for using selective 180° RF pulses for NMRI of the thorax, in the absence of cardiac synchronization, has been explained previously(see Chapter 3). Since both the MSE and SR imaging sequences employ selective 180° RF pulses for producing the proton spin-echo, appropriate corrections must be made if the resultant images are to provide quantitative relaxation information. This is because selective refocussing pulses will fail to realign completely the distributed-phase transverse-magnetization components, since the RF power spectrum is non-uniform across the bandwidth of the defined slice and because the resonance condition is not exactly satisfied throughout the slice.

In the absence of a satisfactory mathematical description of proton spin dynamics under our particular experimental conditions, it was necessary to provide an

empirical calibration of the in-vivo longitudinal and transverse relaxation indices using the spectrometrically derived T_1 and T_2 of the various gel solutions. The indices were derived from images generated both with non-selective and selective 180° RF pulses and then compared with the appropriate spectrometric measurements. To verify these phantom-based empirical relationships for in-vivo studies, various tissues(muscle, brain, liver, and subcutaneous fat) were imaged in-vivo as described above and the two sets of T_1 and T_2 indices compared.

4.2.4 The Water Density/Integrated Signal Intensity Relationship:

An index of ρ was obtained from plots of longitudinal relaxation derived from the SR sequences and then modified to provide the integrated signal intensity for the employed ROI volume. Provided the proton relaxation behaviour of a gel solution remained constant, larger ROI volumes would include larger amounts of water and hence give rise to greater integrated signal intensities. A relationship was thus established between the phantom gel water density and integrated signal intensity. Under such ideal circumstances, this correlation of a single NMRI parameter with water density would be sufficient to characterize any observed pulmonary edema.

However, temporal changes in the nature of the edema fluid are also commonly observed. When the nature changes, alterations in proton relaxation behaviour will effect the ROI volume-integrated signal intensity in a manner independent of that from changes in the ROI volume. This is because the recovery curve during the selected T_R values of the SR sequence will now differ from that observed prior to the changes in the water proton environment. Knowledge of T_1 and T_2 indices will facilitate the interpretation of alterations in integrated signal intensity but will not easily reveal the extent to which each individual relaxation process has influenced this parameter. In reviewing the in-vitro T_2 values, both of edematous lung tissue and of various pulmonary fluids (3,5-7), one may conclude that T_2 is not the most sensitive NMR parameter for discriminating between different pulmonary edema exudates. However, the results obtained from both these phantom experiments and the in-vivo animal experiments which followed, clearly demonstrated that T_2 is by far a more discriminating NMR parameter than T_1. This observation has recently been confirmed with T_1 and T_2 analyses of various concentrations of in-vitro protein solutions(1). Nevertheless, with careful selection of the T_R values to be used in the SR sequence, it was possible to minimize the influence of the slightly incomplete transverse decay on the integrated signal intensity obtained with a 5-image SR sequence of any one phantom gel solution. This is because T_2 can thus be made a

constant component in the signal intensitites obtained for each of the constituent images of the SR sequence. However, as the employed SR pulse sequence produces images manifesting T_2 weighting(see Eq. 4.2.3), and because T_2 changed with increased phantom gel water density, the alterations in integrated signal intensity, in cases where ROI volume was constant, were then created by changes in both the longitudinal and transverse relaxation and ρ. It was intended that an empirical relationship would be established between phantom-gel water density and the integrated signal intensity based on this argument.

In a separate experiment, all gel solutions were imaged with the SR sequence, using the same T_R values as in the NMRI study concerned with the verification of the NMRI phantom T_1 indices. The integrated signal intensity was calculated for each gel solution using identical ROI volumes. As one would not expect a water density <0.6 gm H_2O/cm^3 of space in any form of degassed or atelectatic lung tissue, the phantom gel solution possessing this water density value(solution 1/2) was selected as the baseline for determining the influence of increased water density on ROI volume-integrated signal intensity. The corresponding alterations in integrated signal intensity, produced by the differences in phantom gel water density, were then determined for each case and an empirical relationship established between phantom gel water density and integrated signal intensity. An identical set of all gel solutions was

then imaged as before and these same variables related. However, in this instance, twelve different pairs of ROI volumes were employed for the calculation of the change in integrated signal intensity with increased phantom gel water density. The average for all twelve ROI volume pairs, in addition to the associated limits of uncertainty, was then calculated. In so doing, the influence of ROI volume, and thus a larger number of water protons, on the difference between the integrated signal intensities of any two different phantom gel solutions could be accounted for. Any remaining portion of the difference between the two integrated signal intensities could therefore be assigned to both T_1 and T_2 effects, combined with an increased ρ.

4.3. RESULTS:

The effects on the measured relaxation rates of including respiratory-gating and spin conditioning in the data acquisition procedures are summarized in Tables 4.3.1-4.3.2 and Figs. 4.3.1-4.3.2.

When selective 180° RF pulses are used in the MSE pulse sequence, the T_2 indices(see R_2'' in Table 4.3.1) markedly underestimate the actual T_2 values. Moreover, the degree of this underestimation is dependent upon the water content of the phantom gel.

Longitudinal relaxation measurements of the phantom gels are presented in Table 4.3.2. The gated 5-image SR sequence using a single non-selective 180° RF refocussing pulse gave rise to T_1 indices in very reasonable agreement with the spectrometrically-determined phantom gel T_1 values(see Fig. 4.3.2). The minor underestimation of T_1 associated with the more dilute phantom gels did not exceed 10% of the spectrometrically-determined values. The 5-image SR sequence, when used in conjunction with gating and a single selective refocussing 180° RF pulse(see R_1'' in Table 4.3.2) produced an underestiamtion of the spectrometrically-determined T_1 values, the degree of which was essentially constant(or independent of the phantom gel) at 29-35%.

T_1 and T_2 indices of in-vivo animal tissues obtained from both the SR and MSE imaging sequences were compared to the empirical relationships provided in Figs. 4.3.1 and 4.3.2. T_1 and T_2 indices, when measured with selective refocussing pulses, were of the same magnitude relative to those measured with non-selective refocussing pulses for both in-vivo tissues and phantom gel solutions. This finding thus increased the degree of confidence in the ability to correct for the effects of selective refocussing pulses.

The signal intensity asymptote of the phantom gels, expressed per NMR imaging pixel, is presented in Table 4.3.3 and Fig. 4.3.3. As one would expect, altering the ROI volume within any one phantom gel solution did not appreciably effect the measurement of this NMR parameter.

TABLE 4.3.1: TRANSVERSE RELAXATION(sec^{-1}) OF PHANTOM GELS

Phantom Gel Concentration [TX-150/d-H_2O]	R_2	R_2'	R_2' ng	R_2''
1/1.5	23.3	23.5	23.6	*
1/2	17.5	17.6	17.6	*
1/4	13.2	13.3	13.3	28.8
1/6	10.6	10.8	10.9	25.0
1/8	8.6	8.7	8.6	19.0
1/10	6.5	6.6	6.6	14.5
1/12	3.8	3.8	3.8	9.8
1/14	2.5	2.5	2.5	7.6
1/16	1.9	1.9	1.9	6.4

* = unable to measure accurately

FIGURE 4.3.1

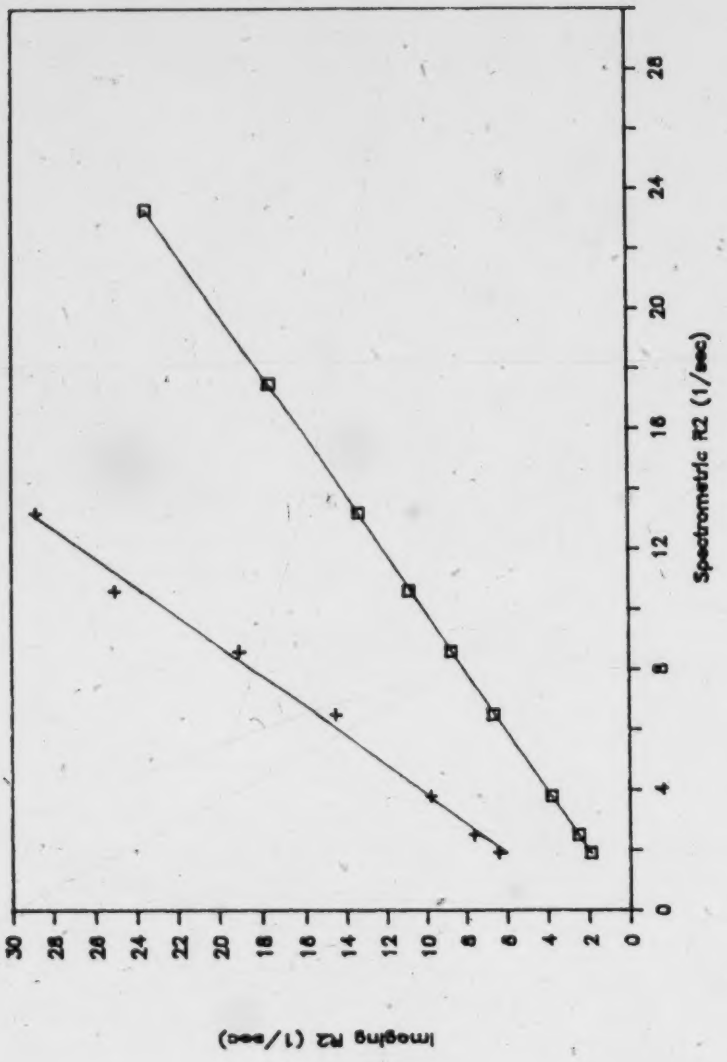
Imaging R2 (1/sec)
Spectrometric R2 (1/sec)
0
2
4
6
8
10
12
14
16
18
20
22
24
26
28
30
0
4
8
12
16
20
24
28

TABLE 4.3.2: LONGITUDINAL RELAXATION(sec^{-1}) OF PHANTOM GELS

Phantom Gel Concentration [TX-150/d-H_2O]	R_1	R_1'	R_1' ng	R_1''
1/1.5	0.446	0.480	0.471	0.630
1/2	0.415	0.432	0.424	0.580
1/4	0.366	0.374	0.372	0.500
1/6	0.343	0.360	0.353	0.488
1/8	0.276	0.290	0.285	0.400
1/10	0.245	0.260	0.257	0.370
1/12	0.226	0.240	0.236	0.330
1/14	0.215	0.230	0.224	0.320
1/16	0.200	0.220	0.216	0.310

FIGURE 4.3.2

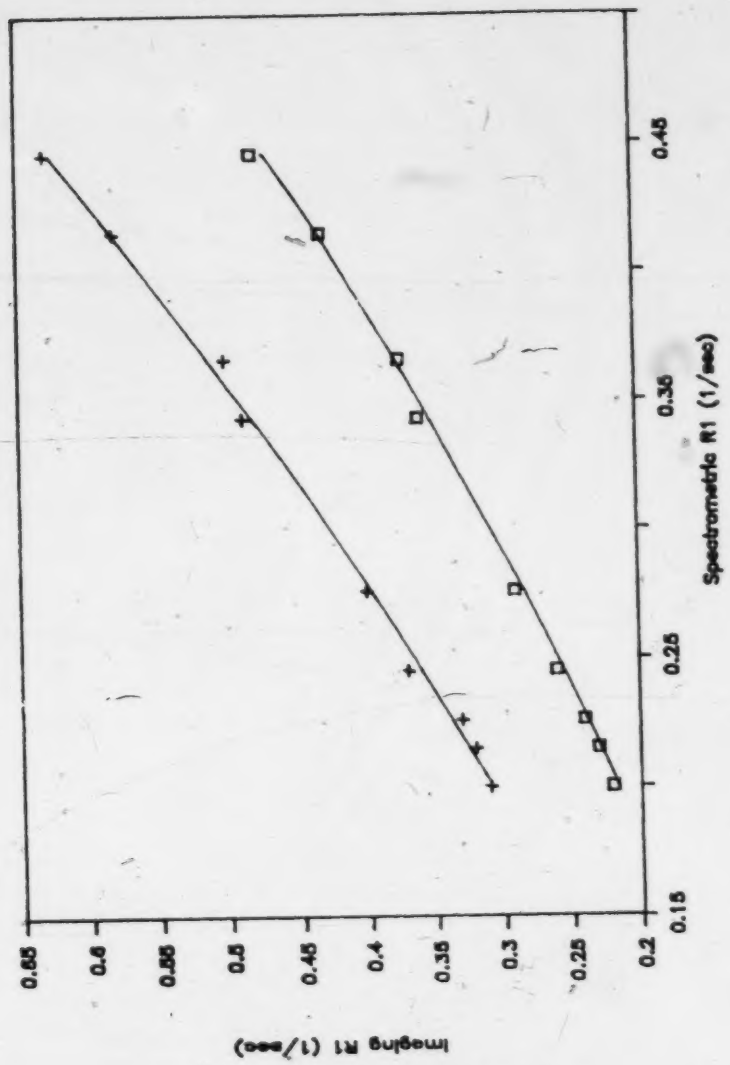
Imaging R1 (1/sec)
0.65
0.6
0.55
0.5
0.45
0.4
0.35
0.3
0.25
0.2
0.15
0.25
0.35
0.45
Spectrometric R1 (1/sec)

TABLE 4.3.3: ESTIMATE OF SIGNAL INTENSITY ASYMPTOTE FOR PHANTOM GELS

Phantom Gel Concentration [TX-150/d-H_2O]	Phantom Gel H_2O Density (gm H_2O/ml)	Signal Intensity Asymptote	Normalized Asymptote
1/1.5	0.60	67000	1.00
1/2	0.67	66000	0.99
1/4	0.80	64000	0.96
1/6	0.86	63000	0.95
1/8	0.89	60000	0.90
1/10	0.91	57000	0.86
1/12	0.92	52000	0.78
1/14	0.93	48000	0.73
1/16	0.94	41000	0.62

FIGURE 4.3.3

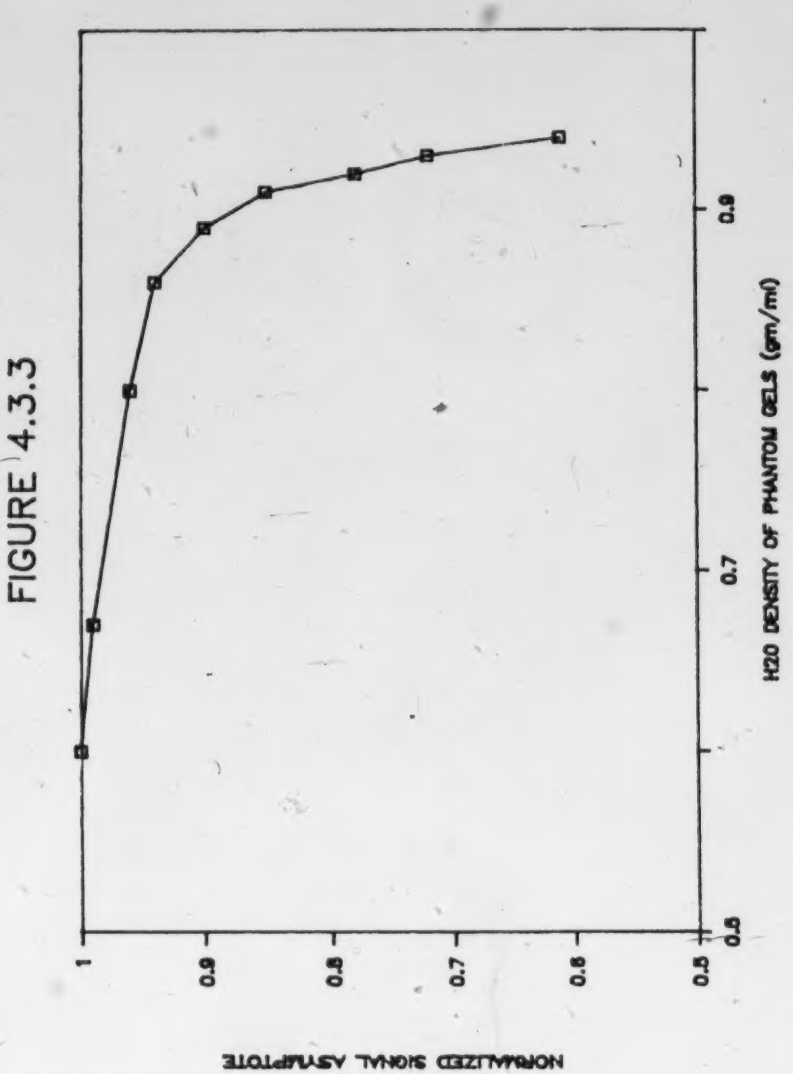
NORMALIZED SIGNAL ASYMPTOTE
1
0.9
0.8
0.7
0.6
0.5
H20 DENSITY OF PHANTOM GELS (gm/ml)
0.5
0.7
0.9

TABLE 4.3.4: THE PHANTOM GEL WATER DENSITY/ INTEGRATED SIGNAL INTENSITY RELATIONSHIP

ΔWater Density of Phantom Gels from Baseline*	ΔIntegrated Signal Normalized to Baseline
0.07	0.01
0.20	0.04
0.26	0.06
0.29	0.10
0.31	0.15
0.32	0.22
0.33	0.28
0.34	0.39

*Baseline = 0.6 gm H_2O/cm^3 of space

FIGURE 4.3.4

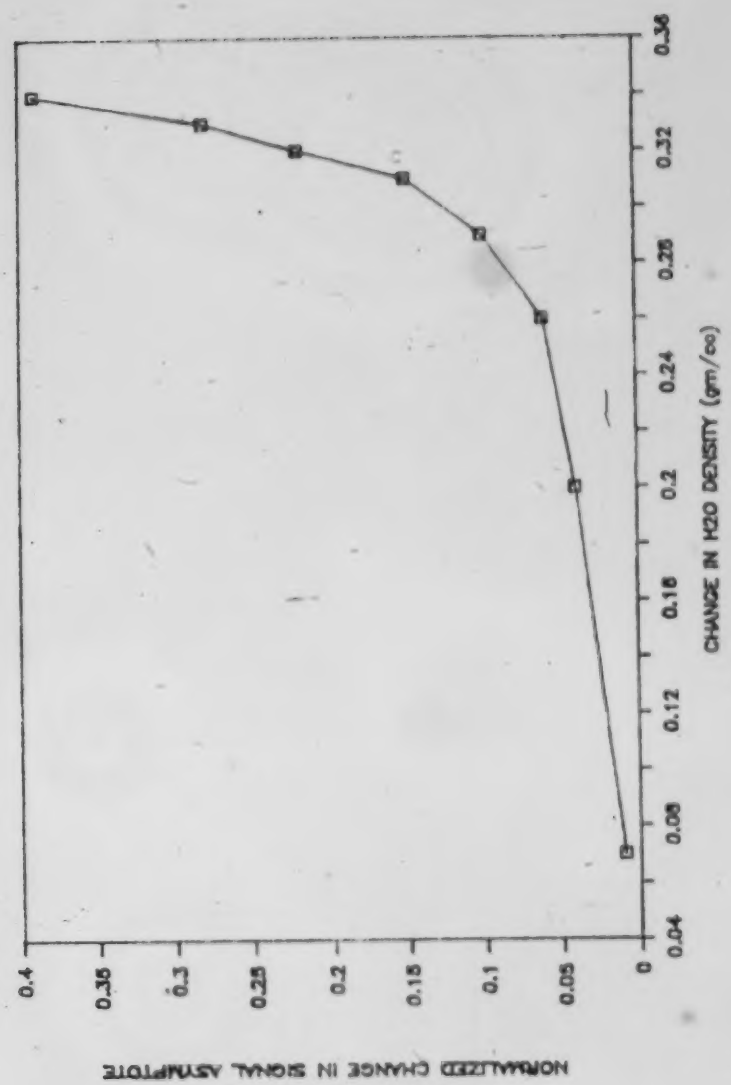
NORMALIZED CHANGE IN SIGNAL ASYMPTOTE
0.4
0.35
0.3
0.25
0.2
0.15
0.1
0.05
0
0.04
0.08
0.12
0.16
0.2
0.24
0.28
0.32
0.36
CHANGE IN H2O DENSITY (gm/cc)

The relationship between changes in phantom gel water density and integrated signal intensity is presented in Table 4.3.4 and Fig. 4.3.4 and represents the proposed means for quantifying in-vivo pulmonary edema. The associated limits of uncertainty for determining the integrated signal intensities would not exceed those pertaining to the measurement of the signal intensity asymptote/imaging pixel. These limits were ±3% of the calculated value for the signal intensity asymptote(see Table 4.3.3).

4.4 DISCUSSION:

The results obtained clearly demonstrate that exciting proton spins within an NMRI slice whose thickness periodically changes between 12 cm and 3 mm does not produce sigificant errors in the measurement of either T_1 or T_2 indices. There is no doubt that some effect does exist, but its magnitude would appear to be within the limits of uncertainty of the NMR experiment.

The studies concerning the phantom gels' transverse magnetization decay revealed that the greater the T_2 of the phantom gel, the greater was the underestimation of the transverse relaxation, when derived from images acquired with the MSE pulse sequence employing selective 180° RF refocussing pulses. The longer the transverse magnetization decay, the longer the echo train will persist and the

greater will be the cummulative effect of the selective refocussing pulses' inability to completely realign the distributed-phase transverse magnetization. The need for a calibration curve, when interpretating T_2 indices acquired with selective refocussing pulses, is graphically illustrated by Fig. 4.3.1.

The underestimation of the more dilute phantom gels' longitudinal relaxation, as derived from the SR pulse sequence employing a single non-selective 180° RF refocussing pulse, is principally due to the T_R values of the SR sequence allowing only incomplete recovery of the longitudinal magnetization for the more dilute gel solutions. The fact that, when using the SR pulse sequence incorporating a single selective 180° RF refocussing pulse, the underestimation of the phantom gels' longitudinal relaxation was independent of phantom gel water content results from using only a single selective 180° pulse. This contrasts with the cummulative effects of successive selective refocussing pulses used to determine phantom gel T_2 indices from images. Another benefit of employing only single spin-echo images to derive T_1 indices is the improvment in both S/N and exponential curve fitting, which in turn give rise to a smaller measurement error.

Measurements of phantom gel signal intensity asymptote/NMR imaging pixel reflect a decrease with increasing phantom gel water density. This is contrary to what one would expect from the mathematical model commonly

used to describe the single spin-echo SR pulse sequence(4):

$$M \propto M_0(1-e^{-TR/T_1})e^{-t/T_2}$$

where TR is the pulse repetition time and t is the time interval between the 90° RF pulse and the single 180° RF refocussing pulse. From this model, NMR signal intensity would be expected to increase with increasing water density since the ROI volumes used for the more dilute gel solutions contain more mobile water protons than do identical ROI volumes used for the more concentrated gel solutions. Increasing phantom gel water density also affects the acquired signal intensity by increasing the T_1 of the associated gel solution. Thus, although the more dilute gel solutions contain more mobile protons within a given ROI volume, the fixed T_R values of the SR sequence inhibit the recovery of the longitudinal magnetization of the more dilute gel solutions and thus limit the acquisition of NMR signal. However, the influence of the increased ρ and, more importantly, the longer T_2 values associated with the more dilute gel solutions should exceed this T_1 effect and establish an increasing signal intensity asymptote with increased phantom gel water density. Nevertheless, this phenomenon of decreasing signal intensity with increasing water density was consistently observed throughout all the phantom experiments in addition to all the in-vivo animal experiments which followed. One must therefore conclude

that: 1) the signal intensity asymptote was influenced by increased phanton gel water density primarily through a mechanism that, at this time, unfortunately remains unaccountable, or that 2) this observed phenomenon was manifested through either the employed NMR spectrometer hardware(i.e. the program-control board or the analoque-to-digital convertor) or the NMR image reconstruction algorithms or both.

Notwithstanding the inability to account for this phenomenon and to appropriately correct for its presence, one should still be able to assess alterations in water density through the associated changes in the ROI volume-integrated signal intensity asymptote, as has been accomplished.

The established quantitative technique, together with the phantom water density/integrated signal intensity relationship, was therefore applied to the quantification and description of in-vivo pulmonary edema.

REFERENCES:

1) Allen, P.S., M.E. Castro, E.O. Treiber, J.A. Lunt, and D.P.J. Boisvert. A proton nmr relaxation evaluation of a model of brain edema. Phys. Med. Biol. 31: 699-711, 1986.

2) Guy, A.W.. Analyses of electromagnetic fields induced in biological tissues by thermographic studies on equivalent phantom models. IEEE Trans. on Microwave Theory and Techniques 19: 205-225, 1971.

3) Podgorski, G.T., F.E. Carroll, and R.E. Parker. MR evaluation of pulmonary interstitial and intravascular fluids. Invest. Radiol. 21: 478-482, 1986.

4) Rosen, B.R., I.L. Pykett, and T.J. Brady. Spin lattice relaxation time measurments in two-dimensional nuclear magnetic resonance imaging: correction for plane selection and pulse sequence. J. Comp. Assist. Tomog. 8: 195-199, 1984.

5) Schmidt, H.C., M.T. MacNamara, R.C. Brasch, and C.B. Higgins. Assessment of severity of experimental pulmonary edema with magnetic resonance imaging: effect of relaxation enhancement by g-dtpa. Invest. Radiol. 20: 687-692, 1985.

6) Schmidt, H.C., D.G. Tsay, and C.B. Higgins. Pulmonary edema: an mr study of permeability and hydrostatic types in animals. Radiol. 158: 297-302, 1986.

7) Skalina, S., H.L. Kundel, G. Wolf, and B. Marshall. the effect of pulmonary edema on proton nuclear magnetic resonance relaxation times. Invest. Radiol. 19: 7-9, 1984.

THE IN-VIVO QUANTIFICATION AND DESCRIPTION OF OLEIC ACID-INDUCED PULMONARY EDEMA WITH NMR IMAGING

5.1 INTRODUCTION:

Nuclear Magnetic Resonance imaging(NMRI), with its marked sensitivity to alterations of the mobile proton environment in tissues, represents a potential analytic tool for the non-invasive study of pulmonary edema. Despite several preliminary studies that have successfully correlated lung water content of excised tissue with in-vitro water proton relaxation time measurements(4,9,22-24,27) there unfortunately remains a paucity of in-vivo data. This is due to the numerous technical difficulties associated with obtaining reliable quantitative NMRI parameters from the in-vivo lung. Moreover, since the NMR signal is influenced by proton density(ρ), and both longitudinal(T_1) and transverse(T_2) relaxation, single parameter correlations with lung water content do not represent a complete picture of pulmonary edema. Remember from Chapter 2.2 that both T_1 and T_2 provide an index of proton mobility and that proton density provides an index of the number of protons/unit volume. A more complete understanding of pulmonary edema would thus arise from the

A version of this chapter has been submitted for publication. Phillips, D.M., Allen, P.S., and Man, S.F.P. 1987. J. Appl. Physiol.

separation of the NMR signal into its T_1, T_2, and ρ components, and observing the correlation of each to changes in lung water content.

The successful imaging technique described in Chapter 3 was coupled to respiratory-gated data acquisition procedures and applied in two series of in-vivo pulmonary edema investigations. One of these experimental series ended at the onset of observable edema within the acquired images, while the second followed the course of the induced edema over 4-5 hours. In both instances, quantitative imaging data were correlated with post-mortem lung water analyses.

The results obtained demonstrated NMRI to be remarkably sensitive in detecting temporal changes in the volume, nature, and distribution of induced pulmonary edema.

5.2 EXPERIMENTAL:

5.2.1 Imaging System and RF Pulse Sequences:

All NMR data were acquired at 2.35 Tesla(T) in a 40 cm bore magnet and employing a modified Bruker CXP spectrometer (Bruker Spectrospin, Karlsruhe, West Germany). Slice gradient strengths of 3.5 mT m^{-1} resulted in an imaging slice thickness of approximately 3.0 mm and an in-plane spatial resolution of 1.72 mm by 0.86 mm for a 128x256 raw

data matrix interpolated to a 256x256 pixel image matrix. The inhomogeneities of the RF magnetic field, B_1, and the static magnetic field, B_0, over an imaging volume representative of an experimental animal (cat), have been measured at 10% and 7 parts per million (ppm) respectively.

Proton transverse relaxation indices from the experimental animals were obtained from images generated with an MSE pulse sequence(see Fig. 5.2.1). This consisted of a selective 90° RF pulse followed, after a delay period ($T_e/2$) of 13 milliseconds(ms), by a train of four selective 180° RF pulses separated by T_e. The need for using selective 180° RF pulses within an MSE sequence, for in-vivo thoracic NMRI in the absence of cardiac-cycle-synchronized data acquisition, has been described previously(see Chapter 3). However, the use of selective refocussing pulses necessitates appropriate corrective measures if meaningful T_2 information is to be obtained(see section 4.2.2).

The relaxation indices of the longitudinal magnetization were derived from a 5-image SR pulse sequence. Each image was acquired with a selective 90° RF pulse followed, after 13 ms, by a single selective 180° RF pulse. Five different sequence repetition times(T_R) were used to complete the SR experiment, the values chosen depended upon the subject matter imaged. The receiver attenuation was adjusted for the longest T_R and then maintained throughout the entire five-image sequence. Although the SR sequence is really a single spin-echo sequence, images acquired at

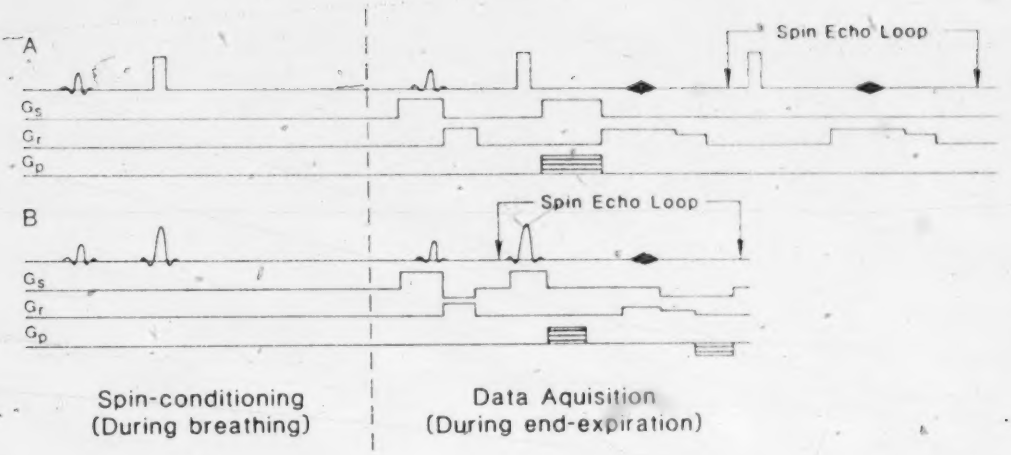

FIGURE 5.2.1: The imaging RF pulse excitation sequence employed for the later in-vivo NMR imaging experiments:

B) spin conditioning, a selective 90° RF pulse, and four selective 180° RF pulses

Only pulse excitation sequence B was employed for the later in-vivo NMR imaging experiments.

different T_R values will relate T_1 information so long as the shortest T_R employed allows complete transverse decay. Data acquisition both for the MSE and SR imaging pulse sequences incorporated phase-alternated signal averaging, with two averages obtained for each of the phase-encoding gradient steps. From the plot of longitudinal magnetization recovery, derived from the 5-image SR sequence, an index of ρ was provided by the asymptote of signal intensity per imaging pixel. This signal intensity asymptote value was then multiplied by the region of interest(ROI) volume in order to provide the total integrated signal intensities from the ROIs. In analysing the images, care was taken to ensure that within one recovery sequence the defined ROIs possessed identical size and location. The ROI signal intensity was then corrected for background noise, which is located predominantly along the phase-encoding axis. The decay of the noise-corrected signal intensity, within a given ROI throughout any imaging sequence, was analysed by means of an exponential curve-fitting routine and the appropriate relaxation index evaluated. The volume defined by an ROI, in all in-vivo imaging sequences, never exceeded 0.57 cm^3. From the information outlined earlier concerning the degree of inhomogeneity in both B_0 and B_1 over the entire volume of an experimental animal, one may conclude that over a 0.57 cm^3 volume both B_0 and B_1 were essentially uniform.

In-Vivo Experiments:

The two series of in-vivo studies involved adult cats and were concerned with following the temporal changes in the volume, nature, and distribution of pulmonary edema as induced by the intravenous injection of oleic acid.

All experimental animals were initially sedated with an intramuscular injection of xylazine hydrochloride(Rompun, 2.2 mg/kg). Atropine sulphate(0.03 mg/kg) was combined in this injection to prevent hypersecretion within the airways. After approximately five minutes, the animals were anaesthetized with an intramuscular injection of ketamine hydrochloride (Rogarsetic, 20 mg/kg), followed by repeated injections(10 mg/kg) when necessary. A tracheostomy was performed and a 4 mm ID cannula introduced into the central airway. A polyethylene catheter was placed within the common carotid artery for monitoring arterial blood gas tensions throughout the course of the experiment. A similar catheter was passed, via the external jugular vein, to the right atrium. The animals were then placed supine in a plexiglass tray, constructed for accommodating animals in the imaging magnet bore. The animals were mechanically ventilated (Harvard Apparatus Co., South Natick, Mass.) with room air, at a tidal volume of 30 ml, and at a rate of 12 breaths/minute. A pneumotachograph (no. 18522, Statham Instru. Co.), positioned immediately distal to the ventilator's outflow port, was connected via plastic tubing

to a differential pressure transducer(no. PM15E, Statham Instru. Co.) which generated the respiratory cycle pressure signal for the electronic gating circuit. The gating circuit generated a trigger signal which rose from zero to 5 volts(V) and so disabled the spectrometer after the pressure signal had passed a threshold of ~5.0 mV. The disable trigger was maintained throughout the respiratory cycle created by the ventilator. After the completion of the respiratory cycle, a delay time window of 0.75 seconds(s) was established to ensure the return of the lungs to their functional residual capacity volume, prior to lowering the disable trigger for data acquisition.

Experimental animals of series A(7 animals, mean body weight = 4 kg) were first imaged in the normal condition with the respiratory-gated MSE sequence operating with a T_R of 1.0 s. The imaging slice was positioned at the upper lung lobes in order that cardiac-motion artefacts would be absent from subsequent images. Oleic acid(0.075 ml/kg) was then injected via the external jugular catheter and NMRI repeated with the MSE pulse sequence operating at a T_R of 1.5 s. Immediately afterwards, the five-image SR sequence was initiated. The T_R values chosen for the in-vivo experiments were 2.5, 2.0, 1.25, 0.75, and 0.35 s. These values ensured at least a 90% decay of the transverse magnetization for tissue protons possessing a T_2 of up to 148 ms, and a minimum of 90% recovery of the longitudinal magnetization for tissue protons possessing a T_1 of up to 1.064 s(see

section 4.2.2). These relaxation ranges were anticipated from a review of relaxation data on edematous lung tissue (3,4,9,22-24,27). Moreover, after considering the extra time required for gating, these TR values represent the practical limits of imaging the relatively dynamic process of oleic acid-induced pulmonary edema. Acquisition of one MSE and one five-image SR sequence required nearly two hours and constituted a complete NMRI parameter dataset. As a consequence of the extended data acquisition time, the images represent averages of edematous tissue parameters over the time required to complete a dataset. The first dataset served as baseline for assessing the subsequent temporal changes in pulmonary-edema volume, nature, and distribution.

Prior to each image, routine checks were made on the RF coil tuning, the shimming, and the RF pulse power. Static magnetic field shimming was always undertaken to ~0.7 ppm (70 Hz) over the volume of the cat within the RF coil. Arterial blood samples were withdrawn at the end of MSE imaging of the normal lung, and both prior to and following the five-image SR sequence of the edematous lung. Measurement of arterial blood gas tensions and hemoglobin (Hb) was performed immediately. A second NMRI dataset was then acquired in an identical fashion to the first. Images were analysed for T_1 and T_2 indices, ρ , and ROI volume as detailed previously. A two-way analysis of variance was performed, the statistical significance of the acquired F

ratio being assessed as $p<0.05$. NMRI parameters were examined for differences between the ventral and dorsal (gravity-dependent) portion of any one lung, between identical portions of opposite lungs in the same animal, and between identical lung regions of the two experimental series.

At the end of the study the animals were sacrificed with a lethal dose of sodium-pentobarbitol(Nembutal, 100 mg/kg). While remaining in the plexiglass tray and in the identical supine position, the imaging slice was first marked over the thorax, and then the animals were placed within an insulated container of pelleted dry-ice(-79°C.). The container was sealed and the process of whole-body freezing allowed to continue for 48 hours.

Animals of series B(3 animals, mean body weight = 3.5 kg) were imaged in the normal condition as performed for those of series A. After checking the NMRI slice position, oleic acid (0.075 ml/kg) was injected and imaging repeated. However, in this series, NMRI terminated at the initial observation of edema. This corresponded closely to the NMRI parameter baseline established for series A, and typically followed the completion of one MSE sequence. The animals were then sacrificed and immediately placed in the dry-ice container. The NMRI slice was then marked and the container sealed for 48 hours. The chief purpose for series B was to establish the extravascular-lung water(EVLW) content in the imaged lung tissue at a time corresponding to the NMRI

baseline. These values then provided the EVLW baseline for assessing subsequent changes in lung water content. The single T_2 index obtained for this series served as a consistency check.

5.2.2 Post-Mortem Analysis of EVLW:

The intact, frozen thorax of each animal was sectioned with a band-saw to represent the imaging slice employed during the in-vivo studies. The limitations of this technique restricted the minimum section thickness to 5 mm. Since the NMRI slice was only 3 mm thick, an artefactual difference between the EVLW measurements conducted via NMRI and via the post-mortem technique may have been introduced. Lung tissue within each section was first divided into ventral and dorsal, right and left lung regions. All grossly edematous regions(easily discernable in the frozen section as clearly defined, hemorrhagic areas) were then removed from these lung divisions and analysed separatley. Very good spatial correlation was consistently demonstrated between the location of these edematous regions as presented both in the frozen lung sections and the corresponding NMR images. All lung tissue was first weighed and then dryed at 25°C. to constant weight. The wet-to-dry ratio(W/D) was calculated separately for the grossly edematous regions as well as for all remaining tissue within each lung section. These W/D

values were then combined such that a W/D was obtained for both the ventral and dorsal lung divisions of each entire lung section. Each dryed lung tissue sample was then placed in a glass vial, a saline aliquot of known volume(5 ml) added, and the sample uniformily homogenized. Resultant samples were centrifuged at 2500 rpm (~1350 g) for 45 minutes and examined via a diode array spectrophotometer (no. 8451A; Hewlett-Packard, Avondale, Penn.) for Hb absorption at 540 nm. Edematous regions and all surrounding tissue within each lung section were separately analysed for EVLW content, incorporating the techniques both of Pearce et al.(19) and Hemingway(12). Results obtained were combined and then expressed for both the ventral and dorsal lung divisions of each entire lung section.

Total blood mass(Q_b) was calculated from:

$$Q_b = ([Hb]_h/[Hb]_b) \times Q_{wl} \times (SG_h/SG_b) \times PHct \qquad (5.2.1)$$

where $[Hb]_h$ and $[Hb]_b$ represent the homogenate and blood Hb concentrations, measured in gm/ml, respectively. Q_{wl} is the wet lung mass in grams, SG_b and SG_h are the specific gravity of the blood(1.052) and the homogenate(1.027) respectively, and PHct is the pulmonary hematocrit correction factor (1.055) established as an appropriate correction, by both Pearce et al.(19) and Rappaport(21), when using systemic blood samples as a reference for pulmonary blood Hb. Blood water volume(W_b) was determined from:

$$W_b = Q_{Hb} \times (1/[Hb]_b) \times SG_b \times PHct \qquad (5.2.2)$$

where Q_{Hb} represents the Hb mass, in grams, contained within the homogenate. Blood protein content(P_b) was calculated using:

$$P_b = 0.07 \text{ gm/ml} \times Q_{Hb} \times (1/[Hb]_b) \qquad (5.2.3)$$

Dry lung tissue mass(Q_{dl}) may therefore be expressed as:

$$Q_{dl} = Q_{td} - (P_b + Q_{Hb}) \qquad (5.2.4)$$

where Q_{td} represents the total dry lung mass, measured in grams. Wet lung mass(Q_{wl}) follows as:

$$Q_{wl} = Q_b + Q_{dl} + EVLW \qquad (5.2.5)$$

Rearranging terms permits the relationship:

$$EVLW = Q_{wl} - (Q_b + Q_{dl}) \qquad (5.2.6)$$

Division of the EVLW by SG_h enables its expression in ml.

Measurements of lung sample EVLW and W/D for both series A and B animals were examined via a two-way analysis of variance, the statistical significance of the acquired F ratio being assessed as $p<0.05$. Differences in the measurements outlined above were evaluated between ventral

and dorsal portions of the same lung, between identical portions of opposite lungs of the same animal, and between identical lung regions of the two experimental series. As EVLW measurements of series B lung samples represented our baseline, temporal changes in EVLW, as assessed by the above post-mortem technique, were compared to values predicted by NMRI.

5.3 RESULTS:

5.3.1 In-Vivo Animal Experiments:

Arterial blood gas tensions for all experimental animals are presented in Table 5.3.1. Control measurements, for both series, undertaken 20-25 minutes after the start of mechanical ventilation, indicate hyperventilation. Measurements coincident with early and later pulmonary edema, performed at 30 minutes and 2 hours after the injection of oleic acid respectively, reflect the progressive degradation of alveolar gas exchange in the presence of increased lung water. No active intervention was undertaken to prevent the onset of both respiratory failure and the resultant metabolic acidosis. Final measurements for series A and B were performed 4-5 and 1.5-2 hours following oleic acid injection respectively.

The image ROI volumes, corresponding to the edematous lung regions of series A animals, are presented in Table 5.3.2. Since the normal lung is devoid of NMR signal in the images, these ROI dimensions provide an index of the volume for each animal's edematous regions. The acquisition of in-vivo T_1, T_2, and ρ will provide a more complete and accurate determination of EVLW, as assessed by NMRI. In the first NMRI dataset, ~2 hours after oleic acid injection, there were no significant differences in volume between the edematous regions($p>0.05$), whether in the same or in the opposite lungs. Thus initially, edema became apparent in an essentially uniform distribution. However, such a uniform distribution was not seen in the second NMRI dataset, obtained at ~4-5 hours after oleic acid injection. This second dataset revealed significantly greater edematous volumes within the dependent regions of both lungs($p<0.05$). More importantly, edematous ROI volumes(see Table 5.3.2) of ventral lung regions did not change appreciably over the course of the experiment ($p>0.05$), whereas those of the dorsal lung regions increased by a highly significant extent($p<0.01$).

A first spin-echo image of the normal condition, generated by the gated MSE sequence, is displayed in Fig. 5.3.1 and shows the lack of NMR signal from the lung as previously mentioned. Fig. 5.3.2 represents a first spin-echo image depicting the initial edematous condition. Both the scattered distribution and uniform nature of the edema

fluid are apparent. Results from the first 5-image SR sequence gave rise to edema characteristics virtually identical to those observed in the initial MSE sequence. However, the SR sequence from the second dataset, Fig. 5.3.3, displayed temporal changes in both regional edema distribution and T_1 indices. The edema distribution had become more extensive in dependent lung regions and the associated longitudinal relaxation indices were increased.

Longitudinal relaxation indices of series A are presented in Table 5.3.3. As observed when discussing the ROI volume data, the first NMRI dataset showed no significant difference between the T_1 indices of any two regions($p>0.05$), whether in the same or in opposite lungs. The second NMRI dataset however, while presenting effectively equal T_1 indices for identical regions of opposite lungs($p>0.05$), revealed a highly significant difference between T_1 indices of ventral and dorsal lung regions($p<0.01$). There were also highly significant differences between the T_1 indices of any one region over the course of series A experiments($p<0.01$), reflecting temporal alterations in regional T_1 indices. Ventral lung regions presented a decrease in T_1 indices(maximum decrease = 34%) over the course of all series A experiments, whereas dependent lung regions displayed an increase in T_1 indices(maximum increase = 56%) over the same time period.

Transverse relaxation indices of series A are presented in Table 5.3.4. Regional differences in these indices, both

FIGURE 5.3.1: The first spin-echo image, Te=26 ms, from a sequence of four MSE images depicting the upper lung lobes of a cat, without pulmonary edema.

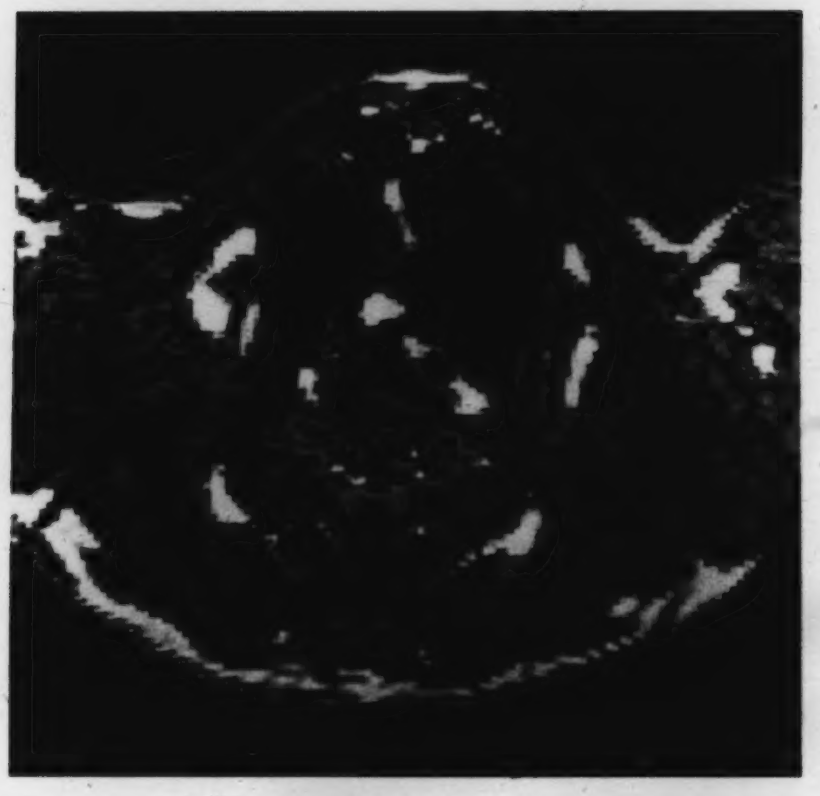

FIGURE 5.3.2: The first spin-echo image, Te=26 ms, from a sequence of four MSE images depicting the initial edematous condition in the upper lung lobes of a cat. This image was acquired approximately 2 hours after the intravenous injection of oleic acid(0.075 ml/kg). The initial 5-image SR sequence revealed essentially identical information.

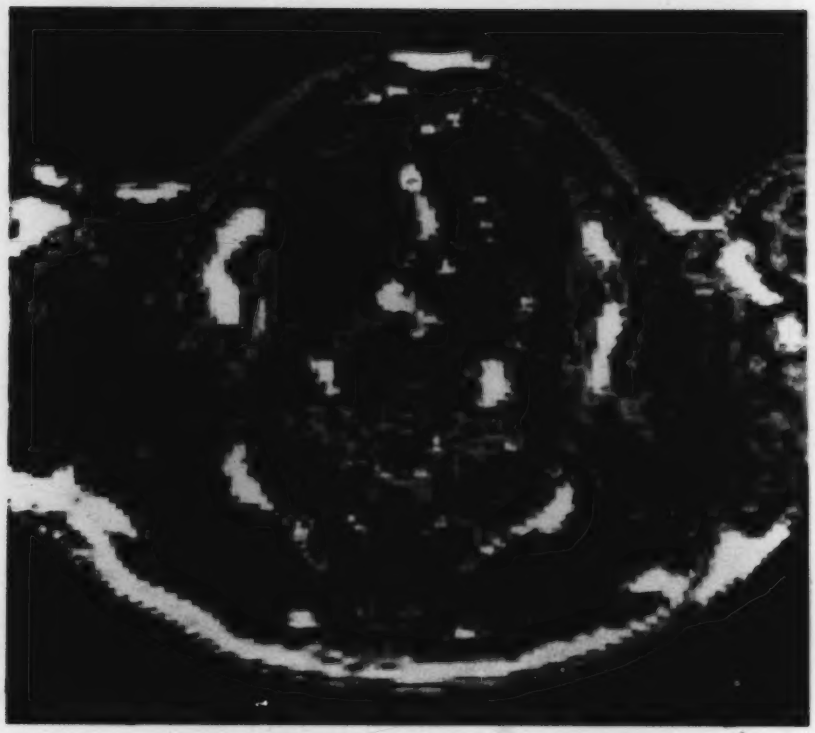

FIGURE 5.3.3: The first image of a 5-image SR sequence, TR=2.5 s, depicting the later edematous condition in the upper lung lobes of the same experimental animal as is shown in FIGURE 5.3.2. This image was acquired approximately 4 hours after the intravenous injection of oleic acid(0.075 ml/kg). The later MSE imaging sequence revealed essentially identical information, although the degree of regional variation in T_2 did not equal that of T_1.

for the same and for opposite lungs in all NMRI datasets, were not significantly large($p>0.05$). Although over the course of the experiment, regional T_2 indices followed the same trend as the T_1 indices, the changes in these T_2 indices never achieved significance ($p>0.05$). The T_2 indices of lung regions in series B experiments displayed the same uniform distribution as those observed in the temporally-equivalent first NMRI dataset of series A experiments.

Finally, the NMR signal intensity asymptote was calculated for the ROIs and then multiplied by the ROI volume to provide the total integrated ROI signal intensity, and thus an index of ρ , for this same volume. Application of the relationship between water density and integrated signal intensity(see section 4.2.3) enabled a measurement of EVLW to be made in those regions where a simultaneous change had occurred in edema volume and both T_1 and T_2 indices. In 2 of the 13 experimental animals, edematous lung regions observed within the NMR images were difficult to partition into ventral and dorsal lung region components that would accurately correspond to the excised edematous lung tissue samples. In these cases, all edematous regions of the afflicted lung were combined to produce a post-mortem EVLW measurement for the entire lung section and then compared to a correspondingly combined value predicted by the NMRI.

TABLE 5.3.1: ARTERIAL BLOOD GAS TENSIONS

Series	Time of Measurement	pO_2 (mm Hg.)	pCO_2 (mm Hg.)	pH
A	Control	84 ± 7	24 ± 4	7.5 ± 0.1
	30 Minutes	66 ± 7	30 ± 9	7.4 ± 0.1
	2 Hours	60 ± 8	33 ± 9	7.3 ± 0.1
	4-5 Hours	48 ± 6	39 ± 8	7.0 ± 0.1
B	Control	84 ± 3	26 ± 2	7.5 ± 0.1
	30 Minutes	69 ± 1	29 ± 1	7.4 ± 0.1
	1.5-2 Hours	61 ± 3	31 ± 1	7.3 ± 0.1

Measurement times, other than control, are expressed as the time elasped since the injection of oleic acid

TABLE 5.3.2: REGION OF INTEREST [ROI] VOLUMES

FOR SERIES A EXPERIMENTS

Cat No.	Ventral Left Volume (cm^3)	Dorsal Left Volume (cm^3)	Ventral Right Volume (cm^3)	Dorsal Right Volume (cm^3)
First Dataset (1.5-2 Hours after oleic acid)				
1	0.086	0.115	0.134	0.311
2	0.191	0.151	0.117	0.100
3	0.237	0.495	0.115	0.134
4	0.292	0.144	0.173	0.158
5	0.352	0.310	0.273	0.272
6	0.263	0.182	0.193	0.139
7	0.182	0.124	0.229	0.110
Second Dataset (4-5 Hours after oleic acid)				
1	0.141	0.134	0.275	0.554
2	0.287	0.280	0.193	0.153
3	0.106	0.513	0.344	0.359
4	0.169	0.182	0.100	0.090
5	0.186	0.514	0.209	0.405
6	0.153	0.301	0.100	0.258
7	0.124	0.342	0.327	0.337

TABLE 5.3.3: LONGITUDINAL RELAXATION TIME [T_1] INDICES(sec) OF SERIES A EXPERIMENTS

Cat No.	Ventral Left Index	Dorsal Left Index	Ventral Right Index	Dorsal Right Index
First Dataset(1.5-2 Hours after oleic acid)				
1	0.9 ± 0.1	0.98 ± 0.08	1.0 ± 0.2	1.0 ± 0.1
2	1.2 ± 0.2	1.19 ± 0.05	1.2 ± 0.1	0.93 ± 0.03
3	0.98 ± 0.03	1.0 ± 0.2	0.9 ± 0.1	0.92 ± 0.07
4	0.92 ± 0.04	0.92 ± 0.02	0.92 ± 0.04	0.96 ± 0.04
5	0.97 ± 0.01	1.04 ± 0.07	1.07 ± 0.01	0.94 ± 0.04
6	0.92 ± 0.02	0.92 ± 0.01	0.90 ± 0.03	0.97 ± 0.02
7	0.89 ± 0.08	0.91 ± 0.08	0.91 ± 0.09	0.90 ± 0.08
Second Dataset(4-5 Hours after oleic acid)				
1	0.73 ± 0.09	1.5 ± 0.1	0.7 ± 0.1	1.4 ± 0.1
2	0.79 ± 0.08	1.5 ± 0.2	0.90 ± 0.03	1.45 ± 0.06
3	0.85 ± 0.02	1.23 ± 0.03	0.88 ± 0.05	1.3 ± 0.1
4	0.68 ± 0.07	1.33 ± 0.05	0.71 ± 0.02	1.37 ± 0.01
5	0.81 ± 0.09	1.3 ± 0.1	0.86 ± 0.07	1.4 ± 0.2
6	0.89 ± 0.02	1.43 ± 0.09	0.66 ± 0.02	1.35 ± 0.05
7	0.77 ± 0.07	1.3 ± 0.1	0.83 ± 0.08	1.4 ± 0.1

TABLE 5.3.4: TRANSVERSE RELAXATION TIME [T_2] INDICES(msec.) OF SERIES A EXPERIMENTS

Cat No.	Ventral Left Index	Dorsal Left Index	Ventral Right Index	Dorsal Right Index
First Dataset(1.5-2 Hours after oleic acid)				
1	77 ± 3	76 ± 4	79 ± 5	76 ± 4
2	74 ± 3	71 ± 1	78 ± 9	78 ± 5
3	79 ± 5	78 ± 5	80 ± 9	83 ± 6
4	71 ± 5	74 ± 3	76 ± 5	78 ± 5
5	75 ± 6	76 ± 6	74 ± 4	78 ± 7
6	79 ± 5	81 ± 6	79 ± 5	80 ± 6
7	80 ± 5	79 ± 5	81 ± 6	81 ± 5
Second Dataset(4-5 Hours after oleic acid)				
1	74 ± 5	78 ± 4	79 ± 7	80 ± 6
2	76 ± 7	75 ± 4	82 ± 8	86 ± 6
3	75 ± 6	85 ± 4	76 ± 4	85 ± 8
4	69 ± 3	79 ± 5	70 ± 4	85 ± 6
5	71 ± 4	82 ± 5	72 ± 3	81 ± 5
6	75 ± 5	86 ± 7	77 ± 6	85 ± 6
7	76 ± 4	85 ± 6	79 ± 5	87 ± 7

5.3.2 Post-Mortem Measurements of EVLW:

Table 5.3.5 presents both the post-mortem gravimetric W/D and EVLW measurements for both the ventral and dorsal lung tissue samples corresponding to the image slices of series A and B experiments. Although in series A there was considerable variation in both W/D and EVLW values from one lung sample to another, definite trends were established. Samples from dependent lung regions possessed consistently greater W/D values than those from non-dependent regions, although this was more pronounced for the left lung($p<0.01$) than for the right($p<0.05$). Series B lung samples displayed these same general trends, but these trends never achieved significance($p>0.05$). For these laboratories, lung W/D values for normal cats are 2/1-3/1. Thus, one may conclude that the oleic acid(0.075 ml/kg) produced a degree of edema ranging from moderate to extensive.

The EVLW measurements of both series display the same trends as the W/D measurements. Dependent lung regions of series A possessed significantly greater amounts of EVLW ($p<0.05$) than non-dependent regions, although the degree of difference was never so great as for the W/D values from the same regions. The EVLW values for series B were essentially uniform throughout(no significant difference, $p>0.05$). In addition, they clearly reflect a less edematous condition.

ROI wet lung tissue density was calculated by dividing the wet lung tissue mass, after appropriate correction for

the discrepancy between the thicknesses of the frozen lung sections and the NMRI slice, by the ROI volume. Edematous ROIs of the ventral lung displayed a wet lung tissue density ranging between 0.803 and 0.985 gm/cm^3 of space, whereas those of the dorsal lung dislayed a temporal increase in wet lung tissue density from 0.813 to ~1.0 gm/cm^3 of space. As normal aerated cat lungs present a wet lung tissue density of ~0.33 gm/cm^3 of space, one may conclude that the observed edematous ROIs contained markedly atelectatic lung tissue possessing an elevated tissue water content. With the above data and the W/D for these same edematous ROIs, it is possible to calculate the corresponding wet lung tissue water densities. The edematous ROIs of the ventral lung displayed a water density ranging between 0.623 and 0.764 gm H_2O/cm^3 of space, whereas those of the dorsal lung displayed a temporal increase in water density from 0.691 to 0.875 gm H_2O/cm^3 of space. The range of ventral lung tissue water density is approximated quite well by the difference in water density between phantom gel solutions 1/1.5(0.6 gm H_2O/cm^3 of space) and 1/4(0.8 gm H_2O/cm^3). The temporal increase in dorsal lung tissue water density was represented equally well by the difference in water density between phantom gel solution 1/2(0.67 gm H_2O/cm^3) and 1/8(0.89 gm H_2O/cm^3),(see section 4.2.1).

EVLW measurements for series A samples are presented with the corresponding NMRI-predicted values in Table 5.3.6 and Fig. 5.3.4. Although NMRI reflected the trends seen in

TABLE 5.3.5: POST-MORTEM ENTIRE LUNG TISSUE SAMPLE WET TO DRY RATIO AND EVLW(ml)

Cat No.	Ventral Left W/D	Ventral Left EVLW	Dorsal Left W/D	Dorsal Left EVLW	Ventral Right W/D	Ventral Right EVLW	Dorsal Right W/D	Dorsal Right EVLW
	Series A							
1	3.6	0.48	4.5	0.83	2.3	0.33	2.4	0.73
2	4.4	0.30	5.3	0.35	4.8	0.37	5.1	0.44
3	5.3	0.36	5.9	0.53	5.7	1.00	5.9	1.02
4	5.6	0.23	5.7	0.22	5.9	0.60	6.7	0.70
5	3.9	0.24	4.0	0.68	3.3	0.41	3.5	0.64
6	4.6	0.22	4.9	0.45	4.7	0.33	5.6	0.33
7	5.3	0.60	5.7	1.04	5.1	0.50	5.2	0.58
	Series B							
1	3.2	0.32	2.9	0.33	3.3	0.32	3.2	0.33
2	3.4	0.29	3.8	0.29	3.5	0.30	4.0	0.32
3	3.4	0.33	3.7	0.33	3.2	0.32	3.4	0.33

TABLE 5.3.6: EVLW VOLUMES(ml) FOR SERIES A EXPERIMENTS

Cat	Lung Region	Post-Mortem EVLW	NMR-Predicted EVLW
1	VL	0.48	0.41
	DL	0.83	0.73
	VR	0.33	0.29
	DR	0.73	0.64
2	VL	0.30	0.26
	DL	0.35	0.30
	VR	0.37	0.33
	DR	0.44	0.38
3	VL	0.36	0.31
	DL	0.53	0.47
	VR	1.00	0.84
	DR	1.02	0.92
4	VL	0.23	0.20
	DL	0.23	0.21
	VR	0.60	0.51
	DR	0.70	0.64
5	Left Lung	0.92	0.80
	Right Lung	1.05	0.94
6	VL	0.22	0.19
	DL	0.45	0.40
	VR	0.33	0.28
	DR	0.33	0.30
7	Left Lung	1.64	1.46
	Right Lung	1.08	0.98

FIGURE 5.3.4

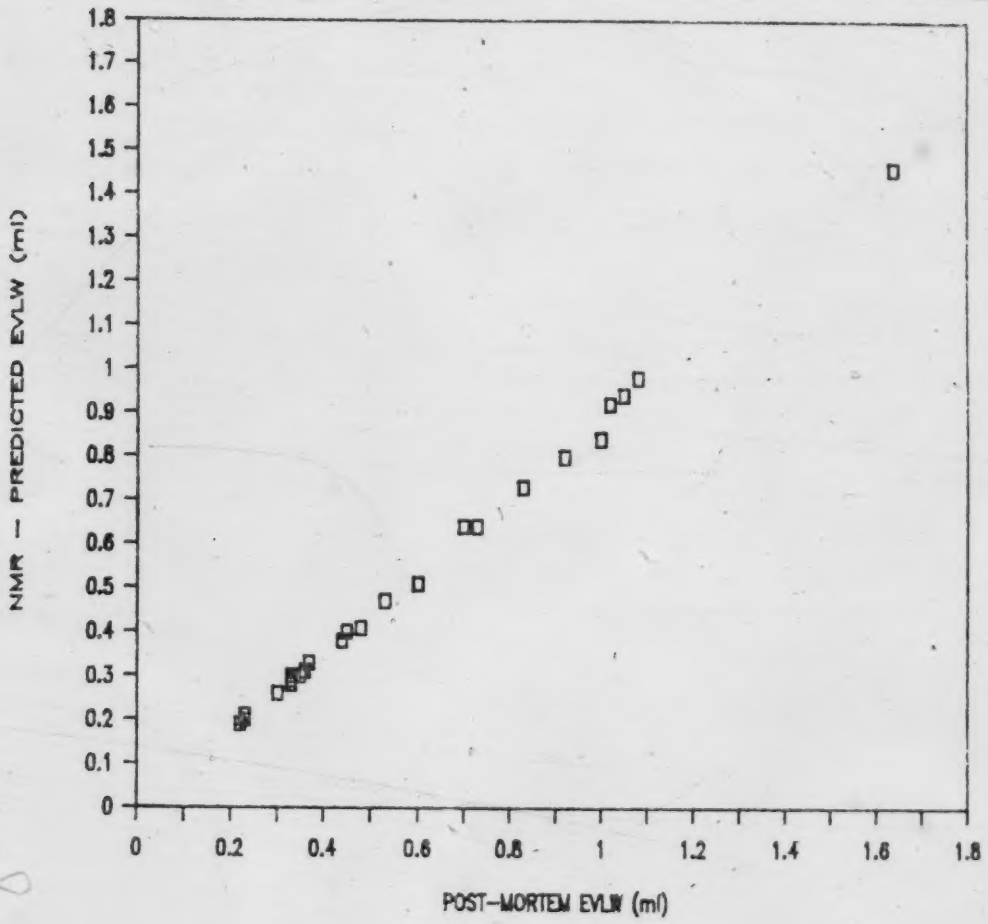
NMR - PREDICTED EVLW (ml)
POST-MORTEM EVLW (ml)
0
0.1
0.2
0.3
0.4
0.5
0.6
0.7
0.8
0.9
1
1.1
1.2
1.3
1.4
1.5
1.6
1.7
1.8
0.2
0.4
0.6
0.8
1
1.2
1.4
1.6

EVLW measurements (r^2 = 0.998), it consistently underestimated the absolute values (maximum degree of underestimation = 16%).

5.4 DISCUSSION:

This study was undertaken to evaluate an in-vivo quantitative NMRI technique for the assessment of temporal changes in the volume, nature, and distribution of oleic acid-induced pulmonary edema. It was the chief objective to exploit the three NMRI parameters(T_1, T_2, and ρ), to obtain more than one single correlation with lung water characteristics. It was also a particular intention not to rely upon reference or calibration fluid vials because of the technical limitations which they introduce and which were discussed in section 4.1.

The foremost concern was whether or not T_1 and T_2 indices derived from respiratory-gated images, would be reasonable approximations of the spectrometrically determined T_1 and T_2. The phantom study revealed that the gated pulse sequences do indeed provide acceptable indices of proton relaxation times(see section 4.3).

The normal lung was not used as the NMRI baseline because of the very low signal-to-noise ratio(S/N) obtained from normal lung tissue when it is imaged without cardiac-cycle-synchronization. Moreover, it is possible that certain

NMR images of the normal lung, appearing in the literature, which do possess an apparent gravity-dependent distribution of signal intensity, do not necessarily reflect a gravity-dependent lung water distribution. Such an apparent distribution of the very weak signal intensity could equally reflect the background noise variation along the phase-encoding direction, since the phase-encoding gradient in many clinical NMR scanners is oriented along the gravity-dependent axis(i.e. top to bottom) when observing transverse images of a supine patient or experimental animal. When corrected for noise along this axis, my images present the normal lung as being virtually devoid of NMR signal. Therefore, the NMRI parameter baseline was chosen to be when edema was first observed.

Measurements of relaxation indices over time enable an assessment to be made of the temporal changes in the nature of the pulmonary edema exudate. For example, changes of the edematous proton environment, induced through changes in protein concentration, coagulation of extravasated blood, and accumulation of interstitial fluid can be discerned. The relaxation indices and ROI volume-integrated signal intensity values then allow one to differentiate alterations in edema volume from those in edema exudate nature.

The significant difference between the W/D values of ventral and dorsal series A lung regions is suggestive of post-mortem drainage of extravasated blood and EVLW occurring within the interstitial tissues. This conclusion

was formulated after considering the W/D measurements for series B lung samples(see Table 5.3.5), which corresponded to an earlier stage of the induced pathophysiology. Series B samples did not display significant gravity-dependent W/D values, as less time was available for the extravasation of blood constituents. In addition, as the entire vertical dimension of all imaged lung lobes was <1.75 cm, pulmonary perfusion pressures throughout the different regions of any one imaged lung lobe would reflect only a small degree of gravity-dependency. Consequently, although there was likely some post-mortem intravascular drainage to dependent lung regions in both normal and mildly-edematous lung tissue (series B), this drainage does not appear to have produced significant gravity-dependent values for either W/D or EVLW measurements (see Table 5.3.5, series B lung samples).

The underestimation of EVLW made by the NMRI quantification technique is due principally to the NMRI-predicted EVLW values being derived from SR imaging sequences, which required 1.5-2 hours for completion. Throughout this time, progressive changes in edema volume continually occurred. Consequently, the acquired T_1 images and the integrated signal intensity values, together with their associated ρ values, represent underestimations of the actual edematous condition at the end of the imaging sequence. In addition, regional differences in EVLW content would most certainly continue to be established throughout the early portion of the whole-body freezing. Consequently,

discrepancies between regional EVLW as indicated in the NMR images and in the post-mortem lung sections would be likely. Finally, the influence of T_1 changes upon the signal intensity asymptote may not have been identical for both the phantom gel solutions and the in-vivo lung tissue. The change in lung tissue water density over the course of series A experiments was well represented by the difference in water density between the phantom gel solutions 1/2 (0.67 gm H_2O/cm^3) and 1/8 (0.89 gm H_2O/cm^3). Moreover, the baseline for these changes in water density was very similar in both instances, 0.69 gm H_2O/cm^3 for lung tissue and 0.67 gm H_2O/cm^3 for the phantoms. A 50% increase in T_1 was experienced in moving from phantom gel solution 1/2 (T_1=2.41 s) to solution 1/8 (T_1=3.62 s), whereas a 42% increase in T_1 (from an average of 0.97 to 1.38 s) was experienced with the in-vivo lung tissue in undergoing an essentially identical increase in water density. However, in absolute terms, the values of T_1 for the in-vivo lung tissue and the corresponding phantom gels differed by a factor of ~2.5. Thus in each case, dissimilar degrees of influence may have been exhibited by the changes in T_1 upon the corresponding change in the signal intensity asymptote. Nevertheless, the comparability of the NMRI predictions and the post-mortem EVLW measurements suggests that although dissimilar degrees of influence by T_1 may have been present in the phantom and the in-vivo experiments, the consequences of this dissimilarity are not excessively disadvantageous. Under

such circumstances, the water density-integrated signal intensity relationship would appear to represent a good methodology for assessing temporal changes in the volume of in-vivo EVLW.

The NMRI results bore an excellent correlation with the post-mortem findings. The pulmonary edema was initially presented in an uniform fashion, both in the distribution and in the nature of the fluid exudate. Such findings are not only corroborated by our post-mortem EVLW measurements (see Table 5.3.5, series B), but also by other physiological and histological data. For example, Hedlund et al.(10,11) perceived with computed tomography that the pattern of oleic acid(0.05 ml/kg)induced-edema was initially uniform throughout both lungs. These authors believed this to be due to the low specific gravity of oleic acid, which would direct the resultant fat emboli to higher bifurcation branches of the pulmonary vasculature. Although preferential redistribution of pulmonary blood flow was not induced by the oleic acid, observed lesions were oftentimes manifested throughout the lung contrary to the pre-existent blood flow distribution. Identical observations in blood flow patterns have been made both by Ali and Wood(1) and by Montaner et al.(18). These investigators, at 2 hours after oleic acid infusion(0.08 ml/kg), found decreases in the regional blood flow, but no change in its distribution with respect to lung height. Moreover, their EVLW measurements, after correction for blood water volume, did not display gravity dependency.

These findings are virtually identical to the series B EVLW determinations, made at the same time relative to oleic acid infusion, and in lung regions where perfusion pressures are most likely to be nearly uniform. It has been suggested(10) that oleic acid-induced damage to the pulmonary capillary endothelium occurs within the first pass of oleic acid through the lung, but that accumulation of EVLW in these damaged areas occurs more slowly. The uniformity of the edematous volumes of the early NMRI dataset, acquired ~2 hours after injection of oleic acid, would support this hypothesis(see Table 5.3.2). Although not presented, the ROI volumes of edematous lung regions for series B displayed the same uniformity as observed in the first series A NMRI dataset.

Both T_1 and T_2 indices also suggest a uniformity in the initial nature of the edema fluid exudate. Histological studies, with both light and electron microscopy(5), have revealed that in this same time frame(2-3 hours after oleic acid infusion) there is no evidence to suggest regional differences in the water proton environment. Thus during this time frame, although edema and capillary congestion are marked, potential proton-binding sites such as fibrin, platelets, and cell debris are not preferentially distributed throughout the various lung regions.

The later series A NMRI dataset, acquired ~4-5 hours after injection of oleic acid, reveals that significant temporal changes occurred in the induced edema. These

changes comprise regional differences both in edema volume and exudate nature. Ventral lung edematous ROI volumes did not appreciably alter throughout the course of series A experiments, indicating a containment of the edema fluid. This is suggestive of alveolar flooding. Several investigators(5,18,26,29) have proposed the alveolus as the major site for EVLW accumulation in oleic acid-induced edema. The rapid and continual deterioration of the arterial blood gas tensions in these animals(see Table 5.3.1) is compatible with this proposition. Such a condition would precipitate alveolar instability and collapse, thus significantly reducing the surface area available for gas exchange. Moreover, if edema was confined to the interstitium, alveolar gas exchange would be less affected, as grossly impaired oxygen diffusion is not a consequence of an increased interstitial thickness(17, 18).

Nevertheless, it is surprising that the ventral lung edematous ROI volumes did not increase during the series A experiments. However, upper lung region T_1 indices were found to decrease with time consistently, indicating a decrease in water proton mobility within the associated edema exudate. Hemorrhaging into the alveolar cuffs is known to be induced by oleic acid(5,13,14,18), with subsequent leakage of fibrinogen, to later form fibrin, into the airspace. Jones et al.(13) demonstrated that fluroescein isothiocyanate-dextran leaked from the blood into adjacent alveoli to a far greater degree in oleic acid lesions than

in other models of pulmonary edema. However, this was eventually checked, indicating some means of hemostasis after the initial oleic acid damage. Dvorak et al.(6) have shown that extravascular coagulation can be initiated by large microvascular leaks. The above reported accounts of fibrin deposition, both on the alveolar surface and within the alveolar airspace, would suggest that this is indeed occurring in oleic acid-induced pathology. Clinical studies have also shown disseminating coagulation as one of the prime aggravating factors in patients with pulmonary edema consequent to fatty acid embolization(15). Histological investigations of temporal changes in oleic acid-induced pathology(5) have revealed that, in addition to the components of the hemostasis mechanism discussed above, alveolar exudate possesses continually increasing amounts of protein. This is consistent with a decrease in the T_1 index with time.

In contrast, dorsal region edematous ROI volumes and T_1 indices both increased with time in series A experiments(see Tables 5.3.2 and 5.3.3). The increase in edematous ROI volume in the dorsal lung region is indicative of either a gravity-dependent distribution of later edema fluid or of interstitial edema which later redistributes itself toward dependent lung regions. The hemostasis mechanisms discussed above must be occurring throughout all regions injured by the infused oleic acid. However, the later NMRI parameters indicate, at least within the more dependent regions, that

accumulation of edema fluid may be mediated through other pathways. One example of such other pathways would be a gravity-dependent course through the interstitial spaces. Unfortunately there have been few studies, into oleic acid-induced pulmonary edema, undertaken over a time scale comparable to the second NMRI dataset. Consequently, there is little evidence either to confirm or deny the later experimental findings. Derks and Jacobovitz-Derks(5) have reported that, although alveolar flooding is the principal site for edema accumulation in this model, interstitial fluid is also observed. Moreover, once such edema has formed, its volume remains virtually constant over the following 12 hours. Zumsteg et al.(29) have described a pressure-dependent pathway existing for interstitial edema formation subsequent to increased pulmonary capillary permeability. If such conditions were present in the series A animals, temporal changes in the volume distribution of interstitial edema would be influenced by gravity. Thus, interstitial edema induced soon after oleic acid injection may have slowly yet continually redistributed towards dependent lung regions throughout series A experiments. Such edema fluid would not be influenced by the hemostasis mechanism discussed above, water protons within its fluid volume would remain mobile and with gradual accumulation of EVLW increase the proton T_1 indices of the dependent lung tissue. Such a process may have begun in the later stages of the first NMRI dataset. However, the data acquisition

procedures would prevent this process from being observed until the later dataset. The two facts that first, interstitial edema is relatively minor in oleic acid-induced pneumopathy and second, that its volume is small relative to that of alveolar edema, may help to explain the later influence of such edema fluid redistribution on the T_1 indices. Complete redistribution of this interstitial edema volume may have been required before significant changes were observed in the T_1 indices. These data emphasize the inadequacy of correlating lung water content with a single NMR parameter, for a constant edema fluid volume may indeed contain within it, significant changes in relaxation indices. As a technical addendum, the significantly increased T_1 indices from dependent lung regions which were recorded in the later NMRI dataset, are most probably still underestimates of the actual T_1 values(see section 4.2.1).

The apparent insensitivity of T_2 to alterations in the exudate nature was not altogether an expected finding. From studies on protein solutions(2), and from the phantom study(see Tables 4.3.1 and 4.3.2), transverse relaxation appears to be more sensitive to changes in water concentration. It is possible that the apparent insensitivity of T_2 which was observed is due to the transverse decay acquiring a bi-exponential nature over the time course of series A experiments, possibly as a result of the development of two water compartments. The decrease in spin-echo amplitude, in all later T_2 measurements, displayed

a close resemblance to bi-exponential decay. However, with only four spin-echoes being employed to derive T_2 indices, the data is insufficient to be unequivocal over two co-existent exponential decay rates. If bi-exponential transverse decay was indeed present, a mono-exponential curve-fitting routine would underestimate the longer T_2 index of the more fluid compartment. The fact that T_1 indices did not exhibit this behaviour does not conflict with this hypothesis. Since T_1 is much longer than T_2, rapid exchange between the two compartments could average the longitudinal relaxation.

Future technical improvements that give rise to a greater number of data points for determining the T_2 index may enable the clear observation of bi-exponentiality in the magnetization decay. Partitioning into the respective fast and slow components may provide information on the constituents of a given edema fluid and their relative temporal changes. One step towards this objective would be the use of cardiac cycle-synchronization, which would in turn enable non-selective 180° refocussing pulses to be employed in an MSE sequence. This would improve S/N and provide a greater number of spin-echo images with which to determine T_2 indices. It is important however, to ensure that the entire echo train can still be regarded as a single time point of the cardiac cycle. Moreover, the validity of relating co-existent edema constituents with bi-exponential magnetization decay remains to be determined, and indeed may

not be as simply related as it has been suggested.

Hemoglobin was chosen as the erythrocyte marker in the determination of lung tissue EVLW for important technical reasons. Although chromium(Cr^{51})-labelled erythrocytes have been employed for decades as markers of a tissue's red cell pool, their employment in NMR related studies leads to difficulties. When sodium chromate(Na_2CrO_4) is added to erythrocytes, it penetrates the cell membrane and the chromium ion is reduced from diamagnetic Cr^{+6} to paramagnetic Cr^{+3}, which binds with high affinity to the Hb molecule(28). In concentrations of 0.1-10 mM, paramagnetic Cr^{+3} can thus be bound to erythrocytes in sufficient quantities to produce significant decreases both in T_1 and T_2 values of a cell's water protons(7). Consequently, indices of relaxation in vascularized tissue will be altered when the blood volume contains as little as 10% Cr^{51}-labelled erythrocytes. Therefore Hb was employed, as measured in a systemic blood sample, and a pulmonary hematocrit correction factor to determine blood water volumes present within the lung tissue samples. Such procedures have been verified(12,19,21) as being sufficiently valid to support the objectives of this study. Although spectrometric analysis both of whole blood and various Hb solutions have revealed that Hb is the chief determinant of blood proton relaxation times(16,20), I assumed that small concentration increases in extravasated Hb would produce little influence on the T_1 and T_2 indices

of edema fluid, as water proton mobility is not greatly affected by such small changes(16).

One may question whether the decrease in the pO_2 values would produce alterations in tissue T_1 and T_2 indices, independent of those influenced by the edema exudate. Changes in the amount of oxygen physically dissolved in blood would cause deviations in either longitudinal or transverse relaxation. However, Tribathi et al.(25) have reported that spectrometrically determined $1/T_1$ and $1/T_2$ change <10% for a 100 mmHg change in arterial blood oxygen tension. Such a change, however, is well within the limits of error for the relaxation index measurements.

This study demonstrates that, not only is NMRI a sensitive method for monitoring temporal changes in EVLW content, but that it can also separate the intra and extravascular lung water volumes. NMRI proved capable of both detecting a <10% change in EVLW and indicating alterations in the nature of such edema fluid volumes. Notwithstanding these attractive attributes, NMRI unfortunately manifested definite practical limitations for the clinical applicability of the quantitative technique. However, the demonstrated sensitivity of NMRI in assessing temporal changes in the volume, nature, and distribution of pulmonary edema clearly warrant further studies in this area.

REFERENCES:

1) Ali, J. and L.D.H. Wood. Factors affecting perfusion distribution in canine oleic acid pulmonary edema. J. Appl. Physiol. 60: 1498-1503, 1986.

2) Allen, P.S., M.E. Castro, E.O. Treiber, J.A. Lunt, and D.P.J. Boisvert. A proton nmr relaxation evaluation of a model of brain oedema. Phys. Med. Biol. 31: 699-711, 1986.

3) Carroll, F.E., J.E. Loyd, K.B. Nolop, and J.C. Collins. MR imaging parameters in the study of lung water: a preliminary study. Invest. Radiol. 20: 381-387, 1985.

4) Cutillo, A.G., A.H. Morris, D.D. Blatter, T.A. Case, D.C. Ailion, C.H. Durney, and S.A. Johnson. Determination of lung water content and distribution by nuclear magnetic resonance. J. Appl. Physiol. 57: 583-588, 1984.

5) Derks, C.M. and D. Jacobovitz-Derks. Embolic pneumopathy induced by oleic acid: a systematic morphologic study. Am. J. Pathol. 87: 143-158, 1977.

6) Dvorak, H.F., D.R. Senger, A.M. Dvorak, V.S. Harvey, and J. McDonagh. Regulation of extravascular coagulation by microvascular permeability. Science 227: 1059-1061, 1975.

7) Eisenberg, A.D., T.E. Conturo, M.R. Mitchell, M.S. Schwartzberg, R.R. Prince, M.F. Rich, C.L. Partain, and A.E. James, Jr.. Enhancement of red blood cell proton relaxation with chromium labelling. Invest. Radiol. 21: 137-143, 1986

8) Fishman, A.P.. Pulmonary edema: the water-exchanging function of the lung. Circ. 46: 390-408, 1972.

9) Hayes, C.E., T.A. Case, and D.C. Ailion. Lung water quantification by nuclear magnetic resonance imaging. Science 216: 1313-1315, 1982.

10) Hedlund, L.W., E.L. Effman, W.M. Bates, J.W. Beck, P.L. Goulding, and C.E. Putman. Pulmonary edema: a ct study of regional changes in lung density following oleic acid injury. J. Comp. Assist. Tomog. 6: 939-946, 1982.

11) Hedlund, L.W., P. Vock, E.L. Effman, and C.E. Putman. Morphology of oleic acid-induced lung injury: observations from computed tomography, specimen radiography, and histology. Invest. Radiol. 20: 2-8, 1985.

12) Hemingway, H.. A method of chemical analysis of guinea pig lung for the factors involved in pulmonary edema. J. Lab. Clin. Med. 35: 817-822, 1950.

13) Jones, J.G., B.D. Minty, J.M. Beeley, D. Royston, J. Crow, and R.F. Grossman. Pulmonary epithelial permeability is immediately increased after embolization with oleic acid but not with neutral fat. Thorax 37: 169-174, 1982.

14) King, E.G., P.K. Nakane, and D.G. Ashbaugh. The canine oleic acid model of fibrin localization in fat embolism. Surgery 69: 782-787, 1971.

15) Liljedahl, S.O. and L. Westermark. Etiology and treatment of fat embolism. Acta Anaesth. Scand. 11: 177-194, 1967.

16) Lindstrom, T.R. and S.H. Koenig. Magnetic field dependent water proton spin lattice relaxation rates of hemoglobin solutions and whole blood. J. Mag. Res. 15: 344-353, 1974.

17) McHardy, G.J.R.. Diffusing capacity and pulmonary gas exchange. Br. J. Dis. Chest 66: 1-20, 1972.

18) Montaner, J.S.G., J. Tsang, K.G. Evans, J.B.M. Mullen, A.R. Burris, D.C. Walker, B. Wiggs, and J.C. Hogg. Alveolar epithelial damage: a critical difference between high pressure and oleic acid-induced low pressure pulmonary edema. J. Clin. Invest. 77: 1786-1796, 1986.

19) Pearce, M.L., J. Yamashita, and J. Beazill. Measurement of pulmonary edema. Circ. Res. 16: 482-488, 1965.

20) Podgorski, G.T., F.E. Carroll, and R.E. Parker. MR evaluation of pulmonary interstitial and intravascular fluids. Invest. Radiol. 21: 478-482, 1986.

21) Rappaport, E., H. Kuida, F.W. Haynes, and L. Dexter. Pulmonary red cell and plasma volumes and pulmonary hematocrit in the normal dog. Am. J. Physiol. 185: 127-132, 1956.

22) Schmidt, H.C., M.T. McNamara, R.C. Brasch, and C.B. Higgins. Assessment of severity of experimental pulmonary edema with magnetic resonance imaging: effect of relaxation enhancement by gd-dtpa. Invest. Radiol. 20: 687-692, 1985.

23) Schmidt, H.C., D.G. Tsay, and C.B. Higgins. Pulmonary edema: an mr study of permeability and hydrostatic types in animals. Radiol. 158: 297-302, 1986.

24) Skalina, S., H.L. Kundel, G. Wolf, and B. Marshall. The effect of pulmonary edema on proton nuclear magnetic resonance relaxation times. Invest. Radiol. 19: 7-9, 1984.

25) Tripathi, A., G.M. Bydder, J.M.B. Hughes, J.M. Pennock, A. Goatcher, J.S. Orr, R.E. Steiner, and R.H. Greenspan. Effect of oxygen tension on nmr spin-lattice relaxation rate of blood in vivo. Invest. Radiol. 19: 174-178, 1984.

26) Vreim, C.E., P.D. Snashall, and N.C. Staub. Protein composition of lung fluids in anaesthetized dogs with cardiogenic edema. Am. J. Physiol. 231: 1466-1469, 1976.

27) Wexler, H.R., R.L. Nicholson, F.S. Prato, L.S. Carrey, S. Vinitski, and L. Reese. Quantitation of lung water by nuclear magnetic resonance inmaging: a preliminary study. Invest. Radiol. 20: 583-590, 1985.

28) Wintrobe, M.M., R.G. Lee, and D.R. Boggs. Clinical Hematology, 8th edition. Philadelphia, Lea and Febiger 1981, pg. 173.

29) Zumsteg, T.A., A.M. Havill, and M.H. Gee. Relationships among lung extravascular fluid components with alveolar flooding. J. Appl. Physiol. 53: 267-271, 1982.

6. CONCLUSIONS:

The application of NMR imaging to both the investigative research and diagnosis of pulmonary edema manifests great potential for increasing the knowledge of this pathophysiological condition, and its reliable diagnosis. Indeed, the results presented in chapter 5(see sections 5.3 and 5.4) demonstrate that NMR imaging may indicate the occurrence of pathological changes that have hitherto been discernable only through histological and invasive physiological examinations.

Unfortunately, the acquisition of such analytical findings is a most difficult endeavour. Continual respiratory motion, a very low S/N from lung tissue, and an appreciable magnitude of highly-pulsatile pulmonary blood flow all contribute to significantly degrade the quality of images obtained from the in-vivo lung. Corrective and/or compensatory methods, intended to lessen or remove the influences of the above constituents, must be incorporated into the data acquisition procedures if meaningful quantitative information is to be realized. Moreover, as discussed in chapter 3, the possession of such information is not a natural consequence to the generation of quality NMR images. Depending upon the data acquisition procedure employed, image quality and the subsequent measurement of accurate NMR parameters may indeed be exclusive.

Although the phenomenon of a decreasing ROI volume-integrated signal intensity with increasing water density was consistently observed throughout both the phantom and in-vivo experiments, the inability to account for this behaviour and to accurately describe it through a mathematical model warrants continued development of the proposed lung water quantification technique. The results of this project indicate that a relationship between water density and ROI volume-integrated signal intensity can indeed be established. The preliminary results obtained from the in-vivo experiments(see Table 5.3.6) are encouraging in this regard. However, a mathematical model should become a principal objective of future investigative endeavours in this area.

The longitudinal relaxation behaviour of edematous lung tissue is such that one may anticipate T_1 values of at least 1.0 second. Thus, the accurate measurement of T_1 indices becomes an extremely time-consuming procedure, especially when performed via images generated with respiratory-gated data acquisition. It is for this reason that the SR imaging pulse sequence(see section 5.2.1) represents the most efficient route for accomplishing this goal. Nevertheless, even with the employment of this pulse sequence, a reliable 5-point estimation of T_1 requires 1.5-2.0 hours. This would therefore restrict the application of the developed quantitative NMR technique to primarily research investigations. Moreover, optimal results would be expected

from animal models of pulmonary edema where the evolution of the associated pathophysiology is either slow or relatively static throughout NMR data acquisition. Notwithstanding these important time considerations, NMR imaging does, however, represent a markedly sensitive non-invasive tool for the quantification and description of pulmonary edema.

Quantitative NMR measurements of blood, protein solutions, and several different tissue fluids have demonstrated T_2 as an effective discriminatory parameter for the compartmentalization of water protons. This is manifested as either a bi-exponential, or multi-exponential, nature of the associated transverse magnetization decay. Although evidence for this phenomenon was presented in the imaging results of chapter 5(see sections 5.3.1 and 5.4), this evidence was not unequivocal. Nevertheless, it may be that T_2 and proton density could provide a reasonable in-vivo description of lung water content. Both of these parameters may be obtained with one MSE imaging pulse sequence, consequently diminishing the time requirements associated with the acquisition of image data essential for the employment of the developed quantification scheme. The prinicpal requisite for quantitatively assessing bi-exponential T_2 decay is a large number of spin-echo images with which to calculate the transverse relaxation. Two methods of attaining this goal would be:

1) to incorporate cardiac-synchronization into the data acquisition procedure, thereby enabling the use of non-selective 180° RF refocussing pulses, and

2) the employment of a decoupled surface-coil receiver, allowing the acquisition, with improved S/N, of relaxation indices from a localized volume of edematous tissue

The second of these is, perhaps, the more attractive since cardiac cycle-synchronization would only lengthen the time required to generate any image. From the experience gained during the investigations described in this thesis, it appears highly unlikely that more than 8 spin-echo images may be acquired from the in-vivo lung, regardless of the particular imaging protocol employed. Whether or not this number of spin echoes would prove sufficient to quantitatively assess bi-exponential T_2 decay in edematous lung tissue has not yet been ascertained.

This project has clearly demonstrated that NMR imaging represents an excellent analytical tool for the study of lung water. In addition to being involved with the simple quantification and description of edema fluid volume, this imaging modality may indeed prove capable of differentiating between different types of lung edema(hydrostatic, increased permeability, alveolar, interstitial, etc.), as well as different constituents(blood, protein, and plasma) of an

edema exudate. The encouraging findings of this project warrant continued research and development in this investigative area. The clinical relevance of increased lung water content demonstrates its necessity.

APPENDIX

Important Characteristics of the electronic respiratory-gating circuit are:

1) The 43 kΩ resistor, associated with the LM339N chip, (see diagram, next page) is responsible for establishing the detection level of the circuit. All other variable resistors control the timing intervals, and are thus associated with the NE556A chips.

2) The operating voltage for the cicuit is from 0 to V_{cc}. The baseline of the input signal is set to 0.5 V_{cc}. Therefore, if V_{cc} = 5V, the pressure signal input(P_{aw}) must be less than 5V peak-to-peak, and a positive peak input must be less than 2.5V, zero-to-peak.

A schematic diagram of the electronic gating circuit is presented on the following page.

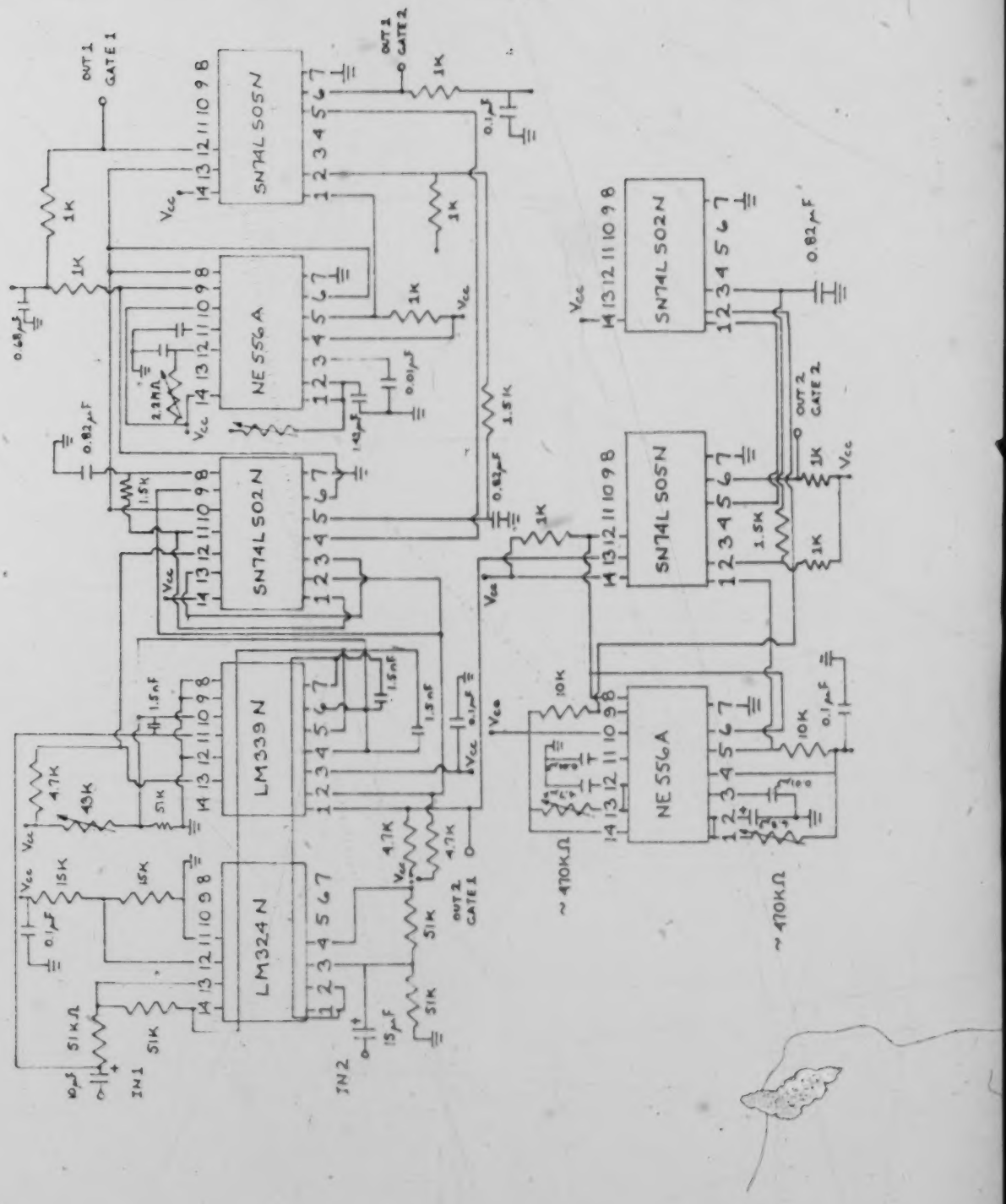
SN74L 502N
SN74L 505N
NE 556A
LM339N
LM324N
OUT 1 GATE 1
OUT 2 GATE 1
OUT 1 GATE 2
OUT 2 GATE 2
IN1
IN2
Vcc
~ 470KΩ
~ 470KΩ